Doctoral Thesis ETH No. 15677

On the Parameterisations of the Turbulent Fluxes in GCMs

A dissertation submitted to the
SWISS FEDERAL INSTITUTE OF TECHNOLOGY ZURICH

for the degree of

Doctor of Natural Sciences

presented by

Raelene Sheppard

Masters Degree in Science (MacQuarie University, Sydney, Australia)

born 02.04.1974

citizen of Australia

accepted on the recommendation of
Prof. Atsumu Ohmura, examiner
Dr. Martin Wild, Dr. Mathias Rotach, Dr. Fred Bosveld, co-examiners

2004

To Dad

Acknowledgments

Firstly, I would like to give my fullest gratitude to Prof. Atsumu Ohmura. Without him, I would never be writing these words or the words that follow. His support during my degree has been unswerving and unconditional. Not only did he find a topic that was suitable to my tastes, but he helped me gather the MRI data, interpret results and pushed me through those difficult times that all PhD students have. I could never wish for a better professor, supervisor or friend.

I would also like to thank Dr. Martin Wild whose knowledge of models is fathomless. I am grateful that he always had time to answer my questions, and am pleased to call such a competent supervisor a friend. Thanks also to Dr. Andreas Roesch who helped with so many things. His help with IDL, BSRN data and the ECHAM4 model are greatly appreciated. Further thanks go to Dr. Mathias Rotach and Dr. Pierluigi Calanca for helping me understand the boundary layer. Thankyou also to Dr. Hendrik Huwald and Dr. Christian Schneeberger for answering my endless questions about IDL and LaTeX, and Prof. Heinz Blatter for assistance with many mathematical questions.

I am further indepted to the modelling groups for their help and support. In particular, Dr. Rachel Stratton from UKMO, Dr. Michel Déqué from Météo-France, Dr. Pedro Viterbo from ECMWF, Dr. Erich Roeckner from MPI and Dr. Andrea Molod from NASA. Thanks also to those scientists that supplied and helped understand the observational data, in particular, Prof. Hisao Ohno and Prof. Toyoaki Tanake (retired) from MRI, Dr. Christof Ammann from the Swiss Federal Research Station for Agroecology and Agriculture, Dr. Fred Bosveld from KNMI, Dr. David Murray (deceased) from the University of Otago and Dr. Hans Gilgen from IACETH.

On a personal level, I would like to thank my office mate Peter Schelander. He made science fun, and provided a lively and entertaining environment. Thanks also to the "badminton crew", Dr. Hermann Hegner and Christine Walser. You helped me release my weekly frustrations, and let me realise that having an office job is a pretty good thing when my muscles are so sore! Thankyou also to the "DOKO crew" for providing great entertainment and interesting chats that gave me a chance to "switch off" from work.

To my family, I am so grateful to my parents. From an early age, my mother always told me "I can" when I felt that "I can't". Well, Mum, you were right. I can. Thankyou for never giving up on your stubborn daughter. Thanks also to my extended family, Joanne, Karen, Richard, Amitee and Katrina. Over the years, you have provided more help than you can imagine. Lastly, to my dear husband Otte. You stood by my side, helped me laugh when I needed it and encouraged me to explore my full potential. You're the best.

Abstract

The present work aims at examining the parameterisations of the turbulent fluxes in GCMs with the prospect of proposing improvements in these models. Intercomparisons over global, zonal and regional areas show large differences between the models, indicating the difficulty in parameterising the turbulent fluxes. On a local scale, observations at sites from the GEBA database, Cabauw, The Netherlands, and two newly analysed sites, at Swampy Summit near Dunedin in New Zealand and in Tsukuba near Tokyo in Japan, are compared to modelled fluxes.

The models used in this study included the GCM simulations of ECHAM4, HadAM2b and ARPEGE, as well as the Reanalyses of ERA15, NCEP and GEOS. Based on climatologies, ECHAM4 and ERA15 showed the most accurate turbulent fluxes when compared to observations, with ERA15 showing a slight improvement over ECHAM4. Since both ECHAM4 and ERA15 are based on a similar model, this indicates that the Reanalyses are superior in the determination of the turbulent fluxes. The reason for accurate turbulent fluxes in ECHAM4 and ERA15 is due to an accurate parameterisation of the solar radiation. Results for the other models typically show an overestimation of latent and sensible heat fluxes, which is largely caused by an overestimation of the solar radiation although, depending on the model, underestimated soil moisture availability and overly intense warm air advection also contribute. For example, in HadAM2b, an overestimated solar radiation combined with an underestimated soil moisture leads to an overestimation of latent heat flux in early summer, and a severe underestimation in late summer. ARPEGE, however, exhibits a too intense zonal flow throughout the year, which produces an excessive moist advection, leading to increased precipitation and evaporation. Lastly, GEOS suffers from an overestimated soil moisture and a surface that is too warm leading to an overestimation in the latent heat flux.

Different data were available for the two newly analysed sites used for this comparison study. The Swampy Summit site consisted of 8 precipitation gauges and a weighing lysimeter enabling the accurate determination of the latent heat flux. The site at MRI has a 200 m tower, one of the few such towers existing.

Measurements from the 200 m tower at MRI included 1 minute mean values of temperature (Pt-100), windspeed (propeller anemometer) and humidity (capacitance hygrometer), as well as 3 dimensional 0.1 second sonic anemo-thermometer data of temperature and windspeed. The wealth of measurements available made it possible to compare methods to determine the turbulent fluxes. Results show that standard methods to determine the turbulent fluxes are not necessarily accurate when considering inhomogeneity. New equations for ϕ_h are proposed from the MRI data to account for the heterogeneity of the site.

The measurements from MRI were then used in conjunction with the parameterisations of ECHAM4. While monthly mean turbulent fluxes from ECHAM4 show good agreement compared to observations, at a half hour timescale, major differences occur. For instance, the momentum flux in ECHAM4 is underestimated for small values and overestimated for large values, while the sensible heat flux in ECHAM4 is continually larger than sonic observations, which are considered to most closely

represent reality. This appears to be due to the use of surface data, such as roughness length of momentum, surface temperature and surface humidity, for the bulk parameterisations. A number of possible solutions exist including the addition of a layer that is close to the surface to determine the atmospheric temperature and windspeed close to the surface rather than the surface data, or the addition of a layer at, say, 2 m or 10 m. The former possibility has the advantage that small gradients of temperature or windspeed are less likely.

Zusammenfassung

Das Ziel dieser Arbeit besteht in der Analyse von Parametrisierungen von turbulenten Flüssen in GCMs und den entsprechenden Vorschlgen zu deren Verbesserung für diese Modelle. Zwischenvergleiche unter den globalen, zonalen und regionalen Gebieten zeigen grosse Unterschiede zwischen den einzelnen Modellen auf und lassen auf Schwierigkeiten bei der Parametrisierung von turbulenten Flüssen schliessen. Auf lokaler Ebene werden Beobachtungen von Standorten aus der GEBA-Datenbank, Cabauw, Holland und zwei neulich untersuchte Standorte in Swampy Summit bei Dunedin, Neuseeland, und Tsukuba bei Tokyo, Japan mit Modell-Flüssen verglichen.

Die in dieser Studie verwendeten Modelle schliessen die GCM-Simulationen von ECHAMA4, HadAM2b und ARPEGE, sowie auch die Reanalysen von ERA15, NCEP und GEOS mit ein. Auf der Basis von Klimatologien weisen ECHAM4 und ERA15 gegenüber der beobachteten Wirklichkeit die genauesten turbulenten Flüsse auf, wobei ERA15 gegenüber ECHAM4 ein wenig besser ausfällt. Die Tatsache, dass ECHAM4 und ERA15 auf einem ähnlichen Modell basieren, deutet darauf hin, dass Reanalysen genauer zur Bestimmung von turbulenten Flüssen sind. Der Grund für genaue turbulente Flüsse in ECHAM4 und ERA15 liegt in einer präzisen Parametrisierung der Sonneneinstrahlung. Resultate anderer Modelle weisen bezeichnenderweise eine Überbewertung latenter und sensibler Wärmeflüsse auf, was weitgehend durch eine Überbewertung der Sonneneinstrahlung hervorgerufen wird, obwohl, je nach Modell, auch eine zu geringe Bewertung der verfügbaren Bodenfeuchtigkeit und eine übermässig starke Warmluftadvektion dazu beitragen. In HadAM2b führt beispielsweise eine Überbewertung der Solarstrahlung, kombiniert mit einer unterbewerteten Bodenfeuchtigkeit, zur Überbewertung des frühsommerlichen latenten Wärmeflusses und einer starken Unterbewertung im Spätsommer. Demgegenüber zeigt ARPEGE während des ganzen Jahres eine zu starke zonale Strömung auf, was eine exzessive Feuchtigkeitsadvektion hervorruft und dabei zu einer erhöhten Schauertätigkeit und Verdunstung führt. Schliesslich zeigt GEOS eine Überbewertung der Bodenfeuchtigkeit und eine zu warme Oberfläche, was wiederum eine Überbewertung des latenten Wärmeflusses bewirkt.

Für diese Vergleichsstudie standen diverse Daten der zwei in dieser Studie analysierten Standorte zur Verfügung. Der Swampy Summit Standort bestand aus 8 Niederschlagsmessgeräten und einem wiegenden Lysimeter, wodurch der latente Wärmefluss genau bestimmt werden konnte. Das Standort von MRI zeichnet sich durch einen der wenigen heute bestehenden 200 Meter hohen Türme aus.

Messungen auf dem 200 Meter-MRI-Turm schliessen 1-Minuten-Mittel Temperatur (Pt-100), Windgeschwindigkeit (Propeller-Anemometer) und Feuchtigkeit (Kapazitanz-Hygrometer) mit ein, sowie von einem Anemothermometer in 0.1 Sekunden-Intervallen gemessene 3-dimensionale Temperatur- und Windgeschwindigkeitsdaten. Die ganze Menge von verfügbaren Messungen erlaubte es, die verschiedenen Methoden zur Bestimmung von turbulenten Flüssen zu vergleichen. Dabei beweisen die Resultate, dass Standardmethoden zur Bestimmung von turbulenten Flüssen nicht unbedingt präzise ausfallen, wenn man die fehlende Homogenität berücksichtigt. MRI-Daten schlagen für ϕ_h neue Gleichungen vor, um

der Heterogenität des Standortes Rechnung zu tragen.

Die MRI-Messungen wurden dann in Kombination mit den ECHAM4-Parametrisierungen verwendet. Während die monatlichen turbulenten Flüsse von ECHAM4 gut mit den Beobachtungen übereinstimmen, treten bei halbstündlichen Mitteln grössere Unterschiede auf. Der Impulsfluss in ECHAM4 wird beispielsweise für kleine Werte unter- und bei grösseren Werten überbewertet, während der sensible Wärmefluss in ECHAM4 stets höher ist als bei Sonic-Messungen, welche der Realität angeblich am nächsten kommen. Es scheint, dass dies auf den Einbezug von Oberflächenwerten, wie beispielsweise Rauhigkeitslänge von Implus, Oberflächentemperatur und -feuchtigkeit in die groben Parametrisierungen zurückzuführen ist. Heute verfügt man über mehrere Lösungsansätze. Dazu gehört die Verwendung einer zusätzlichen Schicht zur Bestimmung der atmosphärischen Temperatur und Windgeschwindigkeit nahe der Oberfläche anstelle der Oberflächenmessungen oder das Hinzufügen einer Schicht in 2 oder 10 Metern Höhe. Erstere Lösungsmöglichkeit bietet den Vorteil, dass kleinere Gradienten in Temperatur oder Windgeschwindigkeit weniger wahrscheinlich sind.

Contents

List of Tables

List of Figures

Chapter 1

Introduction

1.1 Introduction

The constant flux layer (which is typically about the lowest 10% of the planetary boundary layer) is defined as the part of the boundary layer where the fluxes vary by less than 10% of their magnitude from the surface flux (Stull, 1988). Studies of the constant flux layer are important to analyse the interactions between the atmosphere, earth's surface and biosphere. This layer is characterized by intense, small scale turbulence which is generated by surface roughness and convection. Thus, it is possible to learn more about this layer by analysing the turbulent fluxes.

The turbulent fluxes are important determinants of the hydrological cycle and energy balance. They largely influence boundary layer exchanges, and the intensity of moist convective processes. The partitioning of the turbulent fluxes into the sensible and latent components is determined by the temperature difference between the atmosphere and the earth's surface, and the wetness of the surface, which can influence, for example, low-frequency atmospheric variability (Viterbo and Beljaars, 1995).

The momentum flux is important since it describes the state of the turbulence in the atmosphere. The analysis of the momentum flux makes it possible to define the transport of heat and water vapour, as well as pollutants.

Therefore, the accurate parameterisation of these fluxes in general circulation models (GCMs) and Reanalyses is essential for the reliable simulation of the climate system. However, to date, only limited studies have been completed to validate the parameterisations of the fluxes in these models. Firstly, the Project for Intercomparison of Land-Surface Parameterization Schemes (PILPS) was completed to evaluate the parameterisation of interactions between the atmosphere, earth's surface and biosphere in climate and weather forecast models (see for example Chen et al., 1997). This study used measurement data of sensible and latent heat flux from Cabauw, The Netherlands. Although all 23 schemes analysed used identical atmospheric forcings and land-surface parameters, significant differences between observations and numerically derived results were found. Secondly, Forrer (1999) briefly discusses the difficulties in using GCMs to simulate the sensible heat flux in the constant flux layer over the Greenland ice sheet. This study suggested that more accurate values

1

of the sensible heat flux can be obtained from GCMs by adding in the buoyancy length scale (the largest scale where sufficient momentum exists to produce an eddy-like motion in the vertical plane against the restoring buoyancy force). Also on the Greenland ice sheet, Ohmura et al. (1996) found that, while the GCM modelled net surface heat flux was comparable to observations, the modelled sensible and latent heat fluxes were largely different, with the modelled sensible heat flux too low and the modelled latent heat flux too high when compared to observations. Ohmura et al. (1996) do not discuss the possible reasons for these differences, but the fact that the model results show vastly different values to observations suggests that further study in this topic is required. This study will make steps towards this goal.

In order to validate the simulated fluxes on the surface, and in the constant flux layer, it is necessary to have observational measurements of sensible and latent heat fluxes, as well as the momentum flux. This work uses surface observations obtained from the Global Energy Balance Archive (GEBA), as well as sites in Swampy Summit, New Zealand, Tsukuba, Japan and Cabauw, The Netherlands, for the validation of the turbulent fluxes. For the validation of the parameterisations in the constant flux layer, a newly analysed site at Tsukuba, Japan is used.

1.2 Aims

Thus the main aims of this work are as follows:

- To identify the systematic errors in GCMs.

- To test and propose improvements to the parameterisations of the turbulent fluxes in GCMs by comparing the simulated fluxes with observations.

- To determine the sensible heat flux and momentum flux from the Meteorological Research Institute (MRI) in Tsukuba, Japan and the latent heat flux from Swampy Summit near Dunedin, New Zealand for the development of an energy balance climatology.

1.3 Structure of Rest of Report

The chapters of this work will be discussed as follows. Chapter 2 will present the methods used in this study. Both the measurement data and the models used will be discussed. Following this, the results will be discussed in Chapter 3. The conclusions will be discussed in Chapter 4.

Chapter 2

Methods, Experiments and Models

2.1 Introduction

This chapter will be broken up into two sections: A discussion of the measurements used for the validation of the GCMs, and; a description of the models themselves. Emphasis will be placed on the site at MRI, Tsukuba, Japan since there is a wealth of data from this newly analysed site, and on the ECHAM4 GCM.

2.2 Measurements

2.2.1 Introduction

To determine the accuracy of GCMs in parameterising the turbulent fluxes, it is essential to compare models to a variety of observational measurements. In this study, observations were obtained from the author's institute, as well as sites at Cabauw in The Netherlands, Swampy Summit near Dunedin in New Zealand and MRI, Tsukuba in Japan. In the following sections of this chapter, the measurement sites will be discussed. The GEBA (discussed below) and Cabauw, The Netherlands sites will only be discussed briefly since they have been described elsewhere in more detail. A more rigorous analysis will be completed for the Swampy Summit, New Zealand and MRI, Tsukuba, Japan sites since they have been newly analysed for this study.

2.2.2 GEBA Sites

The majority of the sensible and latent heat flux measurements used in this study were extracted from the Global Energy Balance Archive (GEBA; previously a part of the World Climate Program - Water: Project A7) database developed at the Institute for Atmospheric and Climate Sciences, ETH Zürich (Ohmura et al., 1989). The GEBA contains monthly mean energy fluxes measured at the surface for

use in re-evaluating the energy balance and for validating the parameterisations in general circulation models (GCMs), as well as other applications. In this study, only long-term entries for the latent heat flux (at least 3 years of measurements) and sensible heat flux (at least 12 months of measurements) were used. In some cases, the sites for the sensible heat flux and latent heat flux are different since there are only limited long-term entries of the fluxes in GEBA. Each site will be discussed separately below.

Hartheim, Germany

The site at Hartheim, Germany (47° 56' N, 7° 37' E, 201 m a.s.l.) is situated over a pine forest in the lower part of the upper Rhine valley. The area is considered to be a homogeneous flood plain (Jaeger, 1978). The pine forest covers a 10 km by 1.5 km area with the measurement site close to the centre of this area. Measurements of both the sensible and latent heat fluxes are obtained for the years 1974-91.

Monthly averages of the latent heat flux at Hartheim are calculated using the water balance equation (Equation 2.1).

$$L_v E = L_v(P - S + SM), \qquad (2.1)$$

where E is the evaporation (mm), P is the precipitation (mm), S is the percolation (mm), SM is the change in soil moisture (mm) and L_v is the latent heat of vapourisation (J kg^{-1}). At this site, the percolation is negligible (i.e. S$\approx$0), and the latent heat flux ($L_v E$) is dominated by the precipitation.

From the determination of the latent heat flux, the sensible heat flux is estimated as the residual of the energy balance equation (Equation 2.2) with positive fluxes directed upwards.

$$H_s = R_n - G - L_v E, \qquad (2.2)$$

where H_s is the sensible heat flux (W m^{-2}), R_n is the net radiation (measured, W m^{-2}) and G is the sub-surface heat flux (W m^{-2}) given by Jaeger (1978).

ERC, Tsukuba, Japan

The measurement site at the Environmental Research Centre (ERC) at Tsukuba, Japan (36° 07' N, 140° 06' E, 30 m a.s.l.) is located on the edge of the Tsukuba city, 90 km north east of Tokyo. The grass-covered field used for this site is surrounded by small trees and buildings. Both the latent and sensible heat flux have been measured at this site from 1981 to present (http://www.suiri.tsukuba.ac.jp/hojyo/databaseE.html).

The latent heat flux at the ERC site is determined using a weighing lysimeter. The sensible heat flux is determined using the eddy correlation method with measurements obtained from sonic anemo-thermometers at three levels (1.6 m, 12.3 m and 29.5 m).

Basel-Binningen, Switzerland

The region around Basel-Binningen, Switzerland (47° 35' N, 7° 35' E, 317 m a.s.l.) is inhomogeneous, with the measurement site surrounded by undulating farmland, trees and buildings. It is located 2 km from the city centre of Basel in the north of Switzerland, at the German border. Measurements of the latent heat flux at this site are obtained for the years 1977-86. At Basel-Binningen, the latent heat flux is determined using a weighing lysimeter.

Rietholzbach, Switzerland

Rietholzbach, Switzerland (47° 23' N, 9° 00' E, 760 m a.s.l.) is located 32 km east of Zürich and is representative of the Swiss pre-alpine areas (Germann et al., 1978). The region is dominated by farmland, surrounded by small mountains (680 m to 950 m a.s.l.), with a row of trees following a river close to the measurement site. Measurements of the latent heat flux are obtained for the years 1977-84. As with Basel-Binningen, the latent heat flux is determined from a weighing lysimeter. The lysimeter has a ground surface of 3.14 m^2 and is 2.5 m deep. It lies on three weighing elements, and measurements are accrued at an hourly timescale.

Tumengalha, Tibet

Tumengalha, Tibet (32° 51' N, 90° 18' E, 3841 m a.s.l.) is situated on the Qinghai-Xizang Plateau, and is governed by strong winds, low temperatures and intense direct solar radiation (Zeng and Xie, 1980). At this site, the sensible heat flux is measured for the year 1965.

Copenhagen, Denmark

The site at Copenhagen, Denmark (55° 40' N, 12° 18' E, 28 m a.s.l.) is located 20 km from the city centre in an open homogeneous experimental field (Aslyng, 1961). The site is considered to lie relatively high when compared to the immediate surroundings (which are typically 5 m a.s.l.) and is covered with a short, dense mixture of clover and grass. The surrounding fields contain grain, clover, grass and root crops. Measurements of the sensible heat flux are obtained from this site for the years 1956-58. The sensible heat flux is determined as the residual of the energy balance (Equation 2.2).

Barrow, Alaska

Barrow, Alaska (71° 11' N, 23° 20' W, 10 m a.s.l.) is located at the northern most point of Alaska and is characterised by open tundra with numerous puddles and ponds in summer and snow-covered plains in winter. Measurements of the sensible heat flux are obtained for the years 1957-1971. At this site, the sensible heat flux is determined using the profile method from levels at 0.5 m, 1 m, 2 m, 4 m, 8 m and 16 m (Weller and Holmgren, 1974).

2.2.3 Cabauw, The Netherlands

Cabauw, The Netherlands (51° 58' N, 4° 56' E, -0.5 m a.s.l.) is located south east of Amsterdam and is characterised by flat meadows and ditches with some villages, orchards and trees. The site terrain is made up of open pasture for at least 400 m in all directions (van Ulden and Wieringa, 1996). Measurements of both latent and sensible heat flux are obtained from this site for the years 1987-96.

For the sensible heat flux, a modified profile method is used which takes into account the effects of the heterogeneous terrain (Beljaars and Bosveld, 1997). This method uses a different aerodynamic roughness length for each wind direction class (18 classes in total) specified from a site-specific table and is based on an analysis of the standard deviation of horizontal wind.

After the determination of the sensible heat flux from the above mentioned modified profile method, the latent heat flux is calculated using the energy balance equation (Equation 2.2).

2.2.4 Swampy Summit, New Zealand

Swampy Summit, New Zealand (45° 47' S, 170° 29' E, 710 m a.s.l.) is a newly analysed site located 10 km north-northwest of Dunedin in the south east of the South Island of New Zealand (Figure 2.1). The site is on a broad north-south oriented plateau which is predominately covered with tussock grass of roughly homogeneous height (Fahey et al., 1996). The leaf area index (LAI) of the region is approximately 3 and albedo is roughly 0.22. The land surrounding the site is flat, with only minor irregularities in topography for more than 100 m in the 2 main wind directions: North east and south west. The regional climate is quite severe, with prevailing westerly winds, intense rain, and the possibility of snow in any month. Temperatures typically range from -5°C to +25°C and are influenced by foehn from the north west, or sea breezes from the east and north east. Measurements of the latent heat flux are available for the years of 1991-96.

At Swampy Summit, a weighing lysimeter is used to measure the latent heat flux. The lysimeter comprises a 5.8 m^2 by 0.7 m deep undisturbed monolith. The weight changes are detected as pulses from a reversible screw which drives a travelling weight along the lever arm to maintain the balance (Fahey et al., 1996). Excess water drains from the monolith base and is measured by a tipping bucket. Measurements of precipitation are from up to 8 tipping bucket gauges (Figure 2.2). The precipitation is sampled at 30 second intervals and logged every 30 minutes.
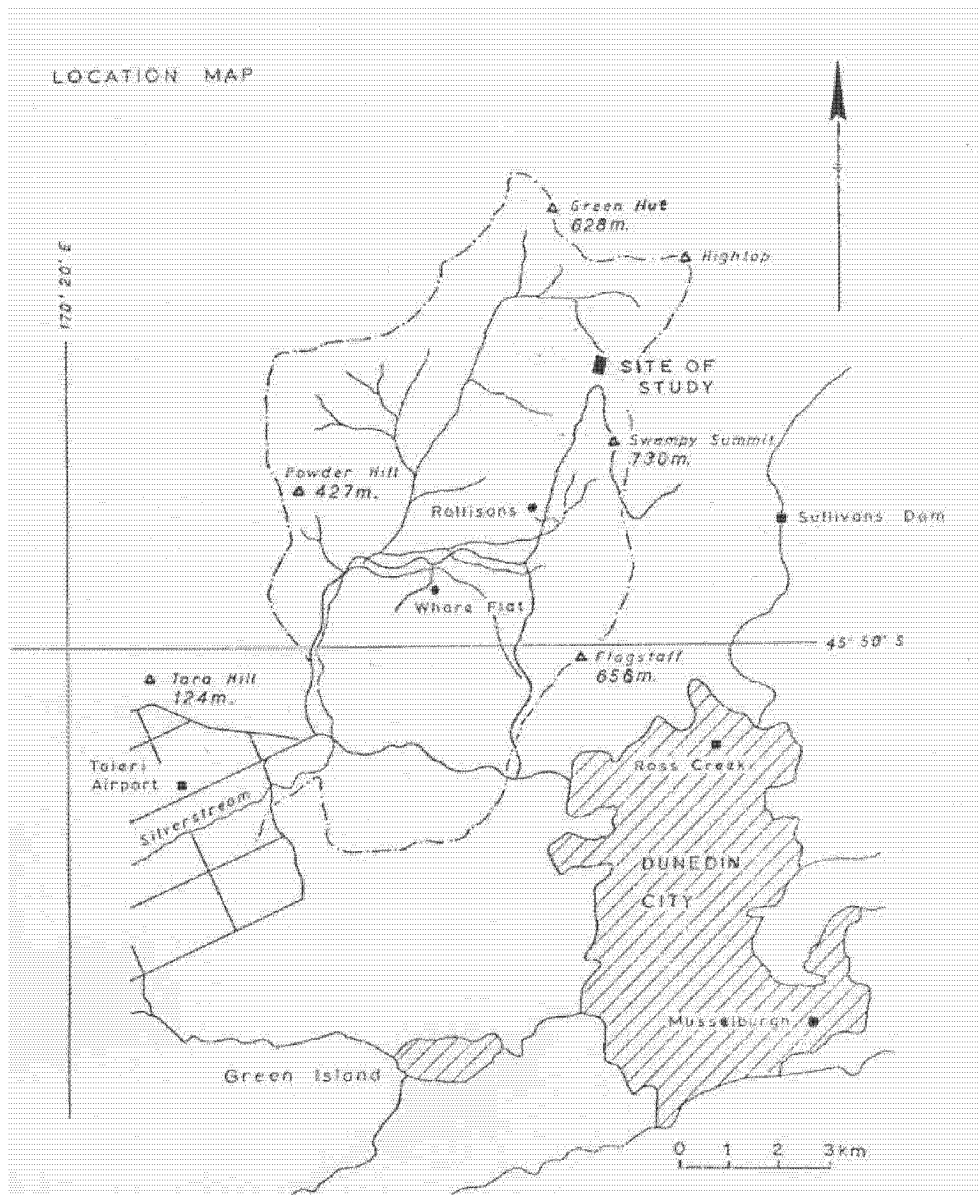
Figure 2.1: The location of the Swampy Summit site in New Zealand.
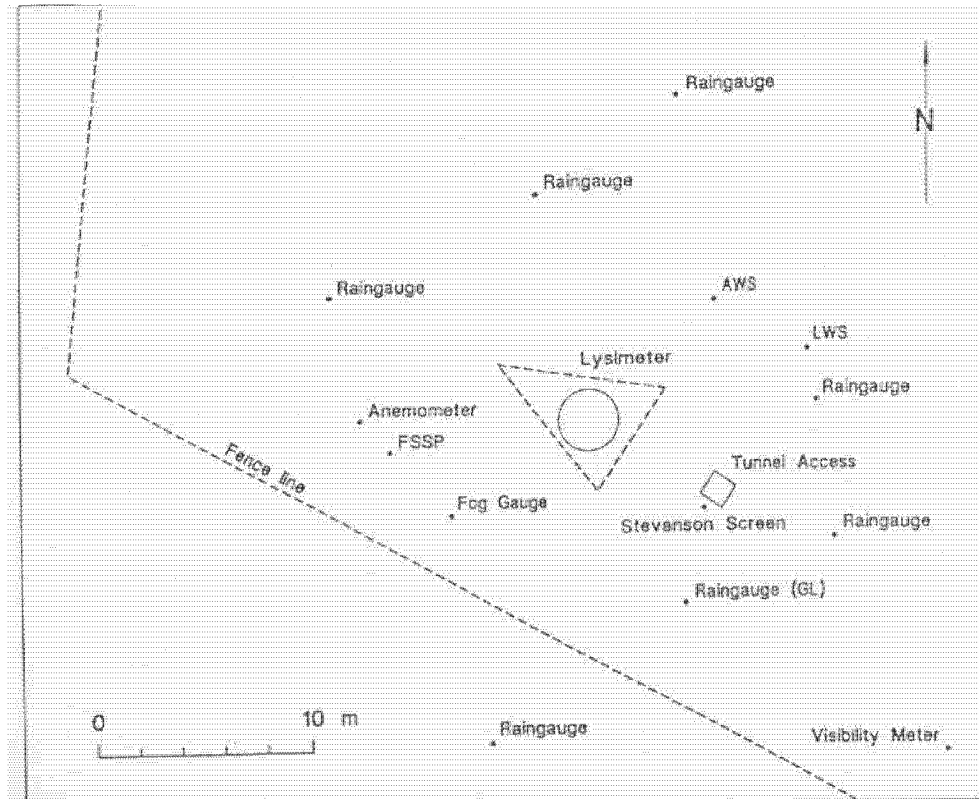
Figure 2.2: The location of the instruments at the Swampy Summit site in New Zealand.

To briefly describe the site at Swampy Summit, it is beneficial to summarise the climatologies of the site. From the data available, the climatologies of windspeed, precipitation and evaporation will be shown.

Figure 2.3 shows the mean (1991-96) daily cycle of windspeed for January and July at Swampy Summit, New Zealand. The site shows typical windspeeds of roughly 6 m s^{-1} throughout the year. The significant difference between the seasons is that summer (January in Figure 2.3) shows a diurnal cycle in windspeed whereas the windspeed in winter (July in Figure 2.3) is relatively constant throughout the day. The diurnal change in windspeed is often caused by the diurnal change in surface heating which is larger in summer.

Figure 2.4 shows the mean monthly (1991-96) precipitation and evaporation in mm day^{-1} for the Swampy Summit site in New Zealand. For precipitation, measurements are also averaged over the 8 available precipitation gauges. As can be seen from the figure, precipitation and evaporation are largest in the summer months (December-February) with precipitation reaching an average of 4.4 mm day^{-1} in December and evaporation reaching a peak value of 3.2 mm day^{-1} in January. The standard deviation in the plots is relatively small showing that the years selected for this study are quite representative, and that the 8 precipitation gauges correlate well.

8
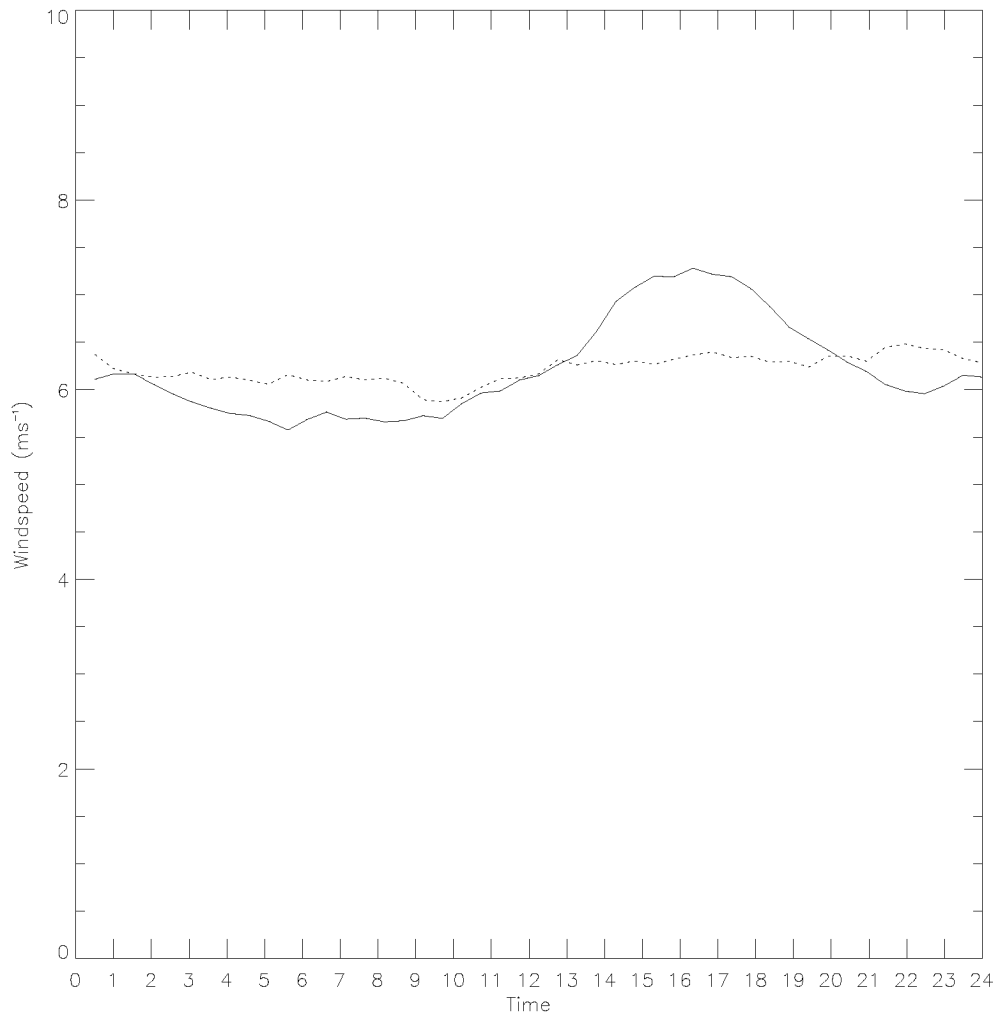
Figure 2.3: Mean daily cycle of windspeed over the years 1991-96 for January (solid line) and July (dotted line) at Swampy Summit, New Zealand. Units in m s^{-1}.
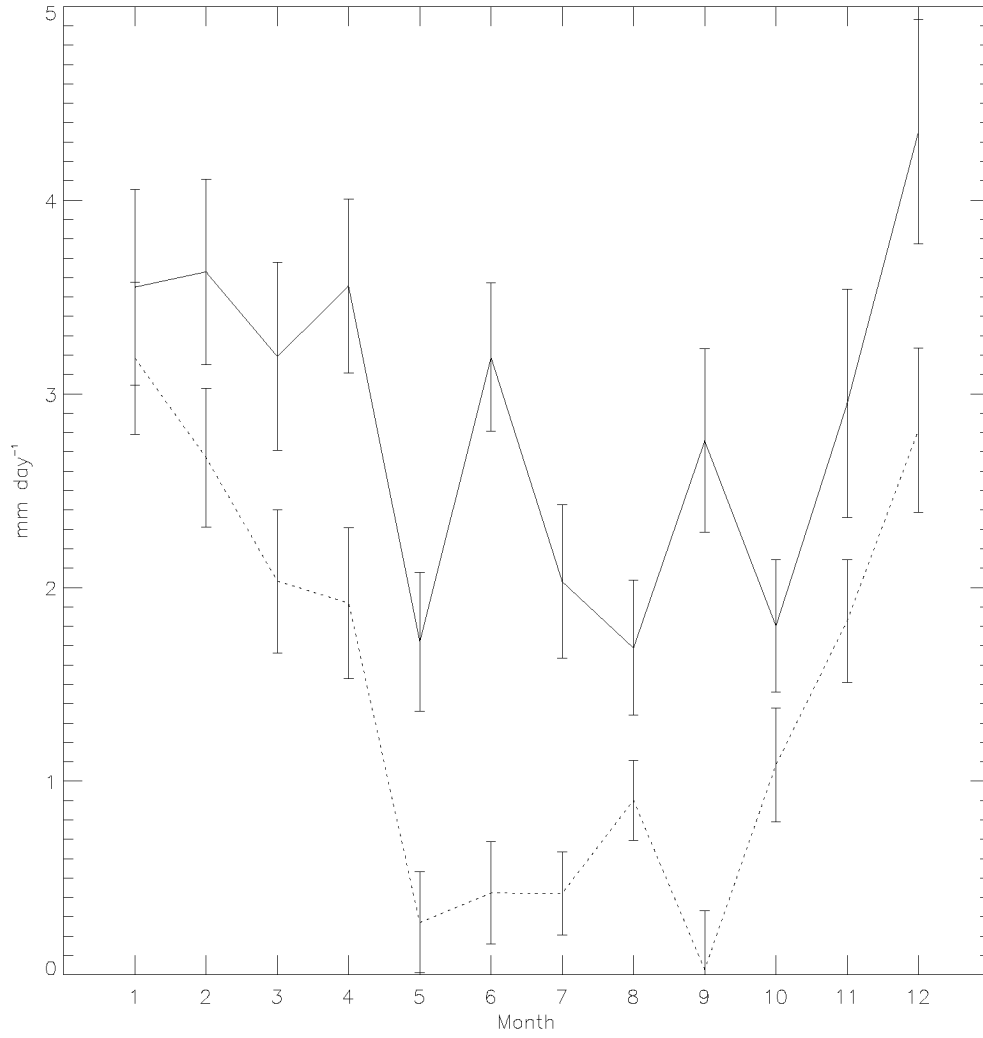
Figure 2.4: Mean precipitation and evaporation for Swampy Summit, New Zealand based on the years 1991-96. The solid line shows the precipitation averaged over the 8 precipitation gauges, the dotted line shows the evaporation. Both curves also show the mean standard deviation (the standard deviation for each year averaged with the standard deviation of each gauge) in measurements. Units in mm day^{-1}.

2.2.5 MRI, Tsukuba, Japan

The measurements used in this study from the Meteorological Research Institute (MRI) at Tsukuba, Japan are taken from a 213 m tower located in the middle-eastern part of Japan (36° 10' N, 140° 10' E, 27 m a.s.l.), 90 km north east of Tokyo. The observational site is a part of the Kanto Plain, 20 km south of Mt. Tsukuba (876 m a.s.l.) and 10 km west of Lake Kasumigaura. As with the site at Swampy Summit, New Zealand, this is a newly analysed site that will be discussed here in more detail than the GEBA sites.

The terrain surrounding the tower is covered with short lawn for 150 m in all directions. Beyond this is a row of pine trees reaching no more than 10 m in height, followed by low-rise buildings in all directions. The closest building is the MRI main building which is 40 m high and lies 300 m north east of the tower. Depending on wind directions, it is possible that this building will have an impact on measurements. Table 2.1 shows the land use map for the area surrounding the tower.

Table 2.1: Map of the land use in the vicinity of the Tsukuba tower (roughly 100 m x 100 m). The cell with the parentheses represents the location of the tower. A description of each number can be found in Table 2.2.

5	6	6	6	5	1	1	1	1	2
6	2	1	5	5	1	1	1	1	3
3	2	1	5	5	5	1	1	1	1
5	5	2	2	2	2	1	1	1	1
2	2	2	2	2	2	2	1	1	2
2	2	2	6	2	2	2	5	2	2
3	2	2	(6)	6	3	3	2	2	3
3	2	3	6	6	3	2	4	3	3
3	2	2	6	5	3	5	4	5	3
2	3	3	2	2	6	6	2	2	3

Table 2.2: Description of land use found in Table 2.1.

1	rice field
2	other agricultural fields
3	forest
4	unused land
5	buildings
6	other man made land use

The MRI, Tsukuba Tower

The tower is a guyed open lattice design, 213 m high (Figure 2.5). The structure is made from galvanised steel with 3 legs spaced 4 m apart. The tower was built in 1973-74 to obtain basic information on diffusion in the boundary layer for air pollution meteorology, and to provide ground-truth of near surface temperature and moisture gradients for satellite observations.

The tower has landings at 6 levels (10 m, 25 m, 50 m, 100 m, 150 m, 200 m). Each of these levels has 3 booms at an angle of 120° to each other which supports the instrumentation (Figure 2.6). The length of each boom reaches 6 m from the edge of the tower. This length was determined from experimental results in a wind tunnel to minimise wind disturbance on measurements (Hanafusa et al., 1979). A rail system is used on each boom, whereby manual winding slides in the instrument stand for maintenance and repairs.

Each boom contains a 3D sonic anemo-thermometer, a propeller anemometer, a Pt-100 resistance thermometer, and a capacitance hygrometer. One minute averages of windspeed, temperature and humidity are available from 1992 to present, while 0.1 second sonic data is available from 1997 to present.
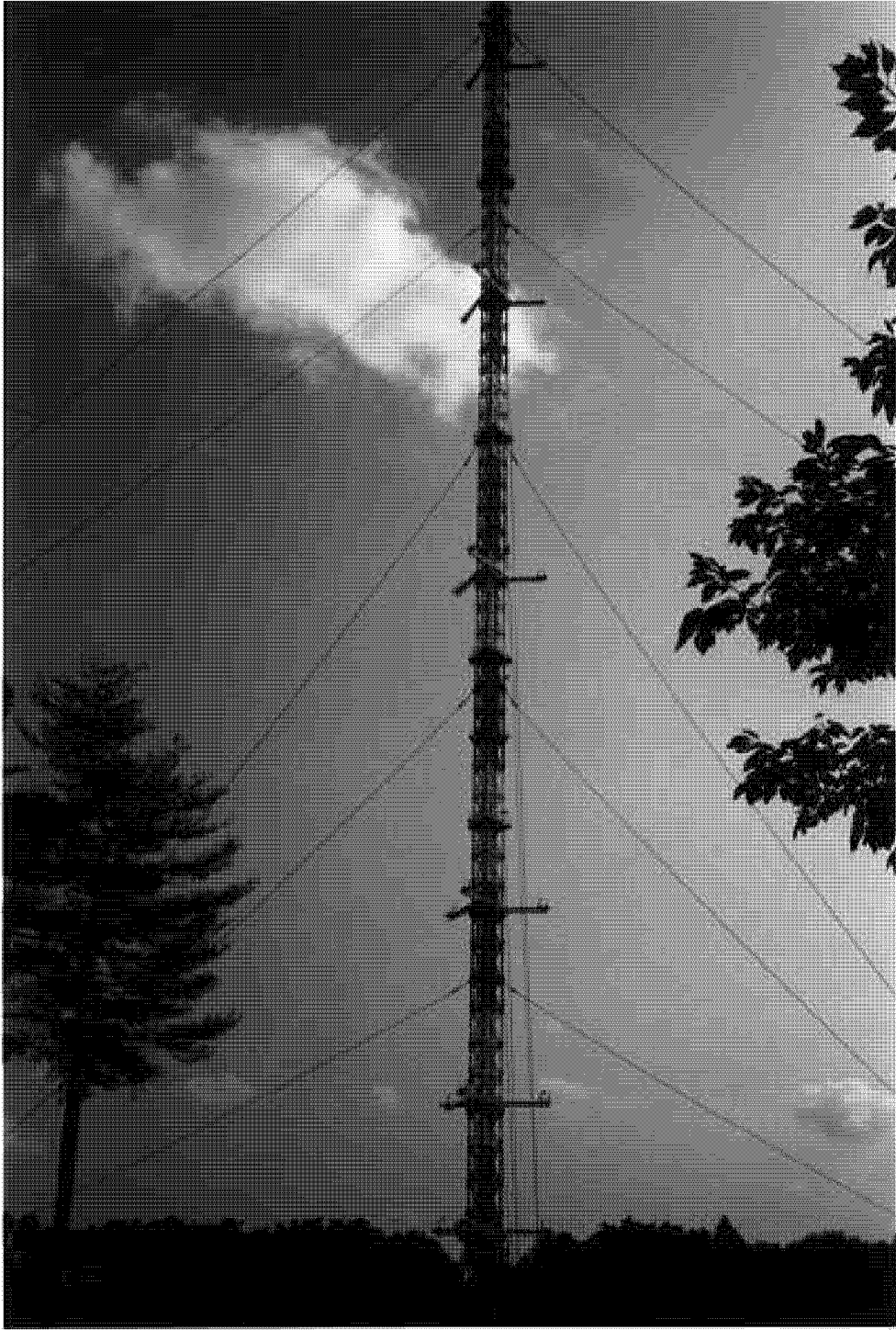
Figure 2.5: The 213 m tower at MRI, Tsukuba, Japan.

Figure 2.6: The instruments on the 213 m tower at MRI, Tsukuba, Japan.

Windspeed, Temperature and Humidity

Before discussing the turbulent fluxes, it is important to analyse the measurements obtained directly from MRI. As mentioned in the previous chapter, windspeed was obtained by both propeller anemometer and sonic anemo-thermometer, temperature was measured by both Pt-100 and sonic and humidity was measured by the capacitance hygrometer.

Table 2.3 shows a summary of the climatologies at the 25 m level at MRI (the reason for the choice of the 25 m level will be discussed later). This analysis showed that May 1997 provided the most reliable dataset in terms of quality and number of measurements. Hence, for the remainder of this study, emphasis will be placed on May 1997.

Table 2.3: Monthly mean windspeed, temperature and humidity for 1997 at the 25 m level.

	Jan	Feb	Mar	Apr	May	Jun	Jul	Aug	Sep	Oct	Nov	Dec
u (m s^{-1})	1.3	1.3	1.5	2.4	2.7	2.2	2.5	2.5	1.8	1.9	1.7	2.0
T (°C)	3.7	4.7	8.5	13.4	17.1	20.2	23.8	24.7	21.1	16.4	12.6	6.9
q (g kg^{-1})	4.0	4.2	3.1	7.3	7.8	3.6	3.7	3.6	3.2	1.8	1.9	3.1

Figure 2.7 shows the propeller anemometer windspeed (u_{prof}) compared to the sonic anemo-thermometer windspeed (u_{sonic}) at each level for May 1997. Typically, both instruments show a good agreement for low windspeeds. At high windspeeds, the propeller anemometer tends to overspeed, since the instrument has difficulty slowing down after short gusts. The large scatter for low windspeeds at the 150 m

level is caused by an instrument problem with the sonics and should be viewed with caution.
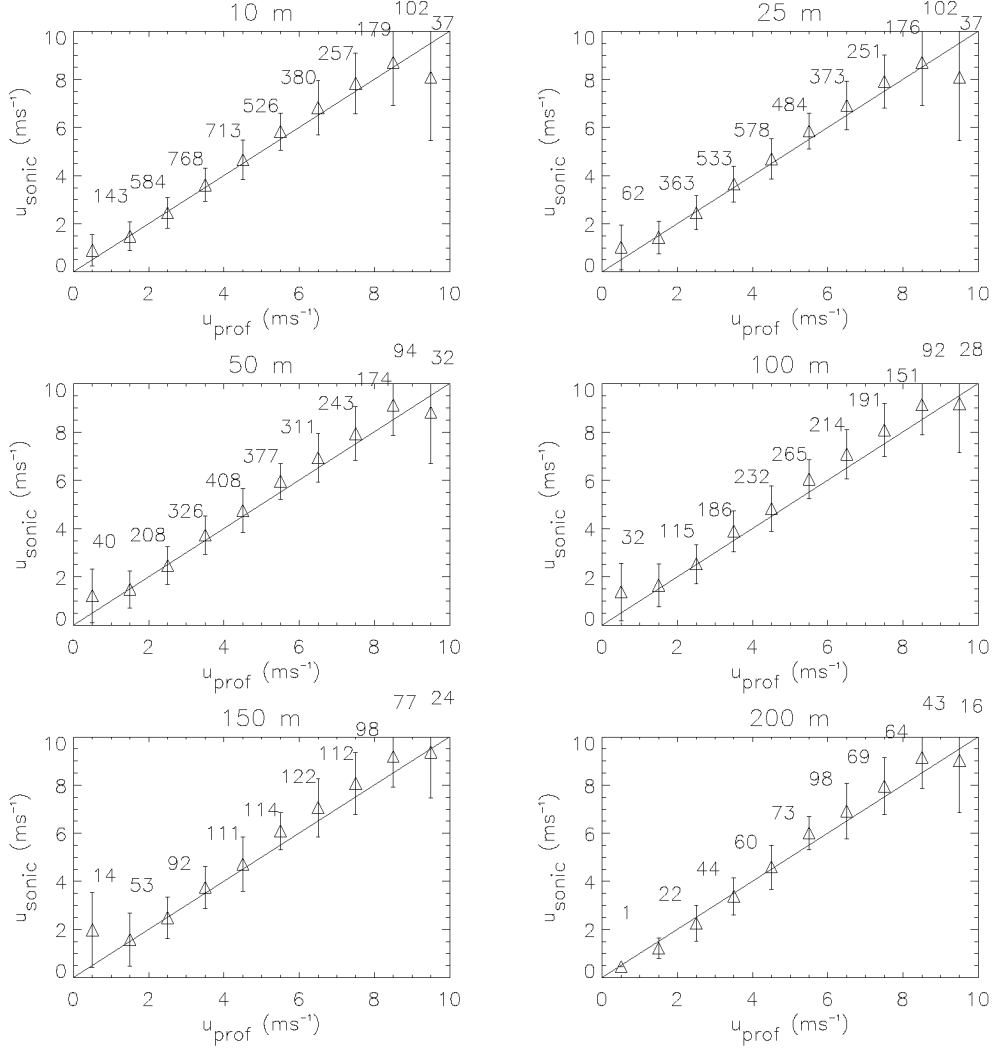
Figure 2.7: Sonic windspeed (u_{sonic}) versus propeller anemometer windspeed (u_{prof}) for each level for May 1997. Measurements are based on 30 minute means. The bars show the standard deviation in the measurements. The numbers in the plots represents the number of values used in each "bin". Units in m s^{-1}.

Figure 2.8 shows the sonic temperature (T_{sonic}) compared to the Pt-100 temperature (T_{prof}) for each level for May 1997. Here, it is important to note that the sonic temperature does not have a realistic magnitude. Since only the fluctuation in temperature is important for flux determination using the eddy correlation method, measurements of temperature using the sonic were manually constrained between -10°C and +10°C. The difficulty with comparing T_{prof} and T_{sonic}, however, is that the manual adjustment carried out at MRI was not documented, making it difficult to readjust sonic temperatures. The fact that some levels (10 m and 25 m) consistently show lower values for the sonic than for the Pt-100, and that other levels (200 m) consistently show higher values could be due to this procedure and not a

cause of instrumental problems. However, it is still apparent that most levels do show good agreement between instruments.
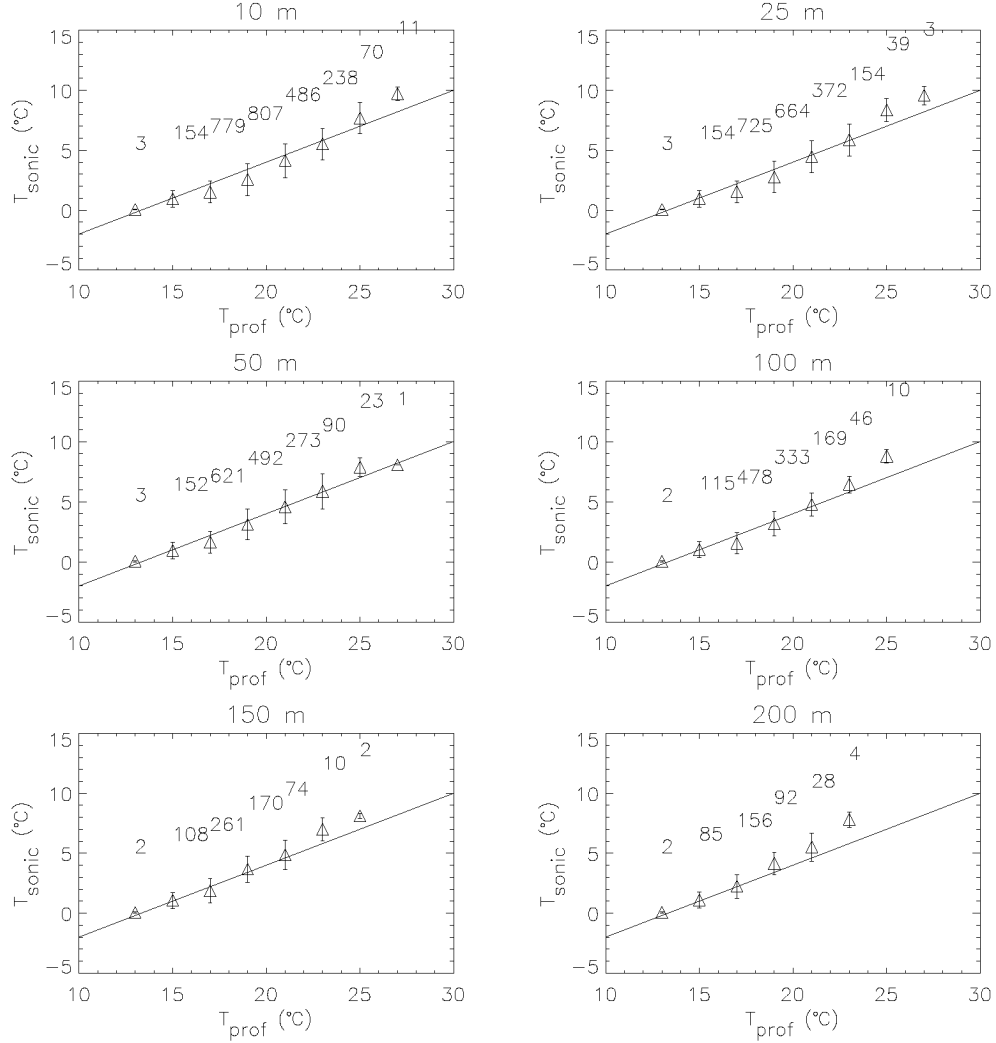
Figure 2.8: Sonic temperature (T_{sonic}) versus Pt-100 temperature (T_{prof}) for each level for May 1997 based on 30 minute means. The bars show the standard deviation in the measurements. The numbers in the plots represents the number of values used in each "bin". Units in ^oC.

For the determination of the gradients of windspeed (Figure 2.9), temperature (Figure 2.10) and humidity (Figure 2.12), curves were fitted through the profile measurements and the derivative with respect to height, z was then determined at the level of interest. A number of interpolation schemes were tested, including:

$$x(z) = a \left(\ln z \right)^2 + b \ln z + c, \qquad (2.3)$$
$$x(z) = a \ln z + bz + c, \qquad (2.4)$$
$$x(z) = az^2 + bz + c, \qquad (2.5)$$
$$x(z) = az + b, \qquad (2.6)$$

where $x(z)$ is the windspeed, temperature or humidity with respect to height z. Each approach was visually inspected to determine the curve of best fit. For each of the three variables, Equation 2.4 provided the best fit.

Figure 2.9 shows the mean windspeed profiles for May 1997 from the propeller anemometer. The average windspeed at MRI is typically quite low compared to other sites. For instance, the 25 m windspeed in May 1997 rarely reaches more than 5 m s^{-1}.

Figure 2.10 shows the mean temperature profiles for May 1997 from the Pt-100. As can be seen in the figure, the temperature profile is stable during the night (time 03:00), then increases in instability during the day (times 09:00 and 15:00) and returns to the stable case at time 21:00. Although not shown here, it is interesting to note that 22 of the 31 days in May 1997 actually show slightly unstable conditions, rather than stable, during the night. This is due to two reasons: Very cold air above intense cloud cover and cold air advection from the north east. However, the remaining 9 days are strongly stable during the night and are the main influence on the monthly mean. The mean temperature in May 1997 is roughly 14°C during the night and reaches a maximum of approximately 20°C during the day (see also Table 2.3).

An important note is that the choice of levels used to determine the temperature gradient using Equation 2.4 has a large effect on the resulting sensible heat flux. For this study, the 25 m, 50 m and 150 m level were used to determine the temperature gradient (see the forthcoming section on Turbulent Fluxes for the resulting sensible heat flux). However, using other levels can produce markedly different values for the sensible heat flux. Figure 2.11 shows the largest (dashed line; which corresponds to the largest sensible heat flux) and smallest (dotted line; which corresponds to the smallest sensible heat flux) possible temperature gradients for 12:00 on the 1st May 1997. The solid line uses the best fit temperature gradient which produces a sensible heat flux that is close to the mean of all possible gradients. The levels used in the solid curve (25 m, 50 m and 150 m) were used throughout this study. For the largest temperature gradient, the resulting sensible heat flux is nearly 4 times larger than that resulting from the smallest temperature gradient. This shows the large range of values possible depending on which levels are used.

Figure 2.12 shows the mean specific humidity profile for May 1997 using the hygrometer. Of the three variables shown here, the humidity shows the most scatter
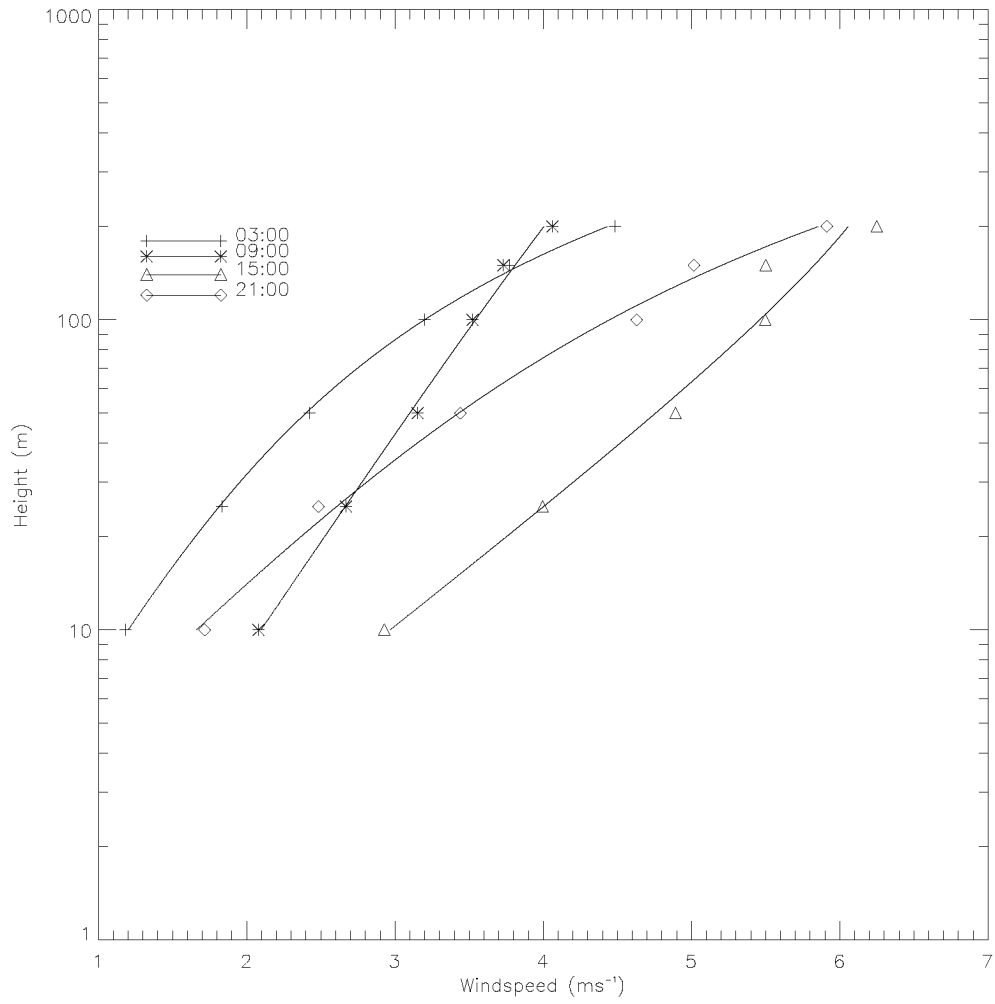
Figure 2.9: Mean profile of windspeed for May 1997 based on 30 minute means. The y axis is logarthmic. Units in m s^{-1}.
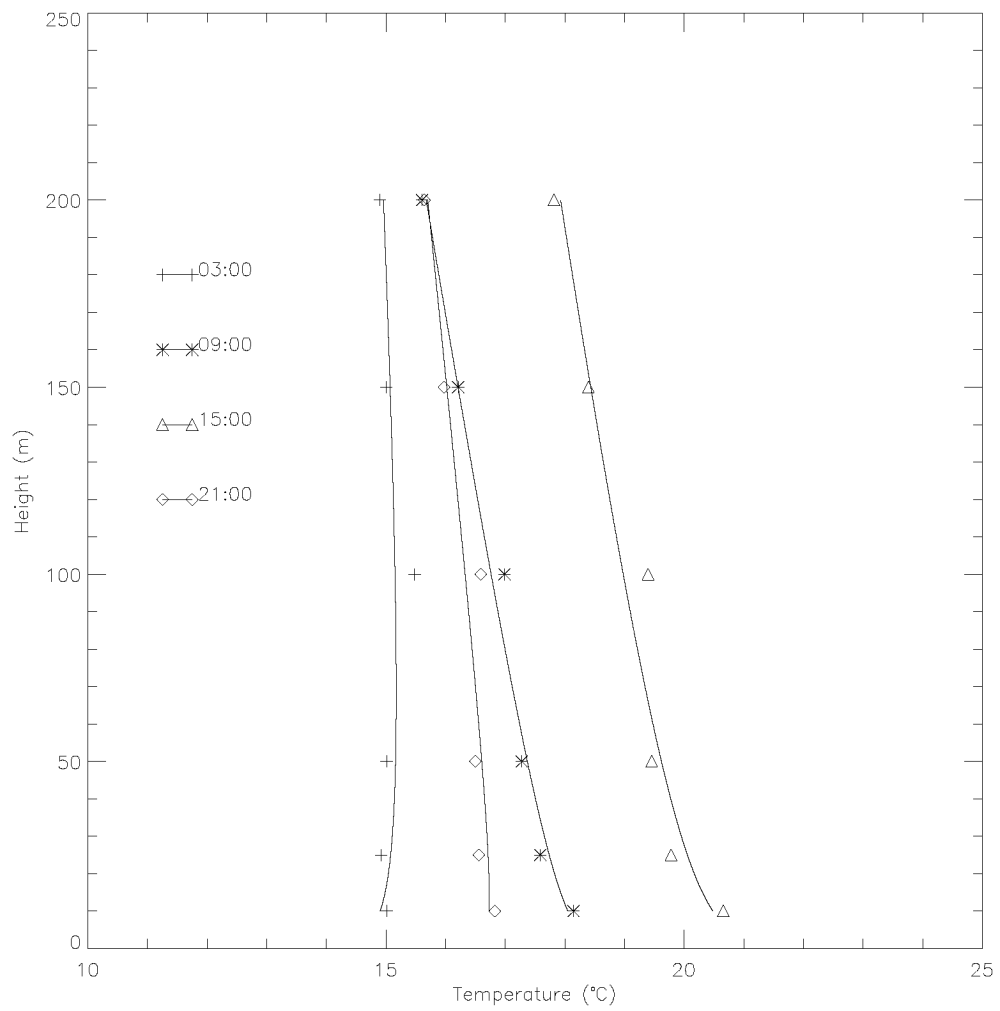
Figure 2.10: Mean profile for temperature in May 1997 based on 30 minute means. Units in ^oC.
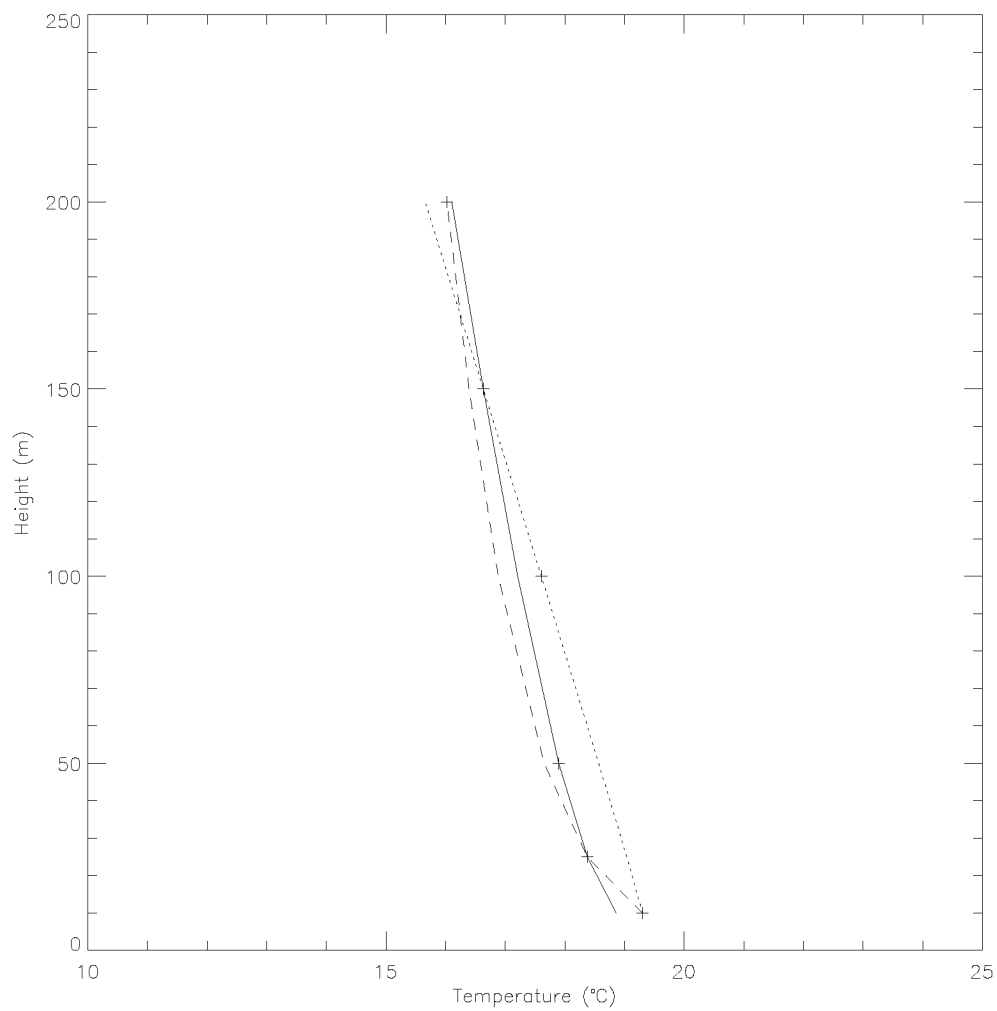
Figure 2.11: Profile for temperature at 12:00 on the 1st May 1997 based on 30 minute means. The solid line uses the 25 m, 50 m and 150 m levels, the dotted line uses the 10 m, 100 m and 150 m levels and the dashed line uses the 10 m, 25 m and 200 m levels. Units in ^{o}C.

with height. However, it is still obvious that Equation 2.4 fits the measurements with reasonable accuracy.
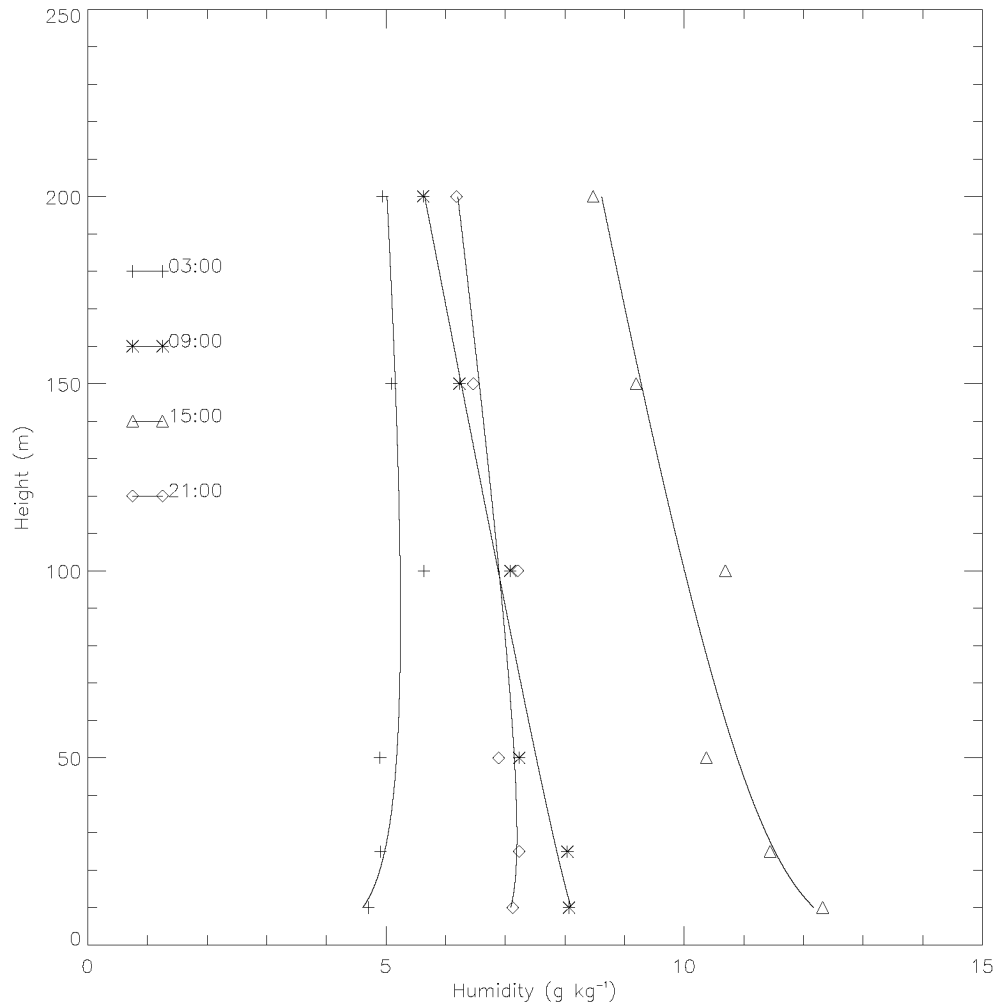
Figure 2.12: Mean profile for specific humidity in May 1997 based on 30 minute means. Units in g kg^{-1}.

Flux Determination at MRI, Tsukuba using the Profile Method

The profile method has the advantage that measurements are easy and relatively inexpensive to obtain (when compared to sonic measurements), and that it can be applied in models such as GCMs. The profile method is based on Monin-Obukhov theory, which relates the turbulent fluxes to the scaling parameters u_*, θ_* and q_*, as well as to the height above the ground, z and the buoyancy parameter $(g/\overline{\theta})$. Equations 2.7−2.9 show the relationship between these scaling parameters and the fluxes. Here, positive fluxes are directed downwards.

$$M = \rho\, u_*^2, \tag{2.7}$$

$$H_s = \rho\, C_p\, u_*\, \theta_*, \tag{2.8}$$

$$L_v E = \rho\, L_v\, u_*\, q_*, \tag{2.9}$$

where M is the momentum flux (N m^{-2}), H_s is the sensible heat flux (W m^{-2}), $L_v E$ is the latent heat flux (W m^{-2}), ρ is the density of air (kg m^{-3}), C_p is the specific heat of air at constant pressure (J kg^{-1} K^{-1}), u_* is the friction velocity, θ_* is the temperature scale and q_* is the humidity scale. These scaling parameters can be determined by two main approaches: Iteratively and analytically, and will be discussed in more detail in the following sections.

Iterative Procedure using Beljaars and Holtslag (1991)   The first method to determine the turbulent fluxes rewrites the equations from Monin-Obukhov theory to incorporate the integrated Monin-Obukhov functions (Equations 2.10−2.12). In this study, the functions from Beljaars and Holtslag (1991) in Equations 2.13 and 2.14 are used. The values of u_*, θ_*, q_* and L are determined through iteration.

$$\frac{M}{\rho\, u_*} = u_* = \frac{k\,(\overline{U}_2 - \overline{U}_1)}{\ln\!\left(\frac{z_2}{z_1}\right) - \psi_m\!\left(\frac{z_2}{L}\right) + \psi_m\!\left(\frac{z_1}{L}\right)}, \tag{2.10}$$

$$\frac{H_s}{\rho\, C_p\, u_*} = \theta_* = \frac{k\,(\overline{T}_2 - \overline{T}_1)}{\ln\!\left(\frac{z_2}{z_1}\right) - \psi_h\!\left(\frac{z_2}{L}\right) + \psi_h\!\left(\frac{z_1}{L}\right)}, \tag{2.11}$$

$$\frac{L_v E}{\rho\, L_v\, u_*} = q_* = \frac{k\,(\overline{q}_2 - \overline{q}_1)}{\ln\!\left(\frac{z_2}{z_1}\right) - \psi_q\!\left(\frac{z_2}{L}\right) + \psi_q\!\left(\frac{z_1}{L}\right)}, \tag{2.12}$$

where k is the von Kármán constant (k=0.4), U_1 and U_2 are the windspeeds (m s^{-1}), T_1 and T_2 are the temperatures (K) and q_1 and q_2 are the humidities (kg kg^{-1}) at heights z_1 and z_2 (m), respectively. The overbar denotes the 30 minute mean values of each quantity. L is the Obukhov length (m). The parameters ψ_m, ψ_h and ψ_q are integrated Monin-Obukhov functions for momentum, sensible heat and latent heat, respectively (Equations 2.13 and 2.14).

$$\psi_m = \begin{cases} 2\,ln(\frac{1+x}{2}) + ln(\frac{1+x^2}{2}) - 2\tan^{-1}(x) + \frac{\pi}{2} & \text{if } \frac{z}{L} < 0 \\ -0.7\frac{z}{L} - 10.72 & \text{if } \frac{z}{L} > 200 \\ -0.7\frac{z}{L} - (0.75\frac{z}{L} - 10.72)\exp(-0.35\frac{z}{L}) - 10.72 & \text{if } 0 \le \frac{z}{L} \le 200, \end{cases} \quad (2.13)$$

$$\psi_{h,q} = \begin{cases} 2\ln(\frac{1+y}{2}) & \text{if } \frac{z}{L} < 0 \\ -0.7\frac{z}{L} - (0.75\frac{z}{L} - 10.72)\exp(-0.35\frac{z}{L}) - 10.72 & \text{if } \frac{z}{L} \ge 0, \end{cases} \quad (2.14)$$

where $x = (1 - 16\frac{z}{L})^{\frac{1}{4}}$ and $y = (1 - 16\frac{z}{L})^{\frac{1}{2}}$.

From Equations 2.10−2.12, a new estimate of L can be determined by

$$L = \frac{\overline{T}\,u_*^2}{k\,g\,\theta_*}, \tag{2.15}$$

where g is the acceleration due to gravity (9.81 m s^{-2}). This procedure is continued until L converges.

It is important to note that the higher levels of the tower may occassionally be located above the constant flux layer, leading to a breakdown of surface similarity theory and, thus, erroneous values for the fluxes.

Analytical Procedure using Högström (1996)   The second method for determining the scaling parameters using Monin-Obukhov (MO) theory (Equation 2.7−2.9) uses the Gradient Richardson Number (Ri) to determine the universal functions (ϕ_m and ϕ_h). In this study, the universal functions of Beljaars and Holtslag (1991) are not used since their differential form is difficult to solve. However, various other relationships have been suggested by Högström (1996), Businger et al. (1971), Dyer (1974), Dyer and Bradley (1982), Foken and Skeib (1983) and others. Here, the relationships of Högström (1996) are used.

Here, the determination of u_*, θ_* and q_* is completed using Equations 2.16−2.18.

$$u_* = \frac{k\,z}{\phi_m}\frac{\partial \overline{U}}{\partial z}, \tag{2.16}$$

$$\theta_* = \frac{k\,z}{\phi_h}\frac{\partial \overline{T}}{\partial z}, \tag{2.17}$$

$$q_* = \frac{k\,z}{\phi_h}\frac{\partial \overline{q}}{\partial z}, \tag{2.18}$$

where the non-dimensional wind and temperature profiles, ϕ_m and ϕ_h, respectively, are derived from Högström (1996), as seen in Equations 2.19−2.22.

For unstable conditions,

$$\phi_m = (1 - 19\frac{z}{L})^{-\frac{1}{4}}, \tag{2.19}$$

$$\phi_h = 0.95\,(1 - 11.6\frac{z}{L})^{-\frac{1}{2}}, \tag{2.20}$$

23

For stable conditions,

$$\phi_m = 1 + 5.3\,\frac{z}{L}, \tag{2.21}$$

$$\phi_h = 1 + 8\,\frac{z}{L}, \tag{2.22}$$

where z/L is determined from Equation 2.23.

$$Ri = \frac{g}{\overline{T}}\,\frac{(\frac{\partial \overline{T}}{\partial z} + \Gamma_d)}{(\frac{\partial \overline{u}}{\partial z})^2 + (\frac{\partial \overline{v}}{\partial z})^2} = \frac{\phi_h}{\phi_m^2}\,\frac{z}{L}, \tag{2.23}$$

and Γ_d is the dry adiabatic lapse rate (0.976°C/100 m), and u and v are the eastward and northward components of velocity (m s^{-1}), respectively.

This method has the advantage over the above method that it calculates the turbulent fluxes directly, omitting the need for iteration. It is important to note, however, that this method is only applicable for horizontal homogeneity and a stationary constant flux layer. Here, stationarity is defined where all the conditions governing the process are time-independent.

Analytical Procedure using New Equations The equations of Högström (1996) were used in this study as a first approximation of using Ri to determine ϕ_m and ϕ_h and, consequently, the fluxes. However, while the equations of Högström (1996) are widely accepted, they may not be the most representative of the observations at this particular site. Figures 2.13 and 2.14 show the universal functions compared to z/L for the 25 m level in May 1997.

Figure 2.13 shows the universal function for momentum, ϕ_m, versus z/L for the 25 m level in May 1997. The observations (plus signs) represent half hourly means derived from sonic measurements for the friction velocity, and the propeller anemometer for the windspeed gradient (see Equation 2.16). While it is apparent that the curve of Högström (1996) is similar to the observations, the measurements show values of ϕ_m which are systematically lower than Högström (1996). This conclusion was also found for other months at the 25 m level. Thus, new equations for ϕ_m were developed using regression analyses to remove this systematic bias (Equations 2.24 and 2.26).

Figure 2.14 shows ϕ_h versus z/L for the 25 m level in May 1997. Similarly to the above figure, the temperature scale for the half hourly mean measurements (plus signs) is determined from the sonics whereas the temperature gradient is determined from the Pt-100 (Equation 2.17). Here, the observations seem to systematically overestimate the equations for ϕ_h from Högström (1996). This was also found to be the case for other months at the 25 m level. Hence, new equations for ϕ_h were developed to remove this systematic bias, as shown in Equations 2.25 and 2.27.

For unstable conditions,

$$\phi_m = 0.85\,(1 - 19\,\frac{z}{L})^{-\frac{1}{4}}, \tag{2.24}$$

$$\phi_h = 1.7\,(1 - 10\,\frac{z}{L})^{-\frac{1}{2}}. \tag{2.25}$$
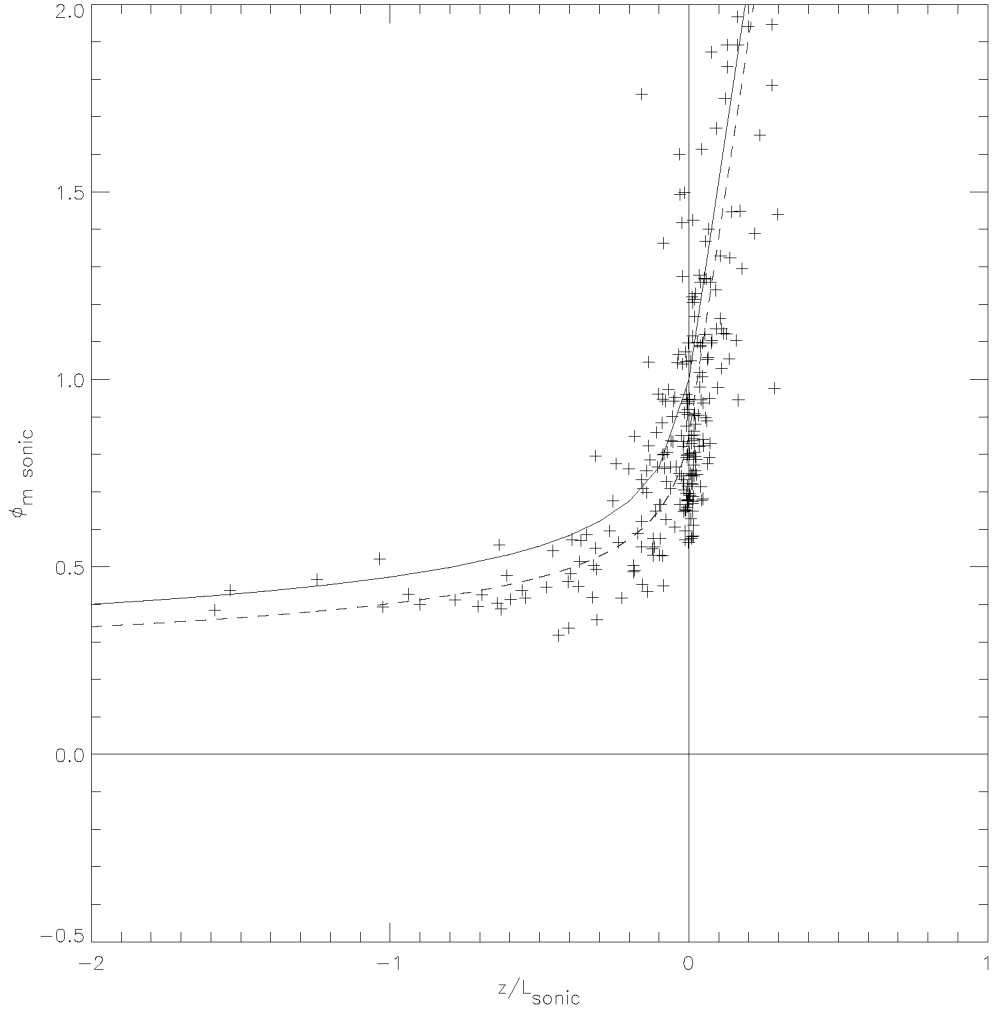
24

Figure 2.13: ϕ_m versus z/L for the 25 m level in May 1997. The '+' indicates half hourly mean measurements from the sonics with the windspeed gradient determined from the propeller anemometer. The solid line represents the equations of Högström (1996), the dashed line shows the new equations derived for this study.

For stable conditions,

$$\phi_m = 0.85 + 5.3\frac{z}{L}, \tag{2.26}$$

$$\phi_h = 1.7 + 6.9\frac{z}{L}. \tag{2.27}$$

Equations 2.24−2.27 are then used in Equations 2.16−2.18 to determine the fluxes. As with the above method, these equations are only applicable for horizontal homogeneity and a stationary constant flux layer.

It is important to note, however, that the new equations developed here appear to be dependent on the roughness elements, and would be difficult to apply to other sites. Even at MRI, these new equations for ϕ_m and ϕ_h are only applicable at certain levels. For the 10 m level, for example, the equations for ϕ_m and ϕ_h from Högström (1996) appear to be more representative than the new equations (see Figures 2.15 and 2.16). This shows the difference between skin (local) roughness and form (areal) roughness. While the 25 m level may be defined by a universal function which depends on the large scale roughness of the site, it is possible that the 10 m level may be defined by a universal function which depends on the small scale roughness. This is an interesting conjecture since it proves that the equations of Högström (1996), and other studies listed in the previous section, are only applicable when developing equations not affected by internal boundary layers. Since the site at MRI is affected by internal boundary layers, the new equations are deemed more representative. The determination of dimensionless gradients that are not roughness dependent is a difficult undertaking. It may be possible to derive a set of equations for the universal functions that are dependent on the heterogeneity of the site, but this prospect is beyond the scope of this work.

Figures 2.17 and 2.18 show the differences between the new equations developed for this study, the equations of Högström (1996) and the equations of Beljaars and Holtslag (1991) for the 25 m level for May 1997 for momentum and heat, respectively. In Figure 2.17, it is apparent that all curves are similar, particularly in stable cases. For unstable cases, the curves of Högström (1996) and Beljaars and Holtslag (1991) agree well, while the new equations produce slightly lower values. For Figure 2.18, the difference is more significant. In this figure, the curves of Högström (1996) and Beljaars and Holtslag (1991) agree well for unstable cases, but separate in stable cases. The new equations produces values which are markedly higher than Högström (1996) and Beljaars and Holtslag (1991) in unstable cases, although the new equations converge towards Högström (1996) in strongly stable situations. These figures show the differences between the universal functions adopted for this study. Of these equations, the new equations provide the best fit to the data, omitting systematic biases from the measurements as seen in Högström (1996) and Beljaars and Holtslag (1991).
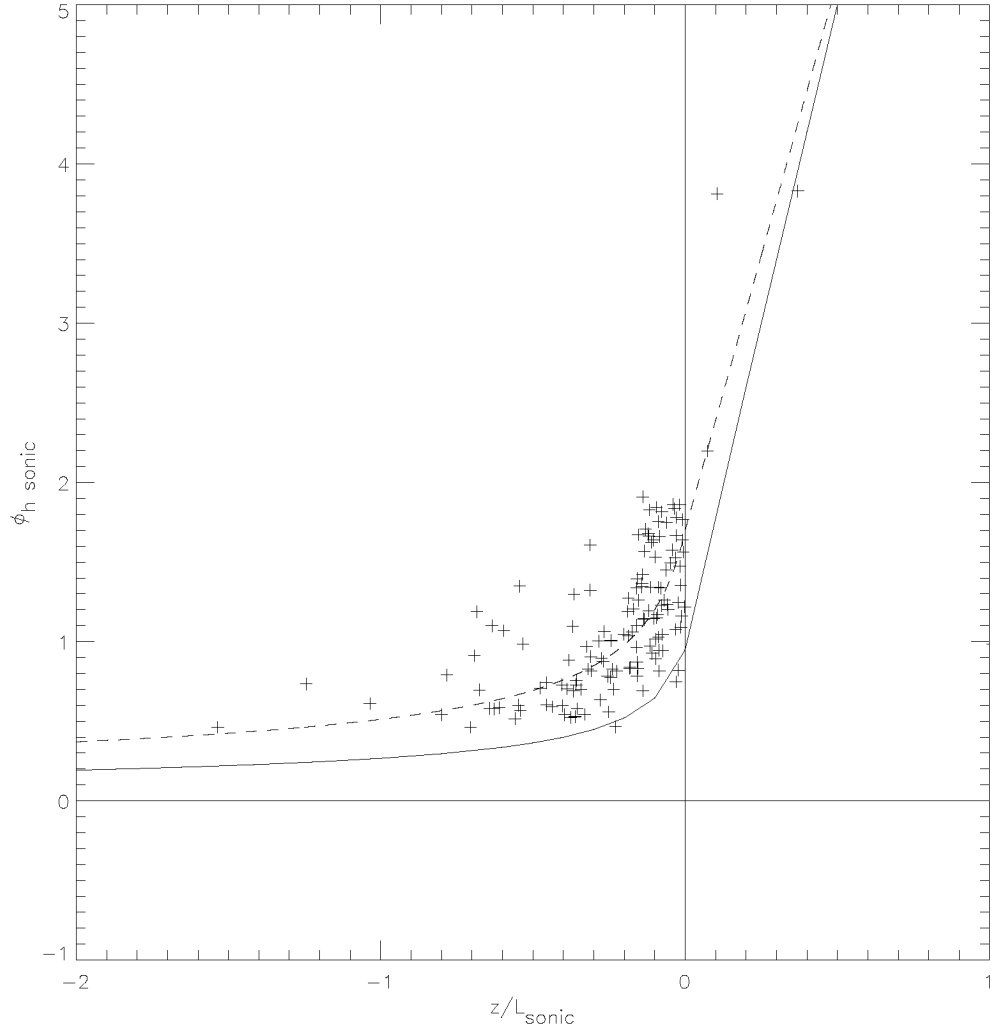
Figure 2.14: ϕ_h versus z/L for the 25 m level in May 1997. The '+' indicates half hourly mean measurements from the sonics with the temperature gradient determined from the Pt-100. The solid line represents the equations of Högström (1996), the dashed line shows the new equations derived for this study.
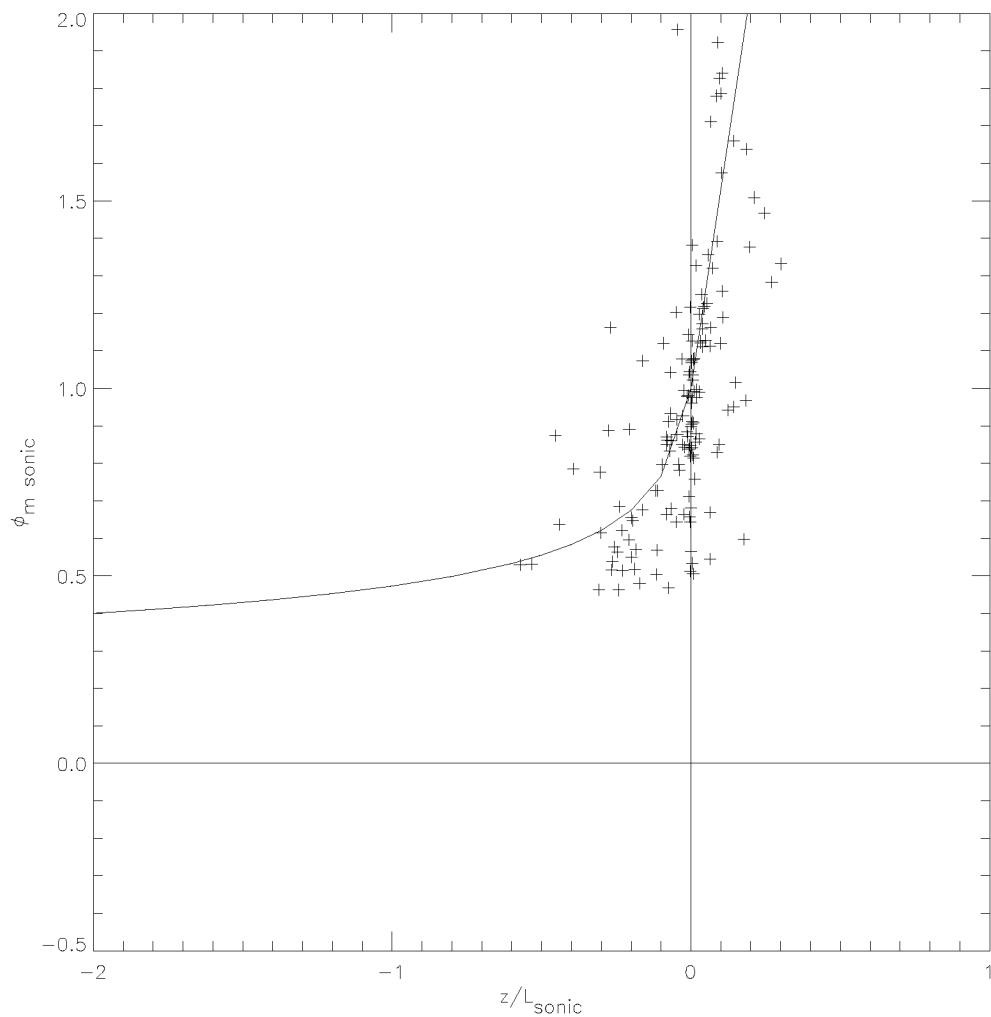
Figure 2.15: ϕ_m versus z/L for the 10 m level in May 1997. The '+' indicates half hourly mean measurements from the sonics with the windspeed gradient determined from the propeller anemometer. The solid curve represents the equations of Högström (1996).
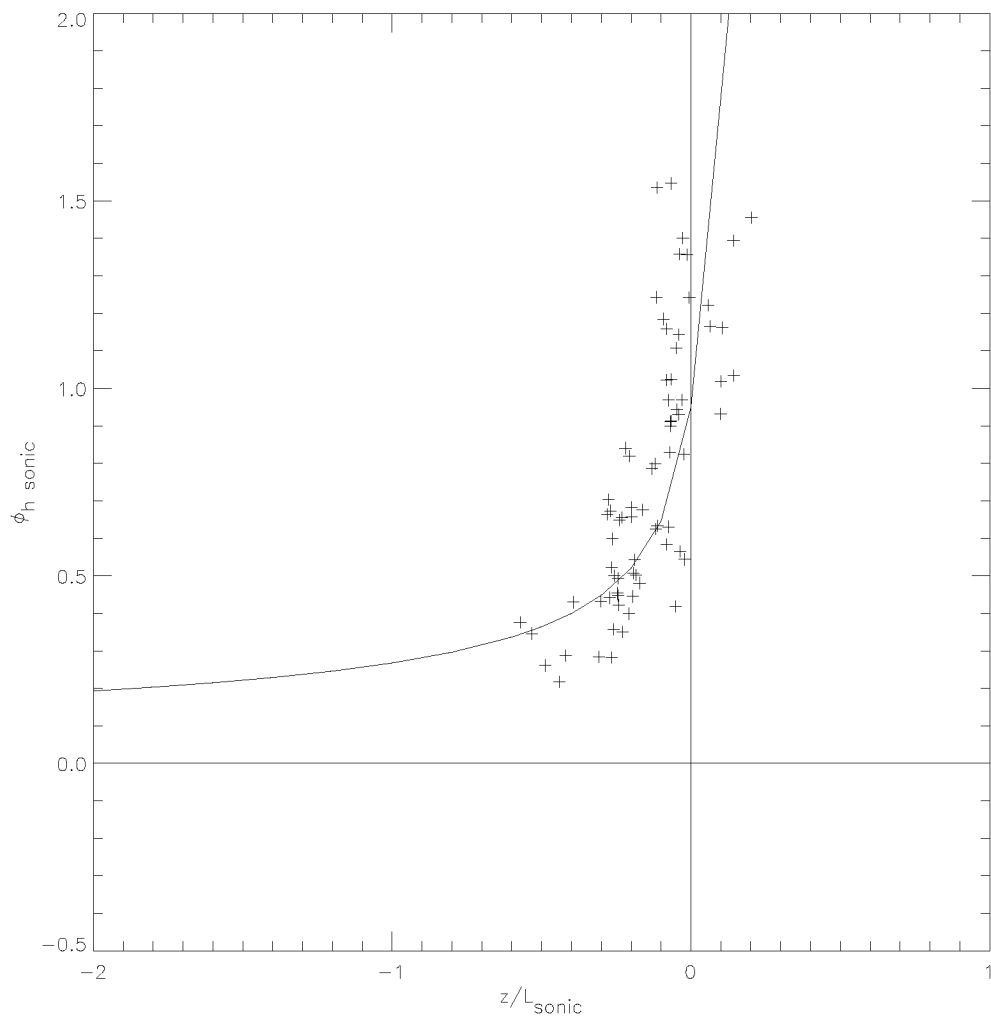
Figure 2.16: ϕ_h versus z/L for the 10 m level in May 1997. The '+' indicates half hourly mean measurements from the sonics with the temperature gradient determined from the Pt-100. The solid curve represents the equations of Högström (1996).
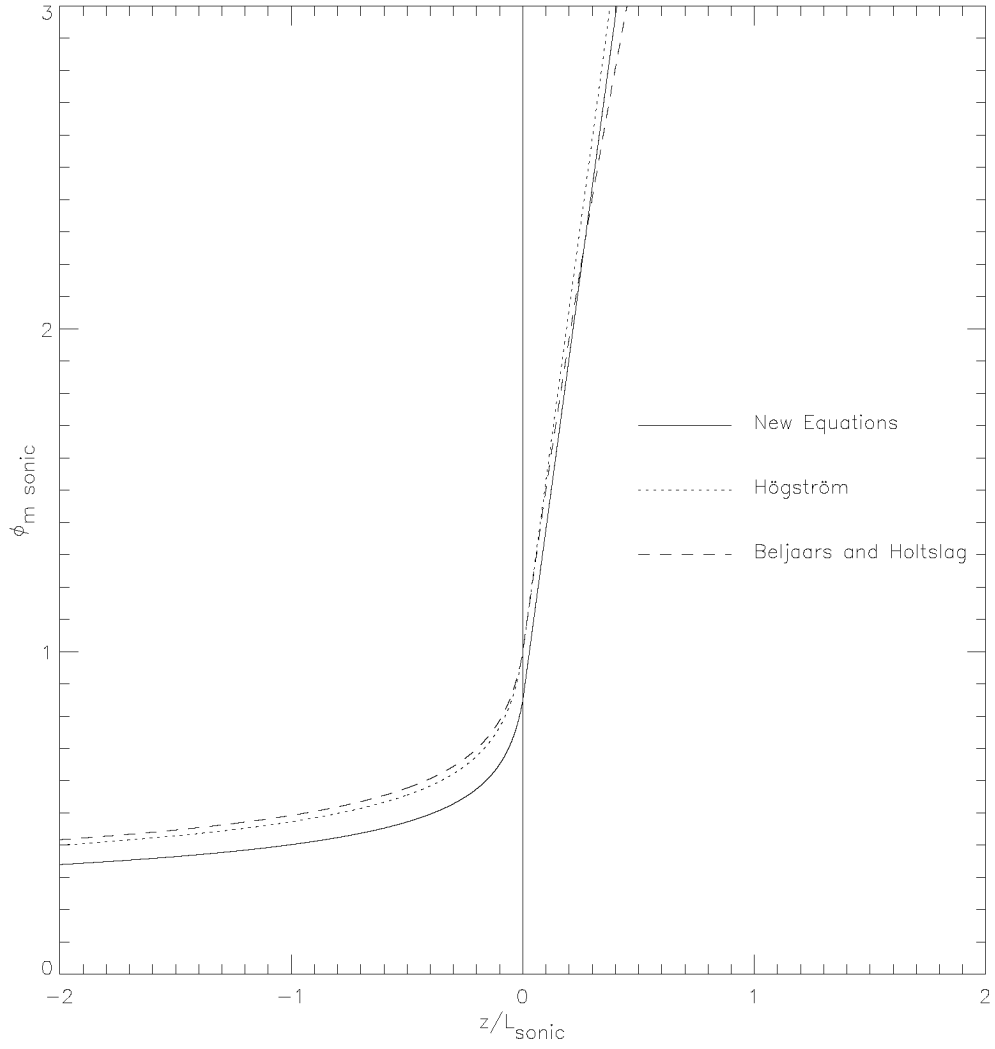
Figure 2.17: ϕ_m versus z/L for the 25 m level in May 1997. The solid curve represents the new equations derived for this study, the dotted line represents the equations of Högström (1996) and the dashed line represents the equations of Beljaars and Holtslag (1991).

30
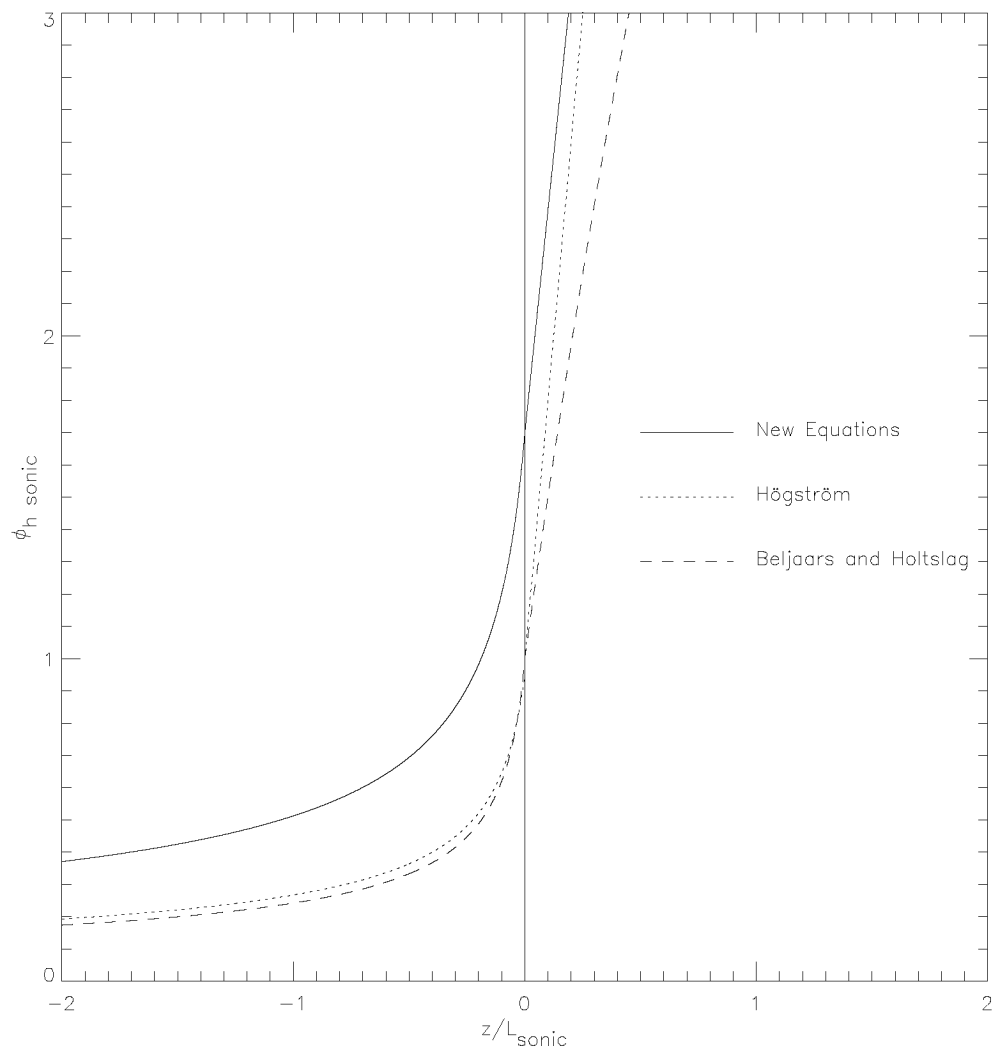
Figure 2.18: ϕ_h versus z/L for the 25 m level in May 1997. The solid curve represents the new equations derived for this study, the dotted line represents the equations of Högström (1996) and the dashed line represents the equations of Beljaars and Holtslag (1991).

Analytical Procedure using Modified New Equations As a fourth approach, the above method (New Equations) can be used with one alteration: Determining Ri from the Flux Richardson Number (R_f). Since the MRI, Tsukuba tower measures sonic data as well as profile measurements, it is possible to use the sonic windspeed and temperature to determine R_f (Equation 2.28).

$$R_f = -\frac{g}{\overline{T}} \frac{\overline{w'T'}}{\sqrt{(\overline{u'w'} \frac{\partial u}{\partial z})^2 + (\overline{v'w'} \frac{\partial v}{\partial z})^2}}, \tag{2.28}$$

where w is the vertical component of velocity (m s^{-1}) and the prime indicates the fluctuating component of the variable.

This Flux Richardson Number is then converted into the Gradient Richardson Number for adaptation into the above method (Equation 2.29).

$$Ri = \frac{K_m}{K_h} R_f, \tag{2.29}$$

where K_m and K_h are the eddy diffusivities for momentum and heat, respectively. For this study, it was found that $K_m = K_h$ for neutral and stable conditions, and $K_m = 0.74 K_h$ for unstable conditions. This new Gradient Richardson Number is then implemented with the equations from the section above to produce a modified version of the new equations.

As with the above methods, this method is only valid for horizontal homogeneity and a stationary constant flux layer.

Analytical Procedure using Sonic Fluxes Instead of Ri The fifth option for determining the turbulent fluxes using the analytical approach involves the use of sonic output to determine z/L (Equation 2.30). Here, Ri is no longer needed. This method has the advantage of being a more straightforward means to determine the turbulent fluxes.

$$\frac{z}{L} = -k\,g\,z\,\frac{\frac{H_{ssonic}}{\rho\,C_p}}{\overline{T}\,(u_{*sonic})^3}, \tag{2.30}$$

where H_{ssonic} is the sensible heat flux (W m^{-2}) and u_{*sonic} is the friction velocity both determined using the eddy correlation method (see the following section). Equations 2.16−2.18 are then used in conjunction with

1. the equations of Högström (1996) (Equations 2.19−2.22), or

2. the new equations derived for this study (Equations 2.24-2.27)

to determine the scaling parameter and, thus, the turbulent fluxes.

As with the previous method, this method is only valid for horizontal homogeneity and a stationary constant flux layer.

Flux Determination at MRI, Tsukuba using the Eddy Correlation Method

Since the Tsukuba tower is surrounded by surfaces with non-uniform characteristics such as trees and buildings, it is likely that the vector quantities such as velocity or fluxes are measured in a reference framework that does not coincide with that of the equations used to analyse them. To deal with this difficulty, coordinate rotations are performed to mathematically transform the measurements from the reference frame of the instrument into a chosen frame of optimum orientation, i.e. into the flow direction. This approach is based on the methods of Kaimal and Finnigan (1994) and has been tested and verified in Cassardo et al. (1995).

The first step is to reorientate the sonic plane (with 120° angles between the a and b horizontal probes) onto a 90° plane. During this transformation, the x and y axes are also rotated to geographical east and north, respectively. These transformations change with regard to the arm used for measurements, as seen in Equations 2.31−2.36.

For the NW arm,

$$u = \frac{2\,b + a}{\sqrt{3}}, \tag{2.31}$$

$$v = -a. \tag{2.32}$$

For the NE arm,

$$u = \frac{2\,a + b}{\sqrt{3}}, \tag{2.33}$$

$$v = -b. \tag{2.34}$$

For the S arm,

$$u = \frac{(a - b)}{\sqrt{3}}, \tag{2.35}$$

$$v = a + b, \tag{2.36}$$

where a is the windspeed from the a probe, b is the windspeed from the b probe, and v and u are the windspeeds using a north east coordinate system, respectively.

The next step is to average the time series of velocities to produce a mean wind vector $\overline{\mathbf{u}}_{\mathbf{a}}$, with components $\overline{u}_1$, $\overline{v}_1$, $\overline{w}_1$. The averaging period must be long enough to obtain a valid statistical value from two inherently noisy signals, yet short enough to assume weak stationarity of meteorological conditions. In this study, a 30 minute averaging period was selected based on the discussion by McMillen (1988). The differences between using 30 minute mean and 60 minute mean measurements can be seen in Figures 2.19 and 2.20. Figure 2.19 shows 2 half hourly mean sonic measurements averaged to one hour compared to hourly mean sonic measurements for windspeed in May 1997 for each level. It is obvious that, while the majority of the measurements are the same, there are also some differences, particularly at low windspeeds. It is difficult to prescribe the reason for these difference to non-stationarity,

33

which will be discussed in more detail in the following chapter, since the same figure for temperature (Figure 2.20) shows perfect agreement. Non-stationarity would have an affect on temperature as well as windspeed. Instead, it is possible that the difference in Figure 2.19 is due to inaccuracies in the windspeed instruments themselves.
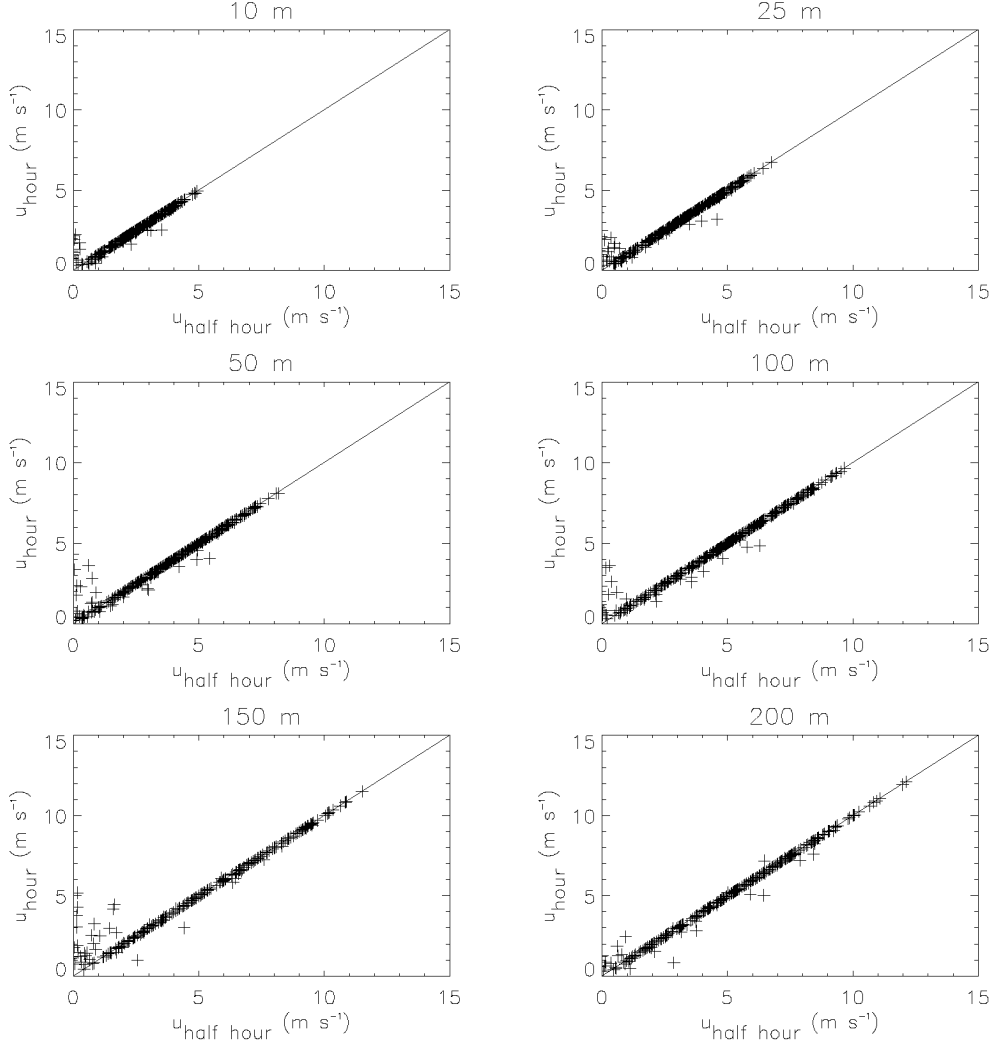
Figure 2.19: Mean hourly sonic windspeed versus 2 half hourly mean sonic windspeeds averaged over 1 hour for each level at MRI for May 1997. Units in m s^{-1}.

The first transformation rotates the x_1 and y_1 axes around z_1 to produce a new set of axes (x_2, y_2, z_2). From this, the new mean wind vector $\overline{\mathbf{u}}_\mathbf{b}$ with components $\overline{u}_2$, $\overline{v}_2$, $\overline{w}_2$ is determined using Equation 2.37. This coordinate rotation forces $\overline{v}_2 = 0$, but the vertical component remains unaffected.

$$\overline{\mathbf{u}}_\mathbf{b} = C\,\overline{\mathbf{u}}_\mathbf{a}, \tag{2.37}$$

where $C = \begin{bmatrix} \cos\alpha & \sin\alpha & 0 \\ -\sin\alpha & \cos\alpha & 0 \\ 0 & 0 & 1 \end{bmatrix}$,
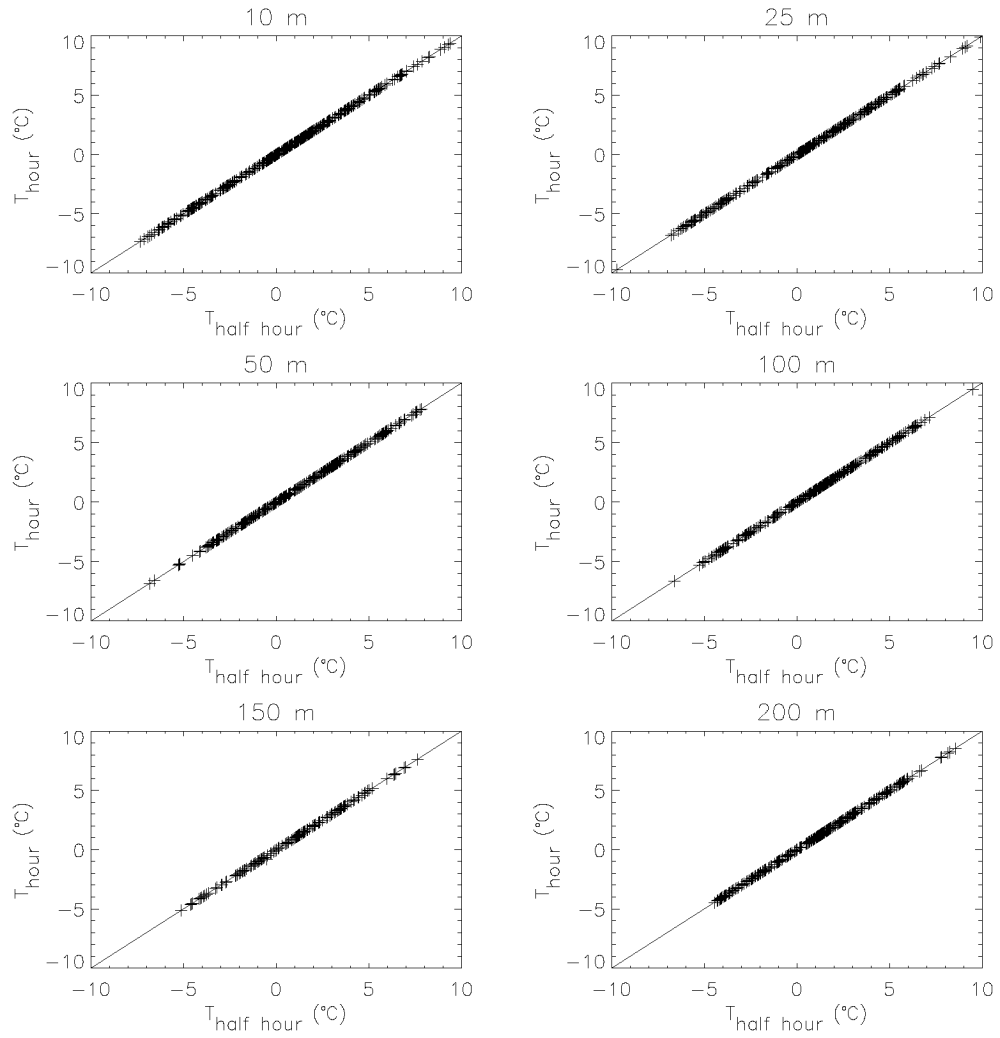
Figure 2.20: Mean hourly sonic temperature versus 2 half hourly mean sonic temperatures averaged over 1 hour for each level at MRI for May 1997. Units in ºC.

$\alpha = \tan^{-1}\left(\frac{\overline{v}_1}{\overline{u}_1}\right).$

The second transformation rotates x_2 and z_2 around y_2 to form the new axes (x_3, y_3, z_3). This rotation points x_3 along the mean wind direction. From this, the new mean wind vector $\overline{\mathbf{u}}_{\mathbf{c}}$ with components $\overline{u}_3$, $\overline{v}_3$, $\overline{w}_3$ is determined using Equation 2.38. This rotation forces $\overline{w}_3 = 0$. After these rotations, the coordinate system follows the transport direction which is aerodynamically normal to the effective earth's surface.

$$\overline{\mathbf{u}}_{\mathbf{c}} = D\,\overline{\mathbf{u}}_{\mathbf{b}}, \tag{2.38}$$

$$\text{where } D = \begin{bmatrix} \cos\beta & 0 & \sin\beta \\ 0 & 1 & 0 \\ -\sin\beta & 0 & \cos\beta \end{bmatrix},$$

$\beta = \tan^{-1}\left(\frac{\overline{w}_2}{\overline{u}_2}\right).$

The alignment of the coordinate system with the average wind vector, however, does not make any constraints on the y and z axes; only the x axis is fixed. There exist 3 methods of locating v and w: Transform w such that the $w - u$ plane is tangential to the geopotential vertical; transform w such that the $w - u$ plane is perpendicular to the ground surface, or; force the $\overline{v'w'}$ covariance to zero. The third alternative is used in this study since it forces the w' covariances to correspond to a vector normal to the streamline rather than to a geopotential vertical. If $\overline{v_2 w_2} = 0$, no rotation is needed and the angle of rotation is 45° if $\overline{v_2{}^2} = \overline{w_2{}^2}$. From this, the fully rotated mean wind vector $\overline{\mathbf{u}}$ with the components $\overline{u}$, $\overline{v}$, $\overline{w}$ is determined using Equation 2.39. It is important to note, however, that this rotation should only be used when z_3 is within 10° of the vertical.

$$\overline{\mathbf{u}} = E\,\overline{\mathbf{u}}_{\mathbf{c}}, \tag{2.39}$$

$$\text{where } E = \begin{bmatrix} 1 & 0 & 0 \\ 0 & \cos\varphi & \sin\varphi \\ 0 & -\sin\varphi & \cos\varphi \end{bmatrix},$$

$\varphi = \frac{1}{2}\tan^{-1}\left(\frac{2\overline{v_3 w_3}}{\overline{v_3{}^2} - \overline{w_3{}^2}}\right).$

For cases of non-stationarity, the running mean, determined from a digital recursive filter, is subtracted from the incoming data. In this study, a filter of 200 seconds is used, as suggested by McMillen (1988).

Lastly, a run test is applied to the data to check each half hour averaging period and each component for stationarity (Bendat and Piersol, 1986). Here, each averaging period is divided into forty subintervals. The variance of the variable (e.g. $\sigma_u{}^2$ for the variance of the east windspeed component) for these subintervals is then compared to the variance of the entire averaging period (e.g. $\overline{\sigma_u}^2$) and is classified into one of two categories (e.g. $\sigma_u{}^2 \leq \overline{\sigma_u}^2$ or $\sigma_u{}^2 \geq \overline{\sigma_u}^2$). The number of times the observations change between categories is an indication of the randomness of the data. This procedure uses a t-test on the hypothesis that the variances of the subintervals are not independent random observations.

Using these corrections, the friction velocity can be determined by Equation 2.40. Consequently, the momentum flux and sensible heat flux can be determined using Equations 2.41 and 2.42.

$$u_*{}^2 = (\overline{u'w'}^2 + \overline{v'w'}^2)^{\frac{1}{2}}, \qquad (2.40)$$

$$M = \rho\, u_*{}^2, \qquad (2.41)$$

$$H_s = \rho\, C_p\, \overline{w'T'}, \qquad (2.42)$$

where the symbols have been described previously.

Scaling Parameters

As with the windspeed and temperature above, it is possible to compare the scaling parameters using the methods described above.

Figure 2.21 shows the friction velocity determined from the sonic compared to that using the analytical procedure with the Monin-Obukhov functions from the equations of Högström (1996) for May 1997. Data are binned. As can be seen, there is a large scatter between the methods. For the highest four levels, the scatter is substantial. At these heights, the measurements are sometimes affected by non-stationarity, leading to an inability of Monin-Obukhov theory to accurately represent the site. However, the rejection of measurements on the 50 m level and above is not detrimental to the comparison studies with the models. For instance, the lowest model level in ECHAM4 is 33 m, which compares well with the 25 m level of the MRI tower. Thus, the remainder of this section will predominantly discuss the 25 m level of the tower. For the 10 m and 25 m levels, the agreement between the eddy correlation method and profile method is good up to values of u$_*$ of approximately 0.6. At larger values, the overspeeding of the propeller anemometer causes an overestimation in u$_{*prof}$.

Figure 2.22 shows the friction velocity, u$_*$ using each of the methods discussed above for May 1997 for the 25 m level. Data are collocated into bins. In this figure, the most obvious cases of the propeller anemometer overspeeding are removed. Here, it is obvious that each method is comparable. The new equations and Högström (1996), when used in the analytical procedure, appear to show the best agreement. At low values, u$_*$ appears to be underestimated by the profile methods, except when implementing the new equations. For large values of u$_*$, each profile method tends to slightly overestimate the values. This is due to two reasons: The overspeeding of the propeller anemometer, as discussed previously, which can create anomolies in the windspeed gradient, leading to inaccuracies in u$_*$, and; inaccuracies in the windspeed gradient from the choice of levels used. This latter point is similar to the inaccuracy in the temperature gradient as shown in Figure 2.11.

Figure 2.23 shows the sonic temperature scale (θ_{*sonic}) versus the different methods of determining the temperature scale with the profile method (θ_{*prof}) at MRI for the 25 m level for May 1997 based on 30 minute means. Data are grouped into bins. For this variable, quite large differences can be seen between the methods. For
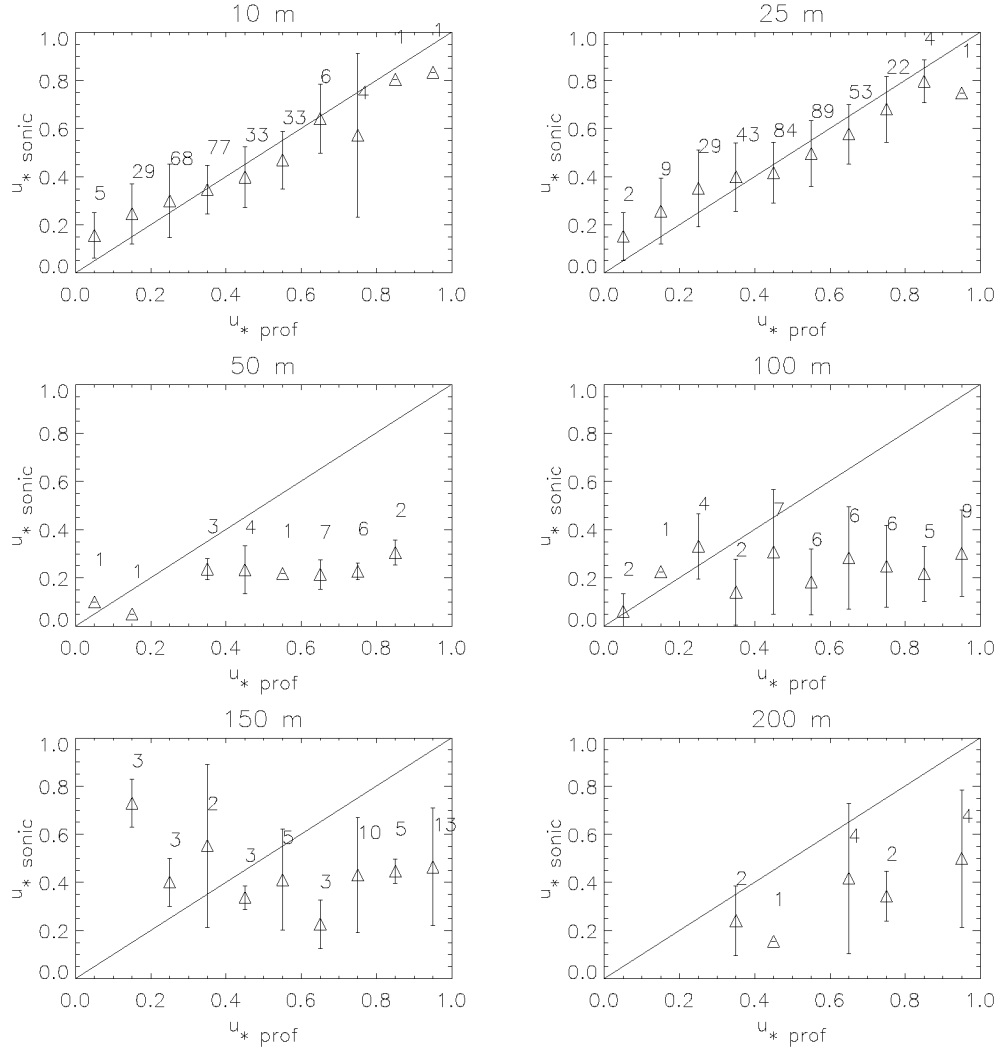
Figure 2.21: The friction velocity determined from the sonics (u_{*sonic}) versus the friction velocity determined from the equations of Högström (1996) (u_{*prof}) for May 1997 for each level based on 30 minute means. The bars show the standard deviation in the measurements. The numbers in the plots represents the number of values used in each "bin".
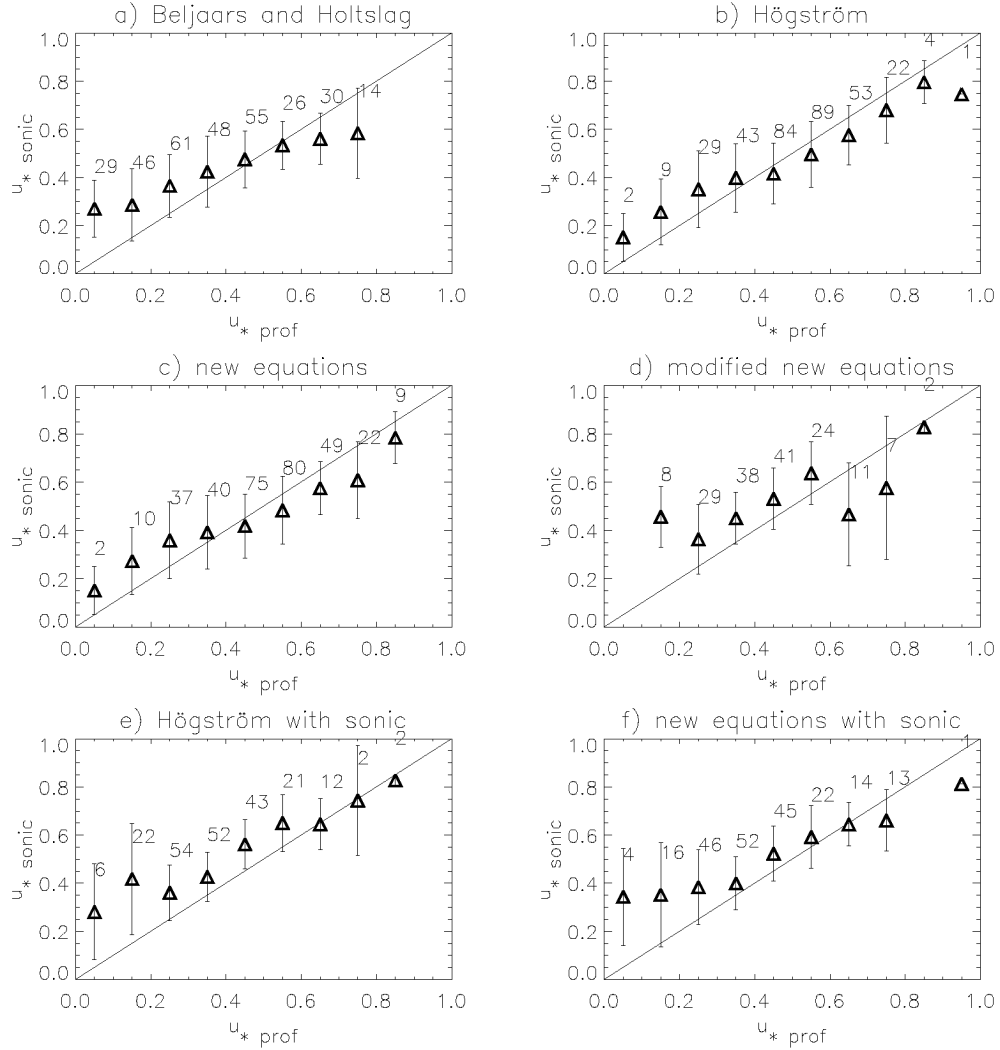
Figure 2.22: Sonic friction velocity (u_{*sonic}) versus the friction velocity determined by the different profile methods (u_{*prof}) at MRI for the 25 m for May 1997 based on 30 minute means. (a) Using Beljaars and Holtslag (1991), (b) using Högström (1996), (c) new equations, (d) modified new equations, (e) using the sonic fluxes in Högström (1996), and (f) using the sonic fluxes in the new equations. The bars show the standard deviation in the measurements. The numbers in the plots represents the number of values used in each "bin". All methods are discussed in the text.

example, using the analytical procedure with the universal functions from Högström (1996) clearly overestimates θ_{*prof} since ϕ_h is lower than seen in the observations (Figure 2.23b). A much better agreement is found when using the analytical procedure with the new equations (Figure 2.23c) or using sonic input into the new equations (Figure 2.23f). The implementation of the iterative procedure with the functions of Beljaars and Holtslag (1991) (Figure 2.23a) also agrees well with θ_{*sonic} although there is comparatively large scatter, particularly for small values of θ_*. Hence, it appears that the derivation of new equations for ϕ_h is justified.
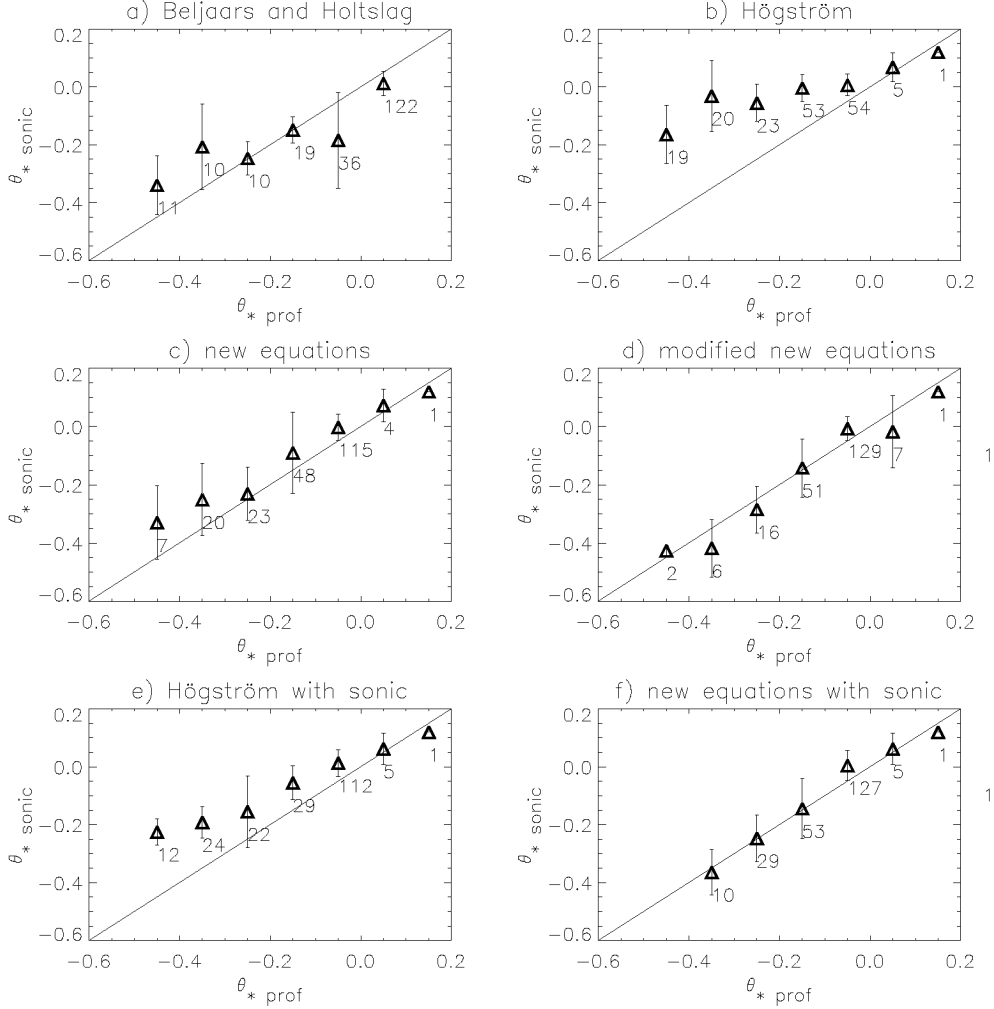
Figure 2.23: Sonic temperature scale (θ_{*sonic}) versus the temperature scale determined by the different profile methods (θ_{*prof}) at MRI for the 25 m for May 1997 based on 30 minute means. (a) Using Beljaars and Holtslag (1991), (b) using Högström (1996), (c) new equations, (d) modified new equations, (e) using the sonic fluxes in Högström (1996), and (f) using the sonic fluxes in the new equations. The bars show the standard deviation in the measurements. The numbers in the plots represents the number of values used in each "bin". All methods are discussed in the text.

40

Turbulent Fluxes

Following the determination of the scaling parameters in the above section, it is then possible to compare the turbulent fluxes as determined from the sonics and the different profile methods.

Figure 2.24 shows the sonic momentum flux (M_{sonic}) compared to the momentum flux determined from the different profile methods (M_{prof}) for the 25 m level in May 1997. Data are binned. Similarly to u_* in Figure 2.22, all profile methods agree well with the sonic.
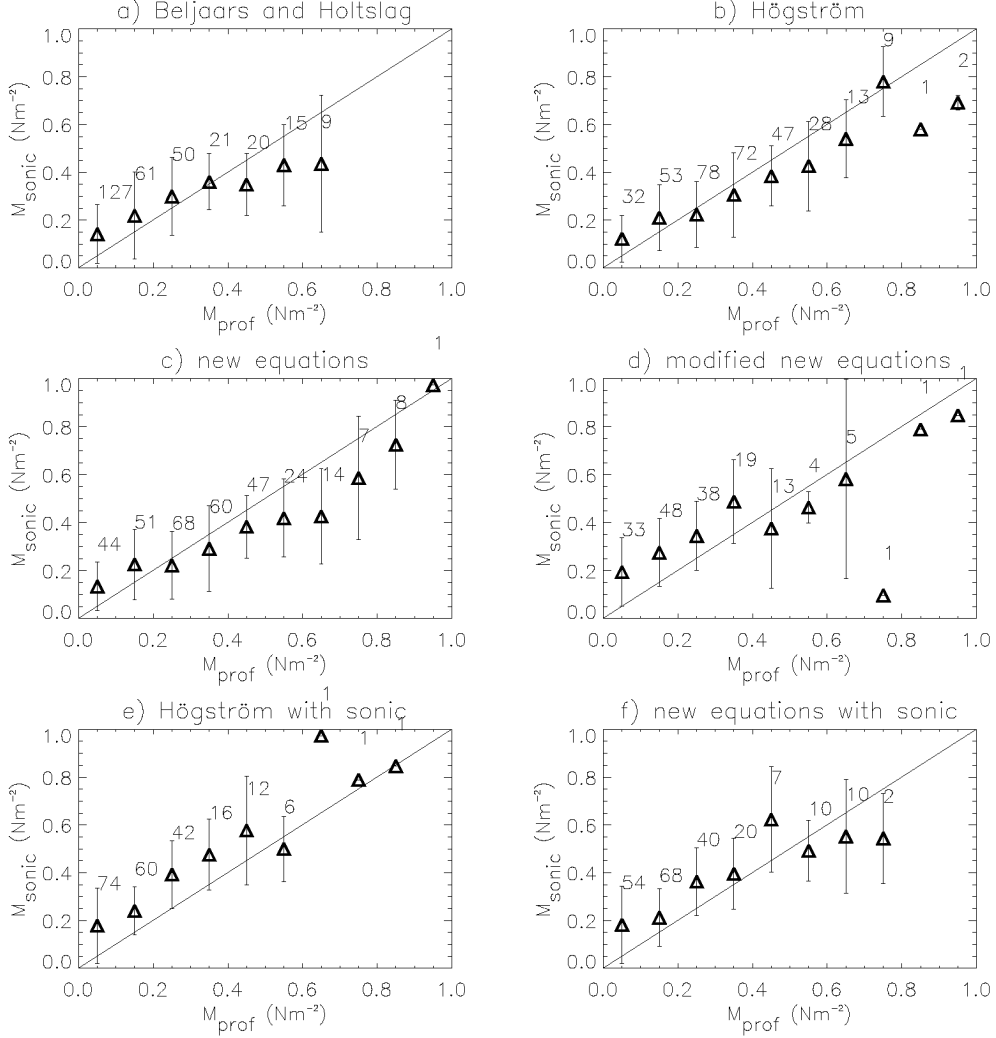
Figure 2.24: Sonic momentum flux (M_{sonic}) versus the momentum flux determined by the different profile methods (M_{prof}) at MRI for the 25 m for May 1997 based on 30 minute means. (a) Using Beljaars and Holtslag (1991), (b) using Högström (1996), (c) new equations, (d) modified new equations, (e) using the sonic fluxes in Högström (1996), and (f) using the sonic fluxes in the new equations. The bars show the standard deviation in the measurements. The numbers in the plots represents the number of values used in each "bin". All methods are discussed in the text.

Figure 2.25 shows the sensible heat flux derived from the sonics ($H_{s\,sonic}$) com-

pared to that from the profile methods (H_{sprof}) for the 25 m level in May 1997. Data are grouped in bins. Similarly to the temperature scale shown in Figure 2.23, the sensible heat flux appears to have the best agreement when using the analytical procedure with the universal functions from the new equations (Figure 2.25c) or when using the iterative procedure with the functions of Beljaars and Holtslag (1991) (Figure 2.25a). Again, using the analytical procedure with the universal functions from Högström (1996) clearly overestimates the sensible heat flux (Figure 2.25b). Surprisingly, using the modified new equations (Figure 2.25d) whereby Ri is derived from R_f shows a large scatter. This is mainly due to the difficulty in removing cases of non-stationarity from the sonic measurements (and hence R_f). Figure 2.26 shows the differences in the stability at the 25 m level for May 1997. In this figure, only 4 plots are shown since the modified new equations uses R_f from the sonics and the use of sonic fluxes in the new equations uses z/L from the sonic.

As can be seen in Figure 2.26, small (absolute) values of stability show good agreement between the sonics and the profile method. However, at larger stabilities, particularly for unstable conditions, the profile method shows somewhat larger values than the sonic. For the new equations, a possible reason for this is due to the levels used to determine the temperature gradient (cf. Figure 2.11), which is consequently used to determine Ri and, therefore, z/L. However, even with obvious differences between sonic stability and the stability derived using the new equations, the resulting sensible heat flux continues to show excellent agreement.

In summary, Table 2.4 shows both the momentum flux and sensible heat flux as determined by the eddy correlation method for the 25 m level for each month of 1997.

Table 2.4: The average monthly momentum and sensible heat flux for the 25 m level for 1997. Units: M in N m^{-2} and H_s in W m^{-2}.

	Jan	Feb	Mar	Apr	May	Jun	Jul	Aug	Sep	Oct	Nov	Dec
M	-	0.88	0.33	0.25	0.35	0.33	0.41	0.38	0.45	0.31	0.19	0.32
H_s	-	3.4	-17.4	-32.5	-39.8	-31.1	-46.7	-38.4	-18.4	-	-19.5	-20.3

Figure 2.27 shows the universal function for momentum as determined from the sonic ($\phi_{m\,sonic}$) compared to that from the profile method ($\phi_{m\,prof}$) for the 25 m level in May 1997. In this figure, the majority of values range from 0.5 to 1 for both the eddy correlation method and the profile method. For values of ϕ_m smaller than 2, there is good agreement between the methods. For larger values, the profile method tends to overestimate ϕ_m although non-stationarity makes the situation unclear since it is possible that some of the sonic values are inaccurate. This is further emphasised for ϕ_h (Figure 2.28). This figure shows that, for large values of ϕ_h, non-stationarity plays an important role. For small values of ϕ_h (< 0.5), it also appears that the iterative method using the functions of Beljaars and Holtslag (1991) shows significant differences to the sonic measurements. However, this could also be due to non-stationarity.
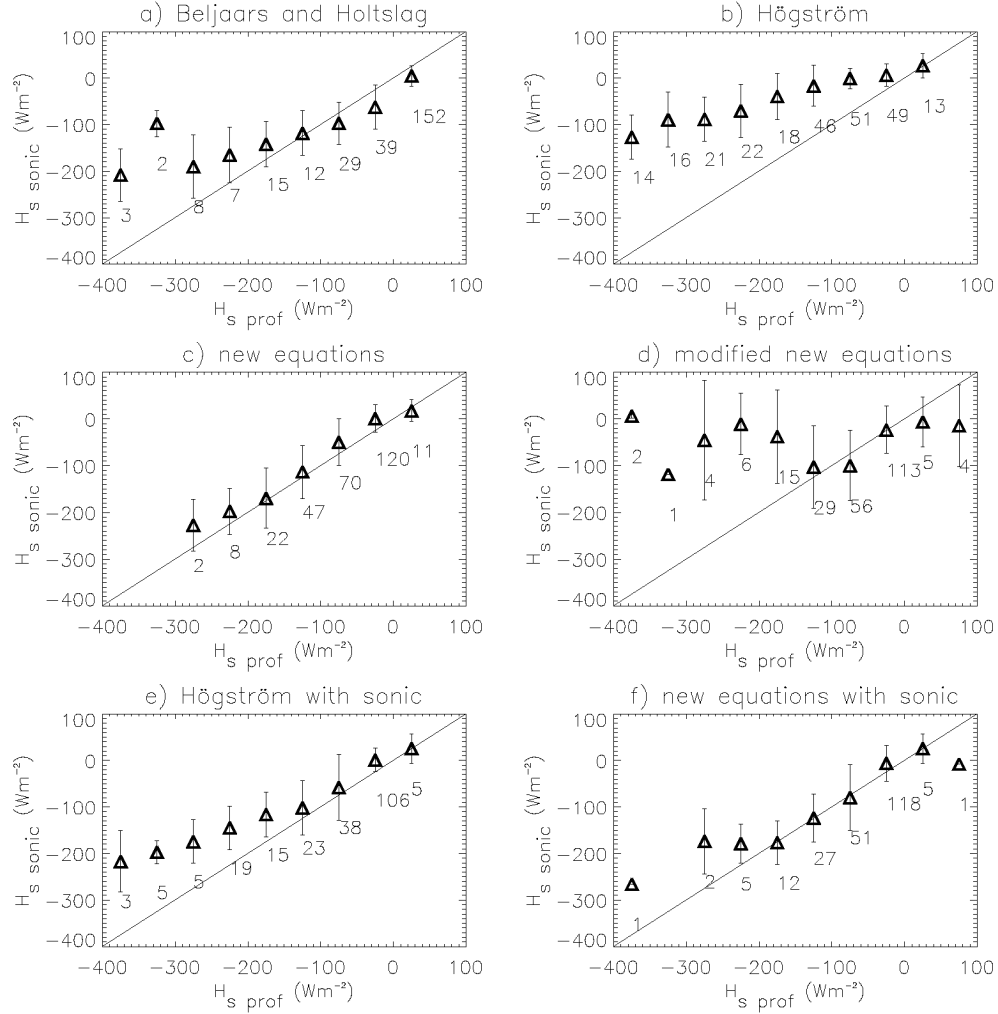
Figure 2.25: Sonic sensible heat flux ($H_{s\,sonic}$) versus the sensible heat flux determined by the different profile methods ($H_{s\,prof}$) at MRI for the 25 m for May 1997 based on 30 minute means. (a) Using Beljaars and Holtslag (1991), (b) using Högström (1996), (c) new equations, (d) modified new equations, (e) using the sonic fluxes in Högström (1996), and (f) using the sonic fluxes in the new equations. The bars show the standard deviation in the measurements. The numbers in the plots represents the number of values used in each "bin". All methods are discussed in the text.

43
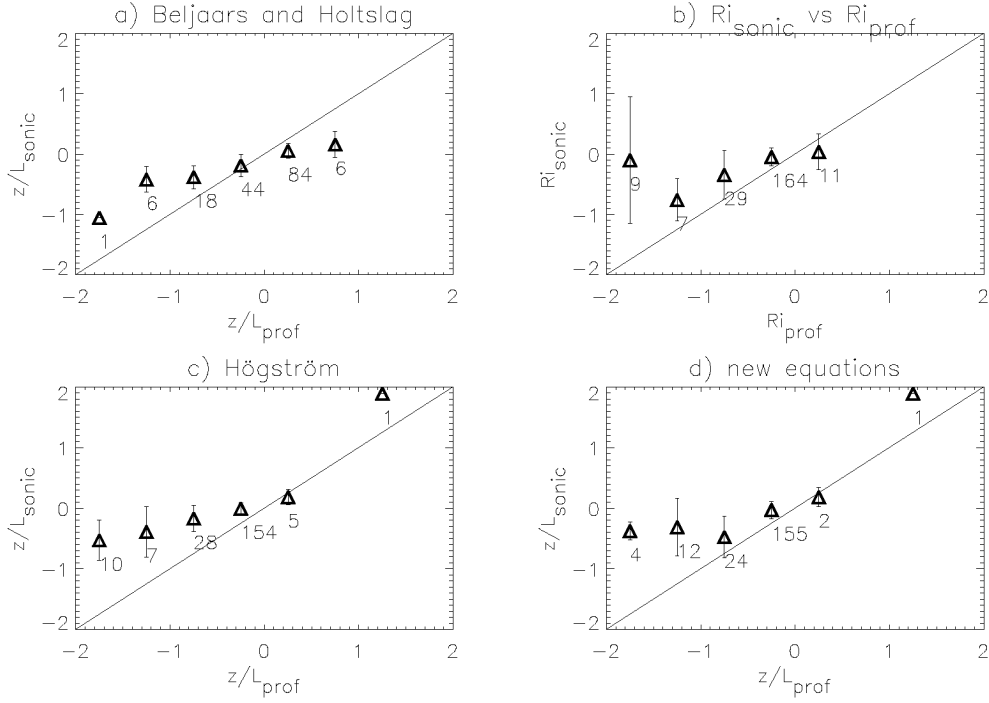
Figure 2.26: Stability for the sonic compared to the profile method at MRI for the 25 m for May 1997. (a) z/L_{sonic} versus z/L_{prof} where the Monin-Obukhov functions are derived from Beljaars and Holtslag (1991), (b) Ri from the sonic versus Ri from the profile method, (c) z/L_{sonic} versus z/L_{prof} where the Monin-Obukhov functions are derived from Högström (1996), and (d) z/L_{sonic} versus z/L_{prof} where the Monin-Obukhov functions are derived from the new equations. The bars show the standard deviation in the measurements. The numbers in the plots represents the number of values used in each "bin". Measurements are 30 minute mean values.
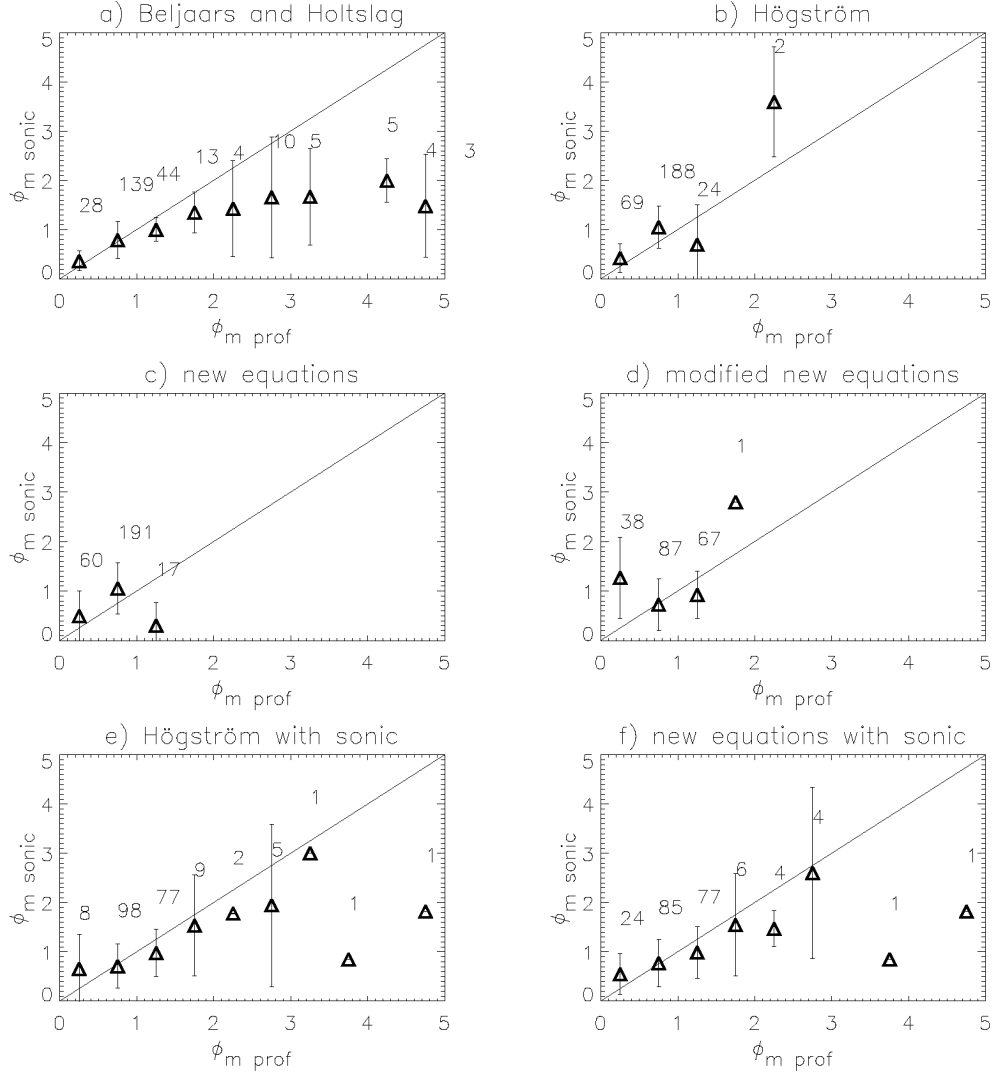
Figure 2.27: Sonic universal function for momentum ($\phi_{m\,sonic}$) versus the universal function for momentum determined by the different profile methods (ϕ_{mprof}) at MRI for the 25 m for May 1997 based on 30 minute means. (a) Using Beljaars and Holtslag (1991), (b) using Högström (1996), (c) new equations, (d) modified new equations, (e) using the sonic fluxes in Högström (1996), and (f) using the sonic fluxes in the new equations. The bars show the standard deviation in the measurements. The numbers in the plots represents the number of values used in each "bin". All methods are discussed in the text.
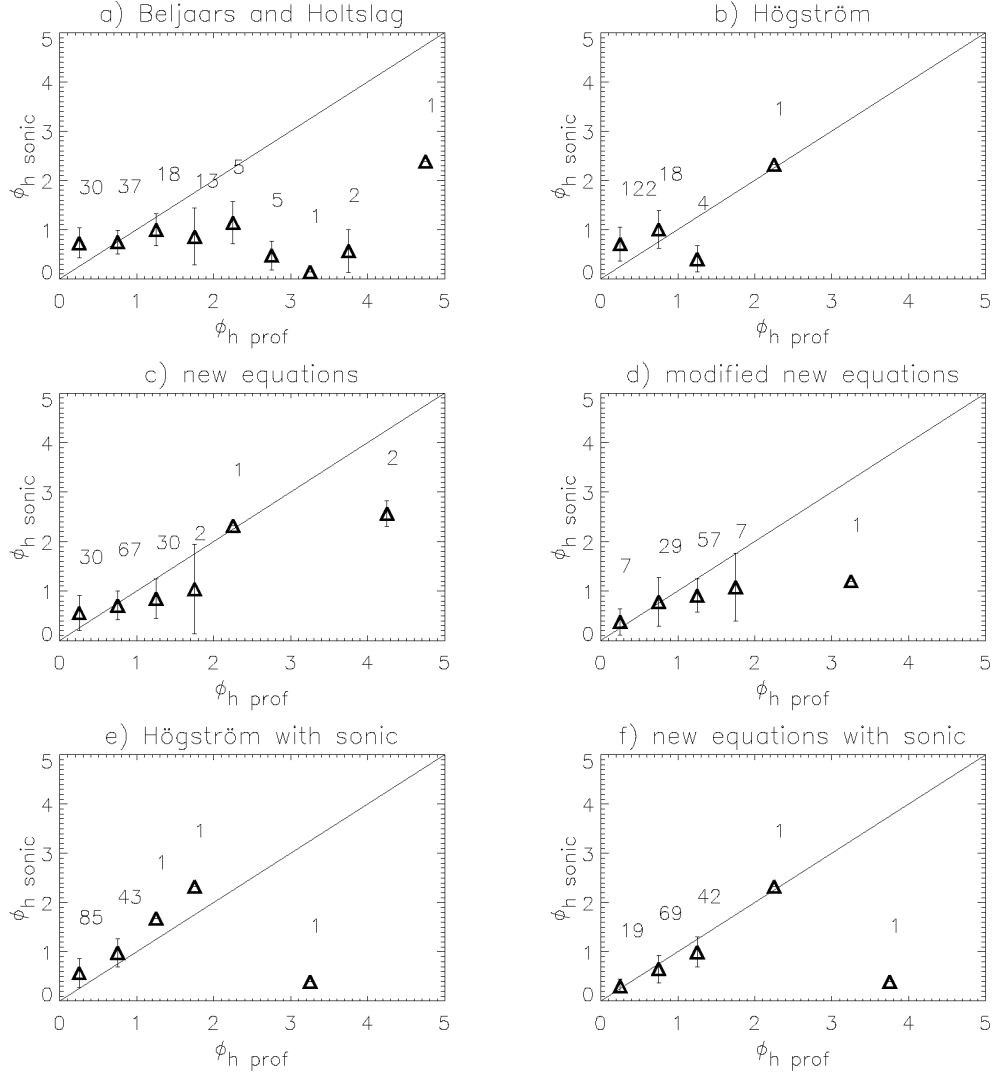
Figure 2.28: Sonic universal function for heat ($\phi_{h\,sonic}$) versus the universal function for heat determined by the different profile methods ($\phi_{h\,prof}$) at MRI for the 25 m for May 1997 based on 30 minute means. (a) Using Beljaars and Holtslag (1991), (b) using Högström (1996), (c) new equations, (d) modified new equations, (e) using the sonic fluxes in Högström (1996), and (f) using the sonic fluxes in the new equations. The bars show the standard deviation in the measurements. The numbers in the plots represents the number of values used in each "bin". All methods are discussed in the text.

46
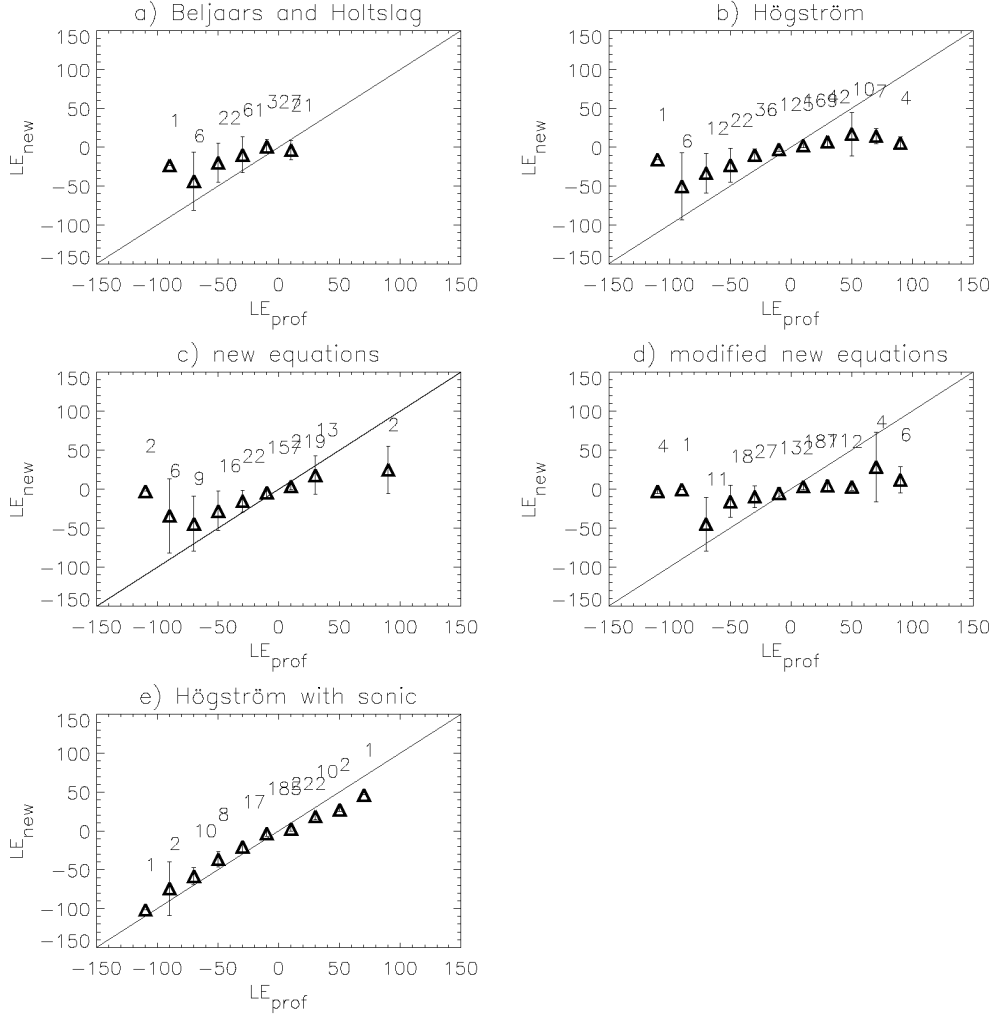
Figure 2.29: Latent heat flux determined from the new equations (LE_{new}) versus the latent heat flux determined by the other profile methods (LE_{prof}) at MRI for the 25 m for May 1997 based on 30 minute means. (a) Using Beljaars and Holtslag (1991), (b) using Högström (1996), (c) modified new equations, (d) using the sonic fluxes in Högström (1996), and (e) using the sonic fluxes in the new equations. The bars show the standard deviation in the measurements. The numbers in the plots represents the number of values used in each "bin". All methods are discussed in the text.

For latent heat flux, sonic measurements are not available. Figure 2.29 shows only five comparisons rather than six. In this figure, LE_{new} represents the latent heat flux determined using the profile method where the universal functions are determined from using sonic fluxes in the new equations. It is obvious that the best agreement is with the new equations (Figure 2.29c) and using sonic input into the equations of Högström (1996) (Figure 2.29e). However, it is obvious that these figures are not completely independent, making an accurate comparison difficult.

Determination of the Roughness Length for Momentum

There are a number of methods to determine the roughness length of momentum of a site. Of these, the log wind profile is probably the simplist approach. In this section, the log wind profile will be discussed as well as two independent methods used to gain confidence in the results: The methods of Martano (2000) and Brutsaert (1982).

The simplest approach to determine the roughness length of momentum, z_0, is by using the log wind profile (Equation 2.43).

$$\frac{u(z)}{u_*} = \frac{1}{k}\left[\ln\frac{z}{z_0} - \psi_m\left(\frac{z}{L}\right)\right],\qquad(2.43)$$

where the symbols have been described previously.

The three methods discussed by Martano (2000) determine the zero plane displacement height and roughness length of momentum using a single level sonic anemometer. He found that the three methods produce similar results, so only one method will be discussed here.

According to Martano (2000), the windspeed profile can be written according to Equation 2.44.

$$S = \frac{k\,u}{u_*} + \psi\left[\frac{z-d}{L}\right],\qquad(2.44)$$

where S is a statistical quantity and $\psi\left[\frac{z-d}{L}\right]$ is defined from Beljaars and Holtslag (1991) as discussed previously. Here, $\psi\left[\frac{z-d}{L}\right]$ is calculated by changing d step by step from slightly negative values to a maximum value of $d = z$.

From this, the standard deviation σ_s can be determined using Equation 2.45.

$$\sigma_s{}^2 = (S- <S>)^2,\qquad(2.45)$$

where $<\ldots> \equiv \frac{1}{N}\sum_i^N$ denotes the average over the dataset of N groups of time averaged quantities u_i, T_i, u_{*i} and L_i at the same height z.

The roughness length (Equation 2.47) is then calculated from the standard deviation of the roughess length (Equation 2.46) and the standard deviation of S as shown in Equation 2.45.

48

$$\sigma_{z_0} = (z - d) \exp < -S > \sigma_s, \tag{2.46}$$

$$z_{0e} \approx \frac{\sigma_{z_0}}{\sigma_s}. \tag{2.47}$$

The final value of d, and therefore z_0, is determined when a minimum value for σ_s is found.

The main disadvantage with this method is that it is only applicable within the constant flux layer and cannot be used either within the canopy layer, or at higher levels.

The main difference between the method used by Brutsaert (1982) and the method described above is that Brutsaert (1982) derives the roughness length as a function of the boundary layer height as opposed to the measurement height. The main advantage with the method by Brutsaert (1982) is that it can be used within the canopy layer, or above the constant flux layer, as long as measurements do not cross into other layers. Here, the method of Brutsaert (1982) follows the method of Martano (2000) in determining z_0 from σ_s and σ_{z_0}. However, the calculation of S varies from above and, instead, follows Equation 2.48.

$$S = \frac{k \, u}{u_*} - B_i, \tag{2.48}$$

where B_i is a similarity function defined in the same manner as Beljaars and Holtslag (1991) but replacing the measurement height with the boundary layer height. The boundary layer height, δ_i , is determined using the following.

$$\delta_i = \begin{cases} \frac{0.25 \, u_*}{f} & \text{for } \left| \frac{u_*}{fL} \right| < 4 \\ k \sqrt{\frac{u_* L}{f}} & \text{for stable conditions,} \end{cases} \tag{2.49}$$

where $f = 2\omega \sin \phi$ is the Coriolis parameter (s^{-1}), ω is the angular speed of rotation of the earth (rad s^{-1}) and ϕ is the latitude (^{o}). For Tsukuba, Japan, $f = 8.543 \times 10^{-5} \, s^{-1}$.

For unstable conditions, the boundary layer height was determined subjectively when the potential temperature θ is at a maximum.

Figure 2.30 shows the roughness length of momentum for each 45° wind direction sector for May 1997 using the log wind profile discussed above with the sonic data. The lack of data at the 10 m and 200 m levels is simply due to the limitation of measurements. For instance, although the friction velocity may be present at a given time, the temperature scale could be missing resulting in no determination of the roughness length. As can be seen in the figure, the roughness length is very large at MRI, averaging approximately 30 cm at the 25 m level, 50 cm at the 50 m and 100 m levels and varying quite dramatically at higher levels. It is apparent that the north east is generally characterised by lower roughness lengths which is attributable to lower roughness elements than in other wind directions. Although the MRI building is located in the north east, this sector is dominated by forest areas, whereas the other wind directions are strongly influenced by buildings.

49
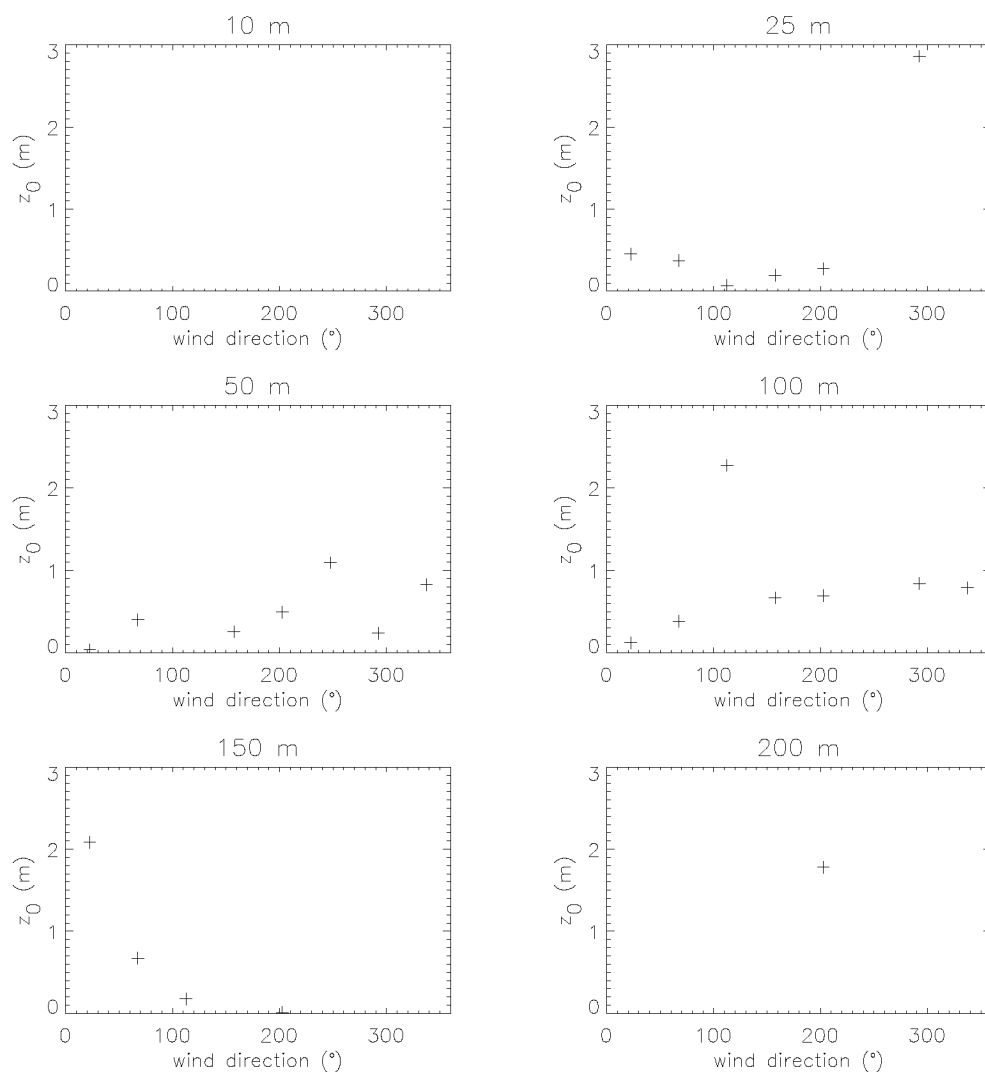
Figure 2.30: Roughness length (z_0) for momentum as determined from the log wind profile versus wind direction for May 1997. North is represented by 0°.

The roughness length determined by Figure 2.30 can be validated by comparing it to the windspeed. In theory, changing windspeed should not alter the roughness length. This is shown in Figure 2.31 for the north east to east sector. The other wind directions show comparable results. As can be seen in the figure, even though there is significant scatter of z_0, there is no trend of the roughness length changing with windspeed. This figure also shows that the 25 m level has the most quantative and qualitative data due to the number of available measurements and the reduced scatter of z_0 compared to other levels.
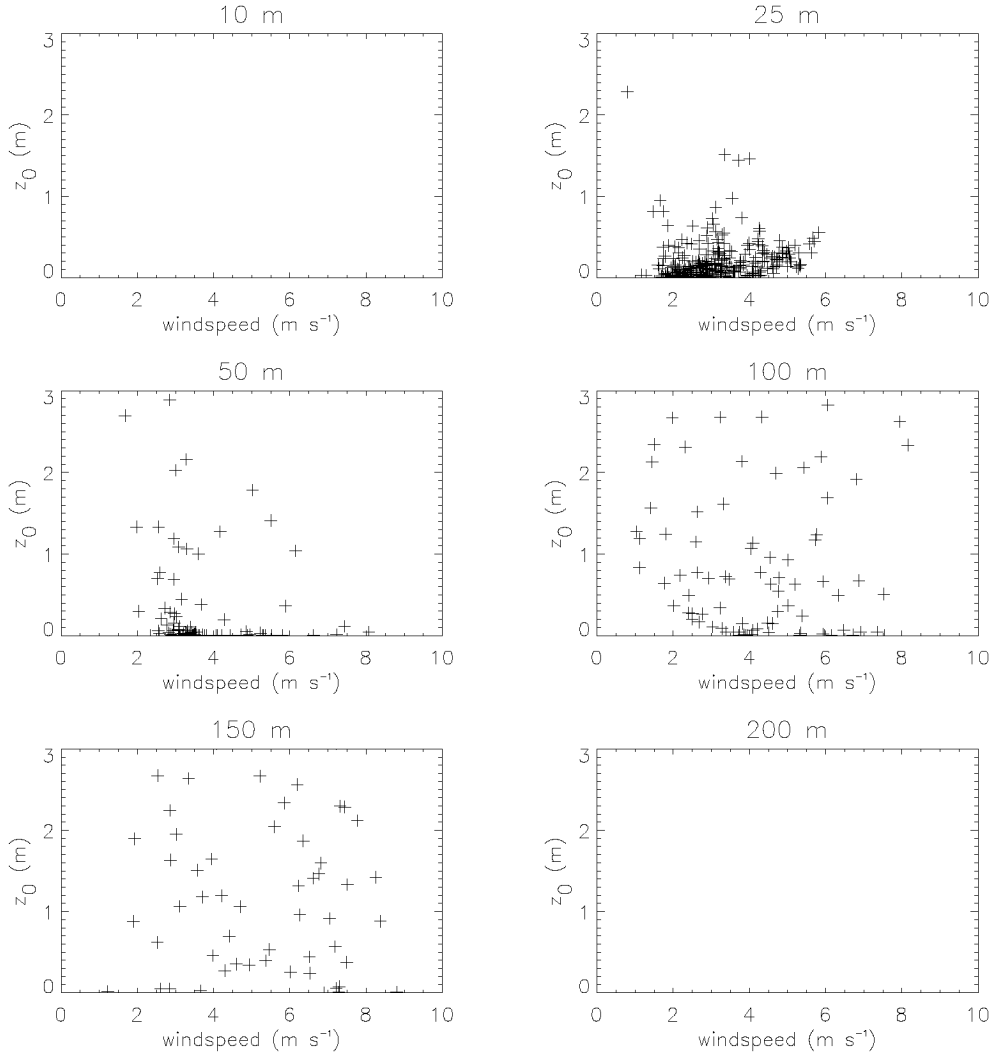
Figure 2.31: Roughness length (z_0) for momentum as determined from the log wind profile versus 30 minute mean windspeed for the NE-E wind sector for May 1997.

While the log wind profile is the easiest and probably most direct means to determine the roughness length, it is also possible to compute this value using other methods (discussed above). Figure 2.32 shows the results from Martano (2000) for each wind direction (45° segments). Typically, the roughness length ranges from 20 cm to over 2 m.
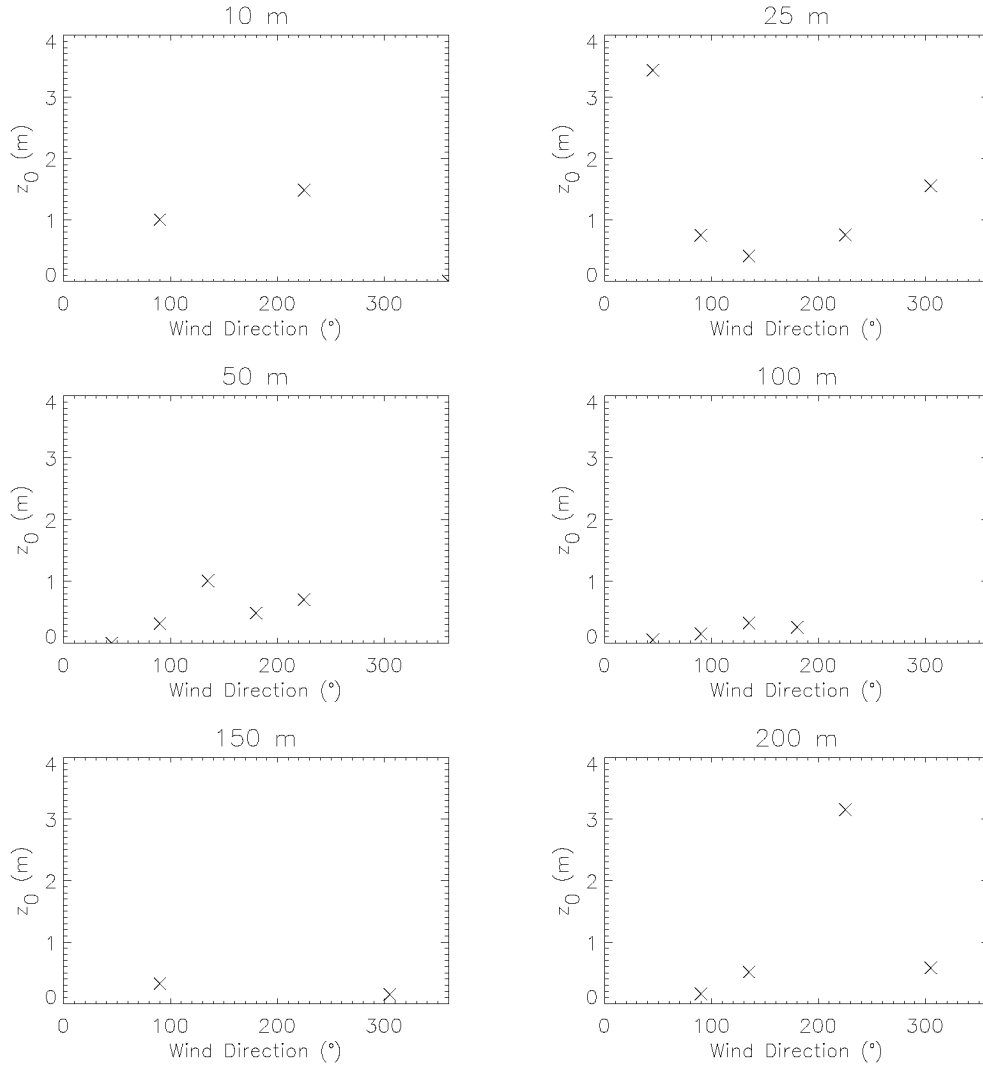
Figure 2.32: Roughness length (z_0) for each level at each wind direction sector (45° sectors) determined by the method in Martano (2000). North is represented by 0°. Units in m.

To determine the validity of the roughness length values determined from Martano (2000), the roughness length are compared with windspeed for each wind direction (Figures 2.33 and 2.34). Only two wind directions are shown below, as other directions do not have a significant number of measurements to analyse in more depth.
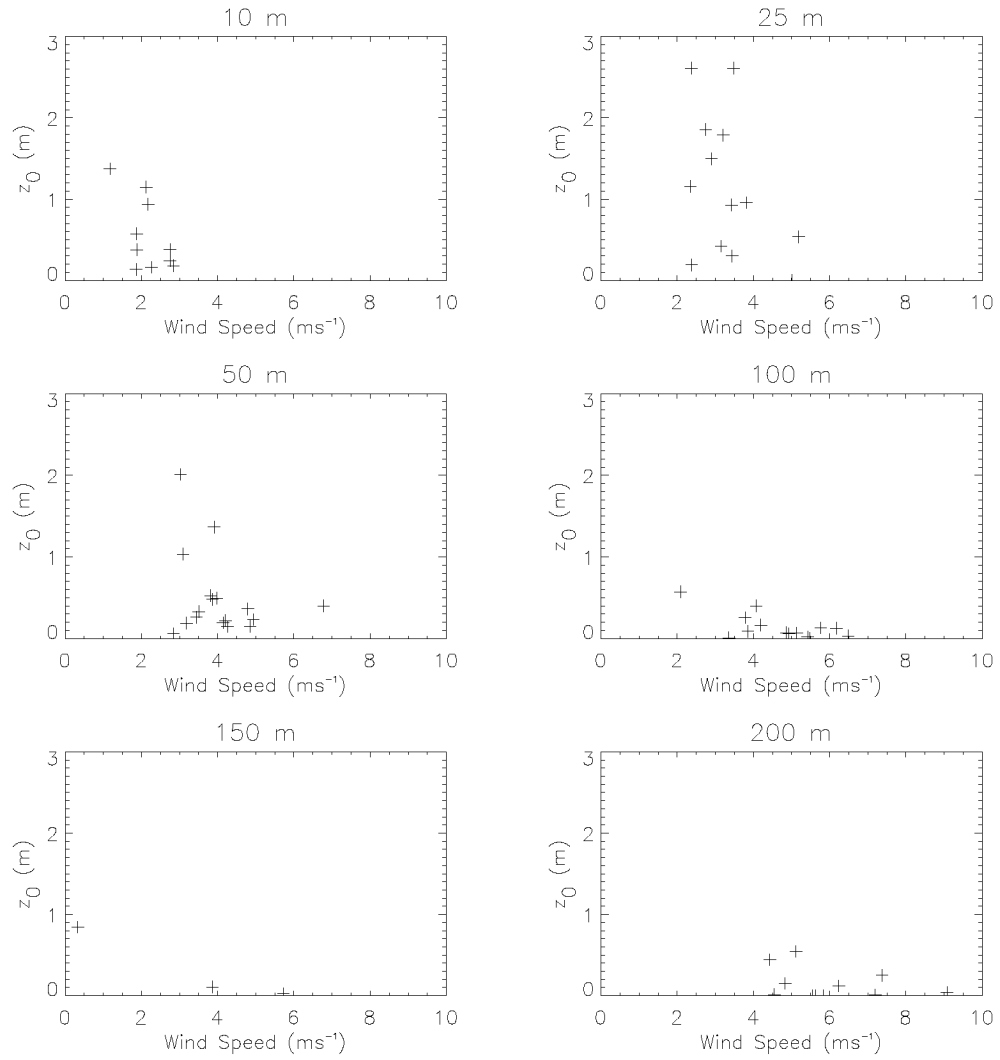
Figure 2.33: Roughness length versus 30 minute mean windspeed for May 1997 for all 6 levels at MRI for the NE-E sector.
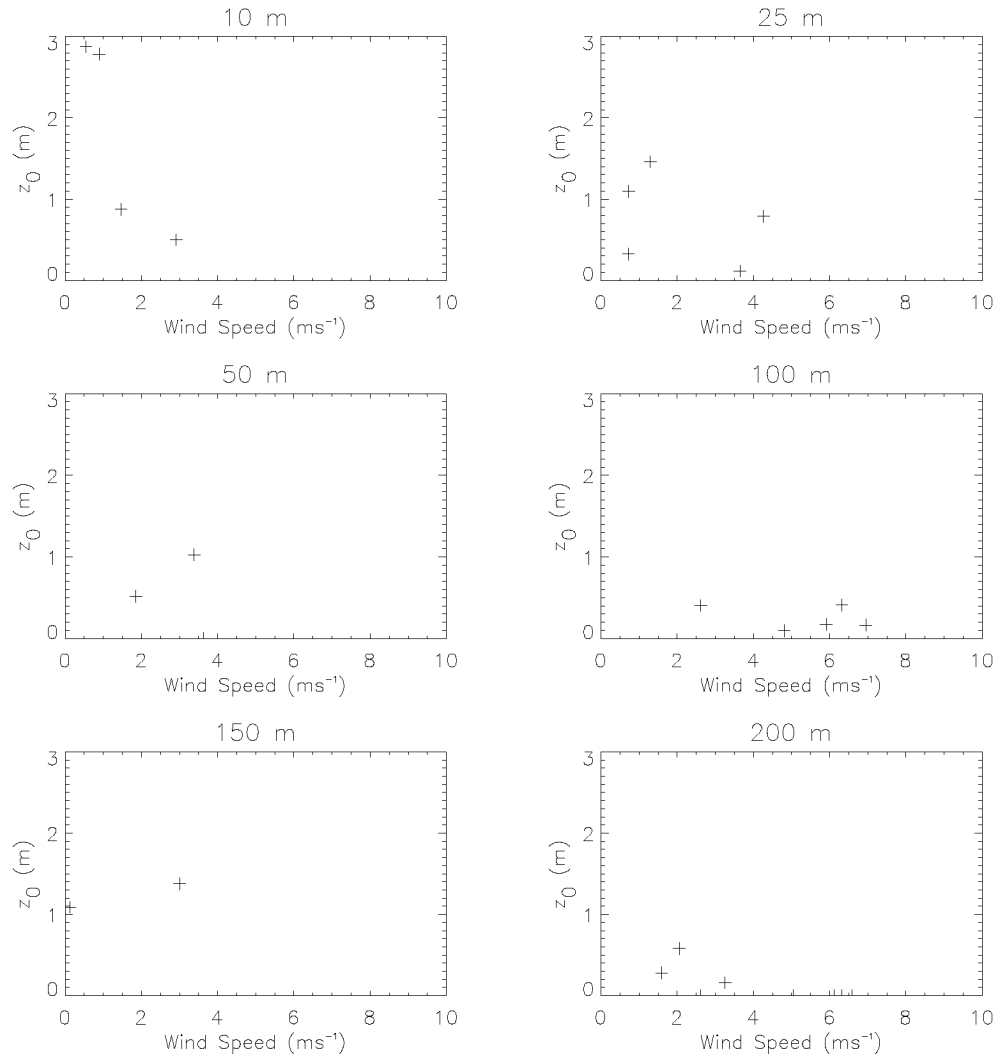
Figure 2.34: Roughness length versus 30 minute mean windspeed for May 1997 for all 6 levels at MRI for the S-SW sector.

As can be seen in Figures 2.33 and 2.34, there is a large scatter in the lowest levels. In particular, the 10 m and 25 m levels show large variations of roughness length with windspeed implying that the equations from Martano (2000) define these levels as being located below the constant flux layer. This is contradictory to the log wind profile method above, which shows that that 25 m level is within the constant flux layer. Moving up the tower, it is evident that the roughness length becomes more constant, showing that the highest three levels are most likely within the constant flux layer. The 50 m level appears to be partially, but not always, within the constant flux layer. From this, it can be concluded that the highest three levels give reasonable values for the roughness length for the NE-E and S-SW sectors, which correspond to values in roughness length at 90° and 225° in Figure 2.32, respectively. Hence, for this example, the roughness length for both the NE-E and S-SW sectors is roughly 25 cm and 80 cm, respectively. For the lower three levels, the method of Martano (2000) appears to be inaccurate and the resulting roughness lengths should be viewed with caution.

The method of Brutsaert (1982) can be analysed in a similar manner to that discussed above. Figure 2.35 shows the roughness length for each wind direction for the six levels at MRI for May 1997. As with the method from Martano (2000), the values of the roughness length range from roughly 20 cm to 2 m. To determine which of these values are accurate, it is possible to compare the roughness length to the windspeed (Figure 2.36). As mentioned previously, the roughness length should not vary with windspeed for a given wind direction. Unfortunately, there appears to be large amounts of missing data using the method of Brutsaert (1982) making a full analysis difficult. However, it appears that the roughness length does not vary with windspeed for the 50 m and 100 m levels regardless of wind direction. For the NE-E and W-NW sectors, the roughness length appears quite low for the site (approximately 30 cm). However, in the N-NE sector, the roughness length is somewhat larger at approximately 2 m. This could be explained by the vicinity of buildings to the north and north east of the tower. Looking at each sector independently, the roughness length for the 50 m and 100 m levels in the NE-E sector appears to be constant when compared to windspeed (Figure 2.36). Once again, the roughness length is very low for the site (approximately 30 cm). For the W-NW sector, the roughness length does not vary significantly with windspeed for the 50 m and 100 m levels (not shown). In this sector, the roughness length ranges from 20 cm to almost 1 m. The increase in roughness length can be explained by the inhomogeneity of the W-NW sector. The area close to the tower is covered with grass, followed by small trees, while there are buildings further from the site.

In conclusion, the log wind profile shows a wide range of values for the roughness length, ranging from 10 cm to almost 3 m. Considering the inhomogeneity of the site, these results are feasible. This is further emphasised by the fact that the windspeed does not change the roughness length. The method by Martano (2000) is able to deal with the inhomogeneity of the site reasonably well, although it is still only applicable within the constant flux layer. Regardless of wind direction, the method of Martano (2000) shows a roughness length of approximately 25 cm. There is some scepticism regarding this, however, since the roughness elements are quite different depending on wind direction. Brutsaert (1982), on the other hand, appears to show
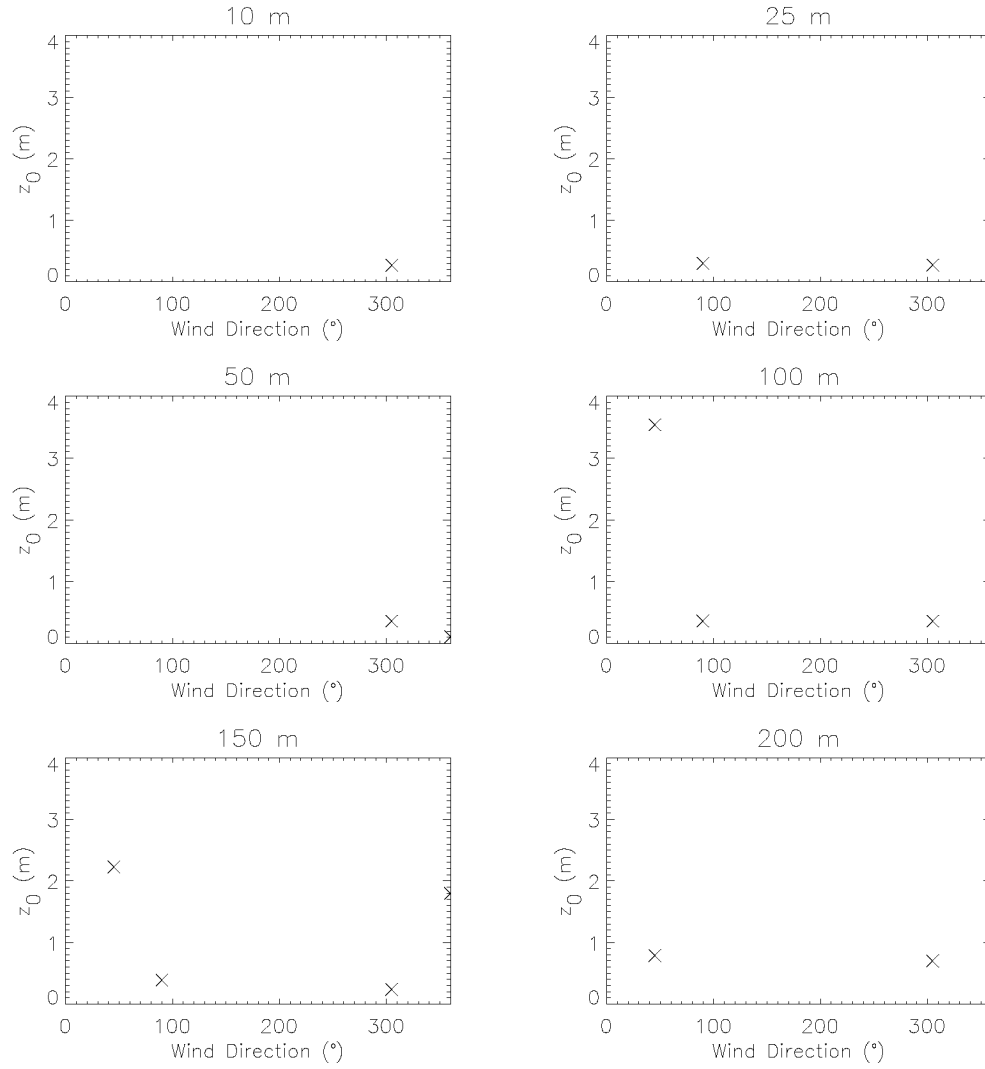
Figure 2.35: Roughness length (z_0) for each level at each wind direction sector (45° sectors) determined by the method in Brutsaert (1982). North is represented by 0°. Units in m.
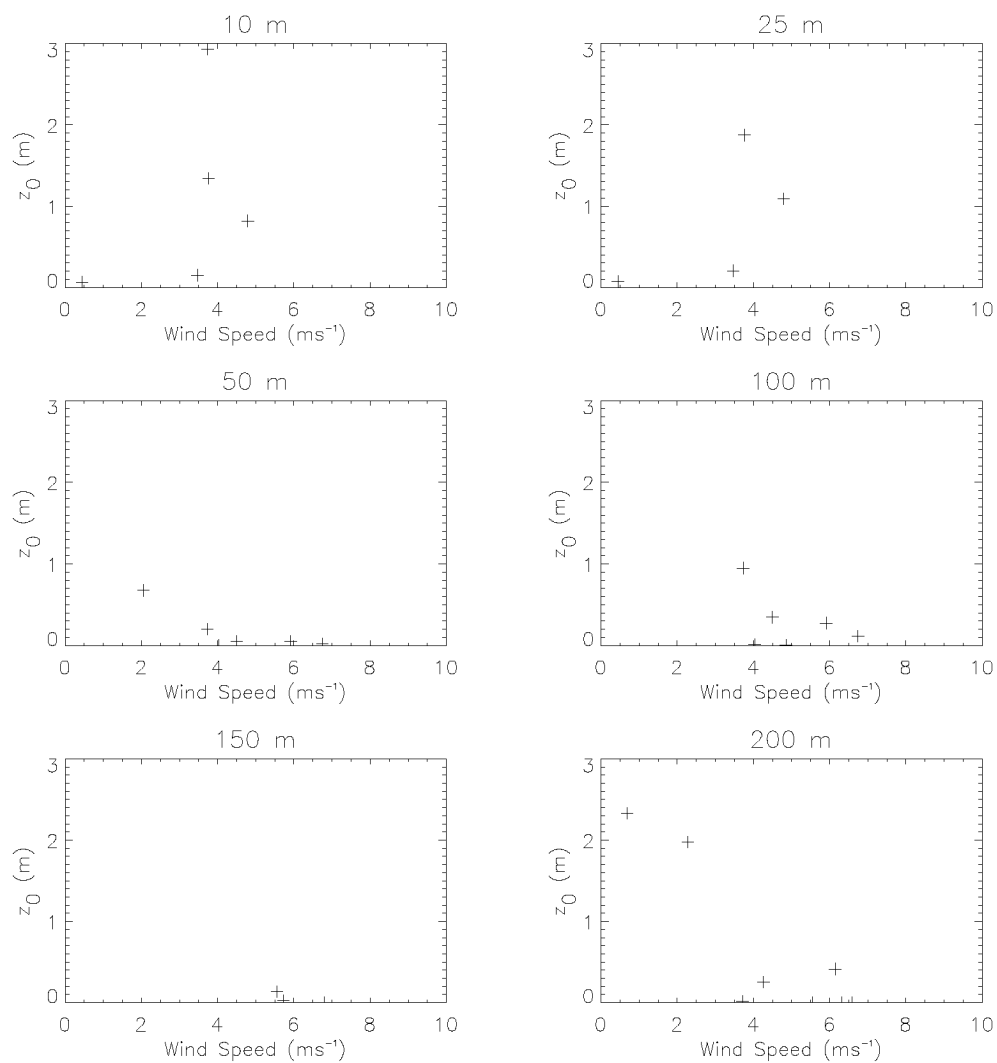
Figure 2.36: Roughness length versus 30 minute mean windspeed for May 1997 for all 6 levels at MRI for the NE-E sector.

more accurate variations of roughness length with the inhomogeneity of the site. For example, in the W-NW sector, the roughness length varies from roughly 20 cm to 2 m. These values are realistic since the area close to the tower is covered with grass and small trees, while the area further from the tower is dominated with buildings. The main problem with the method from Brutsaert (1982) for May 1997 at MRI, however, is that there are only a small number of measurements that are statistically significant.

For the remainder of this research, the roughness length from the log wind profile was adopted. The main reasons for this are due to the large amount of data at the 25 m level, the high level of quality as seen in Figure 2.31 and the ease of this method.

Determination of the Roughness Length for Heat

In atmospheric models, it is often assumed that the roughness length for heat equals the roughness length for momentum ($z_{0h} = z_0$). This means that no distinction is made between the surface temperature at the height of z_0 and the surface radiation temperature. However, this is not necessarily true. For example, Beljaars and Holtslag (1991) show that these temperatures can differ by 6 K at Cabauw, The Netherlands. Therefore, the roughness length for heat will be discussed separately from z_0.

To determine z_{0h}, a quantity θ_0 is first defined by Equation 2.50.

$$\frac{\theta - \theta_0}{\theta_*} = \frac{1}{k} \left[\ln \frac{z}{z_0} - \psi_h \left(\frac{z}{L} \right) \right], \tag{2.50}$$

where all symbols are previously defined and ψ_h follows Beljaars and Holtslag (1991). The quantity θ_0 is the temperature at the height of the roughness length of momentum. From this, the roughness length of heat can be determined using Equation 2.51.

$$\frac{\theta_0 - \theta_s}{\theta_*} = \frac{1}{k} \ln \frac{z_0}{z_{0h}} = B^{-1}, \tag{2.51}$$

where θ_s is the surface temperature (K).

The difficulty in determining that roughness length of heat is that it is a very difficult quantity to define. Whereas the roughness length of momentum is easy to visualise (where the windspeed tends to 0), it is difficult to quantify the absolute meaning of the surface temperature.

Figure 2.37 shows the ratio of u/u_* versus z/L for the 25 m level in May 1997 using the method of determining the roughness length of heat. It is important to note that the roughness length here is an areally averaged value, rather than local value. To determine the roughness length, a visual inspection of the figure was made to find that $u/u_* \approx 4$ at $z/L = 0$. This is then used in the log wind profile to determine the areally averaged roughness length, which is based on windspeed and the friction velocity only. Following this, $\theta_0 - \theta_s$ versus θ_v is plotted (Figure 2.38) to determine

the roughness length of heat. Although there is considerable scatter in Figure 2.38, z_{0h} was estimated to be roughly 5×10^{-4} m based on Equation 2.51. This value is in reasonable agreement with measurements at Cabauw, The Netherlands which find $B^{-1} \approx 22$ (here, $B^{-1} \approx 20$) which gives confidence in the results (Beljaars and Holtslag, 1991).
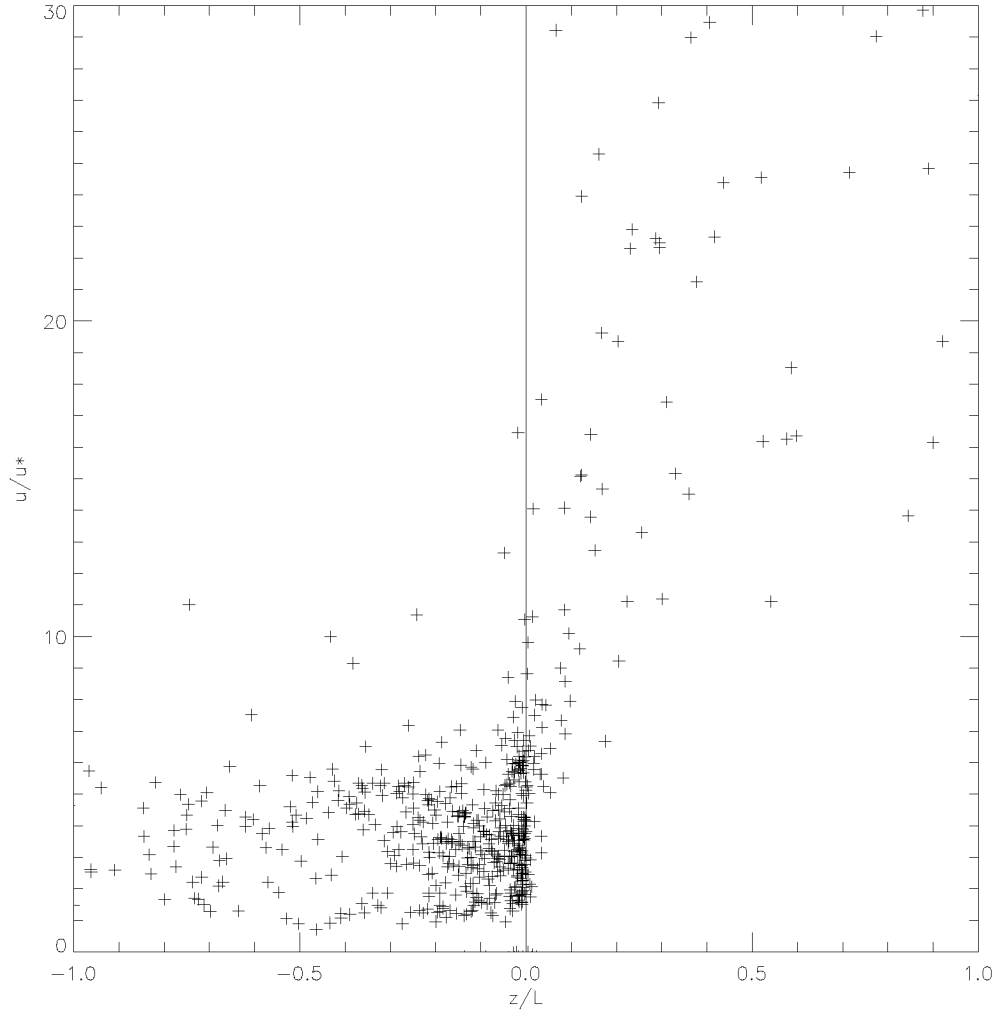
Figure 2.37: The ratio of u/u_* compared to z/L for May 1997 at the 25 m level based on 30 minute mean observations.
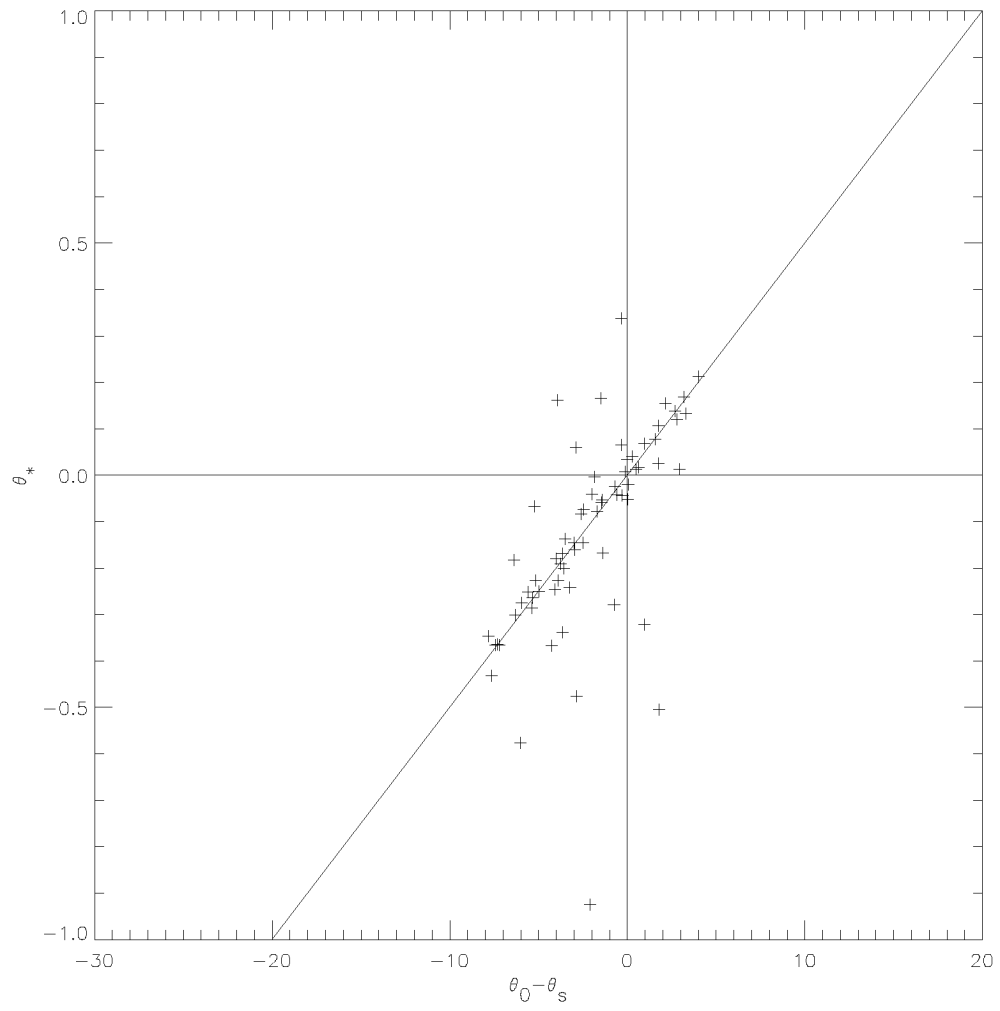
Figure 2.38: θ_* versus $\theta_0 - \theta_s$ for May 1997 at the 25 m level based on 30 minute mean observations.

2.2.6 Summary of Measurements

One method to analyse the accuracy of the turbulent fluxes in GCMs is to compare values to observations. However, while long term measurements of the latent heat flux are reasonably abundant, long term measurements of the sensible heat flux are limited. This study uses measurements from GEBA sites with a minimum of 3 years of measurements for latent heat flux and 12 months of measurements for sensible heat flux, as well as the sensible and latent heat fluxes from Cabauw, The Netherlands (10 years), the latent heat flux from Swampy Summit, New Zealand (6 years) and the turbulent fluxes from MRI, Tsukuba, Japan (2 years).

Two sites have been analysed in more detail here for the validation of their climatologies for use in the validation of GCMs. Only limited measurements are provided for the Swampy Summit, New Zealand site although these measurements are of high quality and provide latent heat flux measurements for 6 years (1991-96). The MRI site has an abundance of measurements of varying quality for two years (1997-98). Only the observations from 1997 have been discussed here, however, due to the increased quality over 1998 measurements.

The 213 m tower at MRI, Tsukuba, Japan is a valuable source of turbulent flux data that can be used in the validation of climate models. Measurements on the tower include sonic windspeed and temperature, as well as windspeed, temperature and humidity from profile instruments. Results show that sonic measurements compare well with the profile instruments. These observations were then used to determine the roughness length of the site, the scaling parameters, and the turbulent fluxes.

The friction velocity and, consequently, the momentum flux show good agreement between the eddy correlation method and the profile method, regardless of the means to determine the universal functions. However, for the temperature scale and sensible heat flux, it is clear that the new equations proposed in this work are superior. For the stability, the profile method and eddy correlation method often disagree, particularly for large instability. This could be due to non-stationarity in the sonic measurements, or due to a slightly inaccurate temperature which leads to inaccuracies in Ri and, consequently, z/L. However, even at large values of instability, the resulting sensible heat flux shows good agreement. For the roughness length, the log wind profile and the method of Brutsaert (1982) give values ranging from approximately 20 cm to 2 m, depending on wind direction. These values seem more realistic than those from Martano (2000) which show a constant value of 25 cm, regardless of wind direction, regardless of the close vicinity of trees and buildings around the tower.

2.3 Model Description

2.3.1 Introduction

The models used in this study are: The ECHAM4 GCM from the Max-Planck Institute for Meteorology (henceforth ECHAM4), Hamburg (Roeckner et al., 1996); the HadAM2b GCM from the Hadley Centre for Climate Prediction and Research (henceforth HadAM2b), Bracknell (Stratton, 1999), and; the ARPEGE GCM from

Météo-France (henceforth ARPEGE), Toulouse (Déqué et al., 1994). Additionally, 3 Reanalysis results were used. They are: The European Centre for Medium-Range Weather Forecasts (ECMWF) Reanalysis (henceforth ERA15), Reading (Gibson et al., 1997); the National Centers for Environmental Prediction/National Center for Atmospheric Research Reanalysis (henceforth NCEP), Washington (Kalnay et al., 1996), and; the NASA/Data Assimilation Office Reanalysis (henceforth GEOS; Schubert et al., 1993).

The Reanalysis systems include fixed versions of operational data assimilation and modelling system to reanalyse historical data. These multiyear simulations have been completed to provide a physically consistent dataset of the atmosphere which is believed to be useful for validation purposes.

The GCMs used in this study were integrated over periods of 10 years and use prescribed sea surface temperatures (SSTs) and sea ice for the period 1979-88 according to AMIP (Atmospheric Model Intercomparison Project; Gates, 1992). On the other hand, the Reanalysis data were integrated over varying periods. The periods available for this study were: 1985-93 for ERA15; 1982-94 for NCEP, and; 1981-92 for GEOS. While these dates are slightly different to those for the GCMs, the averaged monthly climatologies for each model should be similar to those for the AMIP years.

The model resolutions used in this study also vary from model to model. The 3 GCMs were performed at a high resolution: ECHAM4 and ARPEGE were performed at T106 which corresponds to $1.1^o \times 1.1^o$, while HadAM2b was performed at a resolution of $0.833^o \times 1.25^o$. For the Reanalyses, the resolutions correspond to T106 for ERA15, T62 ($2.5^o \times 2.5^o$) for NCEP and $2^o \times 2.5^o$ for GEOS.

The determination of the turbulent fluxes varies with each model and will be discussed below with emphasis on ECHAM4 since this was the main model used in this research. A summary of the resolution and land surface hydrology of each model can be found in Table 2.5.

All the models calculate the turbulent fluxes at the surface according to the bulk transfer relation (Equation 2.52).

$$\overline{(w'\chi')}_s = -C_\chi \, |v_l| \, (\chi_l - \chi_s), \qquad (2.52)$$

where χ is the concentration of the turbulent flux variable (temperature or specific humidity), w is the vertical windspeed, the prime indicates the deviation of the mean of the quantity, C_χ is the transfer coefficient, v_l is the horizontal wind vector at the lowest model level, l (which also represents the top of the constant flux layer), and s is the surface.

2.3.2   ECHAM4 GCM

The ECHAM series of GCMs originally evolved from the spectral weather prediction model of the ECMWF (Simmons et al., 1989). The model is based on primitive equations with 5 layers in the boundary layer (cf. Table 2.5), the highest at roughly 1500 m. The prognostic variables include vorticity, divergence, logarithmic surface

Table 2.5: Model resolutions and parameterisations of GCMs and Reanalyses used in this study.

Group	Model Resolution	Vertical Levels	Levels in BL	Land Surface Hydrology	Soil Layers for Heat and Hydrology
MPI	ECHAM4 T106	19 hybrid	5	Dümenil and Todini (1992) - bucket-type model for soil moisture, depth varies geographically	Heat - 5 Hyd. - 1
UKMO	HadAM2b $0.833^o \times 1.25^o$	19 hybrid	5	Smith (1996) and Dolman and Gregory (1992)	Heat - 4 Hyd. - 4
CNRM	ARPEGE T106	30 hybrid	4	ISBA (Noilhan and Planton, 1989)	Heat - 2 Hyd. - 1
ECMWF	ERA15 T106	31 hybrid	6	Gibson et al. (1997)	Heat - 4 Hyd. - 4
NCEP/ NCAR	NCEP T62	28 sigma	7	Pan and Mahrt (1987) - simple SiB model	Hyd. - 2
NASA/ DAO	GEOS $2^o \times 2.5^o$	20 sigma	4	no land surface model - soil moisture computed offline with a simple bucket model	no land surface model

pressure, temperature, specific humidity and the mixing ratio of total cloud water. A semi-implicit time stepping scheme is used in conjunction with a weak time filter to avoid decoupling of the solutions. The time step is resolution dependent but, at T106, is typically 12 minutes for the dynamics and physics, except for radiation. The three-dimensional transport of water vapour, cloud water and trace constituents is calculated by using a semi-Lagrangian scheme (Williamson and Rasch, 1994). This scheme uses a shape preserving interpolation form which avoids the generation of spurious maxima and minima. Thus, it does not produce, for instance, negative values or spurious rain through the generation of supersaturation by the transport of water vapour. The one disadvantage of the semi-Lagrangian scheme is that it is not inherently conservative. Thus, mass conservation must be forced at every time step. Lastly, land surface data is prescribed during the course of the integration. These variables include orography, background albedo, roughness length, vegetation type, *LAI* and soil parameters. More details can be found in Roeckner et al. (1996).

As mentioned, the surface fluxes of momentum and heat are determined using Equation 2.52. The transfer coefficients at the surface (Equation 2.53) in ECHAM4 are obtained from Monin-Obukhov similarity theory by integrating the flux-profile relationships over the lowest model layer and are based on Louis (1979).

$$C_{m,h} = C_N \, f_{m,h} \left(Ri_B, \frac{z_l}{z_0} + 1, \frac{z_l}{z_{0h}} + 1 \right), \tag{2.53}$$

where $C_{m,h}$ is the transfer coefficient of momentum m or heat h, C_N is the neutral transfer coefficient (Equation 2.54), Ri_B is the 'moist' Bulk Richardson Number (which is described below), z_l is the height at the lowest model level (m), z_0 and z_{0h} are the roughness lengths for momentum and heat (m), respectively and f_m and f_h are the stability functions for momentum and heat, respectively given by Equations 2.55 - 2.57. In ECHAM4, z_{0h} equals z_0.

$$C_N = \frac{k^2}{\ln(\frac{z_l}{z_0} + 1) \ln(\frac{z_l}{z_{0h}} + 1)}, \tag{2.54}$$

$$f_{m,h} = 1 - \frac{a_{m,h} Ri_B}{1 + 3c^2 C_N \sqrt{-Ri_B(\frac{z_l}{z_0} + 1)}} \quad \text{for } Ri_B < 0, \tag{2.55}$$

$$f_m = \frac{1}{1 + a_m Ri_B / \sqrt{1 + cRi_B}} \quad \text{for } Ri_B \geq 0, \tag{2.56}$$

$$f_h = \frac{1}{1 + a_h Ri_B \sqrt{1 + cRi_B}} \quad \text{for } Ri_B \geq 0, \tag{2.57}$$

where $c = 5$, $a_m = 2c$ and $a_h = 3c$.

The 'moist' Bulk Richardson Number (Equation 2.58) used in the above computations is a reformulation of the Bulk Richardson Number to include the impact of water vapour and cloud properties on the buoyancy term (Brinkop, 1992).

$$Ri_B = \frac{g}{\theta_v} \frac{A\Delta\theta_l + \theta B \Delta q_t}{\Delta u^2 + \Delta v^2} \Delta z, \tag{2.58}$$

where g is the acceleration due to gravity (9.81 m s^{-2}), θ_v is the virtual potential temperature (K), θ_l is the liquid water potential temperature (K) which is a conservative quantity in the absence of freezing, precipitation and radiative effects, θ is the potential temperature (K), u and v are the zonal and meridional windspeed (m s^{-1}), respectively, $q_t = q_l + q_i + q_v$ is the total water content (kg kg^{-1}), z is the height (m), q_l, q_i and q_v are the mixing ratios (kg kg^{-1}) for liquid water, ice and water vapour, respectively, and A and B are given by Equations 2.59 and 2.60.

$$A = bA_{sat} + (1 - b)A_{unsat}, \tag{2.59}$$

$$B = bB_{sat} + (1 - b)B_{unsat}, \tag{2.60}$$

where b is the cloud cover and A_{sat}, A_{unsat}, B_{sat} and B_{unsat} are given by Equations 2.61 - 2.64.

64

$$A_{unsat} = 1 + 0.61q_t, \tag{2.61}$$

$$A_{sat} = 1 + 0.61q_t - \frac{0.622\frac{L_v}{R_d T}q_s}{1 + 0.622\frac{L_v{}^2}{R_d C_{pd} T^2}}\left(\frac{L_v}{C_{pd}T}\left(1 + 0.61q_t\right)\right), \tag{2.62}$$

$$B_{unsat} = 0.61, \tag{2.63}$$

$$B_{sat} = \frac{L_v}{C_{pd}T} - 1, \tag{2.64}$$

where A_{unsat} and B_{unsat} are for the unsaturated case, and A_{sat} and B_{sat} are for the saturated case, L_v is the latent heat of vapourisation (J kg^{-1}), R_d is the gas constant for dry air (287.05 J kg^{-1} K^{-1}), C_{pd} is the specific heat of dry air at constant pressure (1005.46 J kg^{-1} K^{-1}), T is the temperature (K), and q_s is the saturation water vapour mixing ratio (kg kg^{-1}).

For the evaluation of the moisture flux over land, each grid square is divided into four fractions. These fractions are divided into snow covered, water in the skin reservoir, vegetation and bare soil components. The moisture flux is then calculated for each fraction and then combined using Equation 2.65.

$$\begin{aligned} E = \ & \rho C_h \left|v\right| [(C_{Sn} + (1 - C_{Sn})C_l)(q_v - q_s) + \\ & (1 - C_{Sn})(1 - C_l)(1 - C_v)(q_v - hq_s) + \\ & (1 - C_{Sn})(1 - C_l)C_v\beta(q_v - q_s)], \end{aligned} \tag{2.65}$$

where E is the moisture flux, C_{Sn} is the fraction covered with snow, $(1 - C_{Sn})C_l$ is the fraction covered with water in the skin reservoir, $(1 - C_{Sn})(1 - C_l)(1 - C_v)$ is the fraction covered with bare soil, $(1 - C_{Sn})(1 - C_l)C_v$ is the fraction covered with vegetation, h is the relative soil water amount given by Equation 2.66, and β is the evaporation efficiency given by Equation 2.67.

$$h = \begin{cases} \frac{1}{2}\left(1 - \cos\left(\pi\frac{w_s - (w_{max} - w_{top})}{w_{top}}\right)\right) & \text{for } w_s > w_{max} - w_{top} \\ 0 & \text{for } w_s \leq w_{max} - w_{top}, \end{cases} \tag{2.66}$$

where w_s is the actual soil amount, w_{max} is the field capacity and w_{top} is the field capacity of the top layer. The upper reservoir is set to $w_{top} = 0.1$ m for $w_{max} > 0.1$ m, and $w_{top} = w_{max}$ otherwise.

$$\beta = \left(1 + \frac{C_h \left|v\right| R_{co}(PAR)}{F(w_s)}\right)^{-1}, \tag{2.67}$$

where PAR is the photosynthetically active radiation and $R_{co}/F(w_s)$ is the stomatal resistance of the canopy given by Equations 2.68 and 2.69.

$$\frac{1}{R_{co}} = \frac{1}{k\,l\,c}\left[\frac{b}{d(PAR)}\ln\left(\frac{de^{j\,LAI} + 1}{d + 1} - \ln\frac{d + e^{j\,LAI}}{d + 1}\right)\right], \tag{2.68}$$

where $d = \frac{a+bc}{c(PAR)}$, $j = 0.9$, $a = 5000$ J m^{-3}, $b = 10$ W m^{-2} and $c = 100$ s m^{-1}. The *LAI* varies with vegetation type for both the growing season and the season of dormancy. In ECHAM4, annual mean values are used which are defined as the arithmetic averages of the seasonal extremes (see Roeckner et al., 1996 for more details).

$$F(w_s) = \begin{cases} 1 & \text{for } w_s \geq w_{cr} \\ \frac{w_s - w_{pwp}}{w_{cr} - w_{pwp}} & \text{for } w_{pwp} < w_s < w_{cr} \\ 0 & \text{for } w_s \leq w_{pwp} \end{cases} \quad , \tag{2.69}$$

where w_{cr} is a critical value taken as 50% of the field capacity and w_{pwp} is the permanent wilting point taken as 20% of the field capacity.

For evaporation, it is assumed that relative humidity at the surface is a function of the water content of the soil. The relative humidity takes into account the fact that evaporation for bare soil can be divided into two regimes: An almost saturated surface evaporating in a similar manner to a free water surface, and; the rate of evaporation determined by atmospheric demand. If the constant flux layer is dry (i.e., no water in the skin reservoir), the evaporation will be controlled by the hydraulic properties of the soil. For wet vegetation and bare soil, the evaporation is at the potential rate. Lastly, for dry vegetation, the evaporation (transpiration) is calculated using the stomatal resistance and a water stress factor, which is a function of the soil moisture. The stomatal resistance is determined from the available water in the root zone, the *PAR* and the *LAI*. For more information, see Wild et al. (1996), Roeckner et al. (1996) and Roesch et al. (1997).

2.3.3   HadAM2b GCM

HadAM2b is a version of the United Kingdom Meteorological Office (UKMO) Unified Model (Cullen, 1993). This model is in hydrostatic, primitive equation mode with 5 model layers in the boundary layer (cf. Table 2.5). At the high resolution used here, HadAM2b uses a time step of 10 minutes.

In HadAM2b, the transfer coefficients are obtained from Monin-Obukhov similarity theory using the formulations in Smith (1996). The approach used directly relates the transfer coefficients to the Richardson Number, the lowest model level and the roughness lengths of both momentum and heat (which are set equal in HadAM2b). For stable conditions, theoretical arguments imply that turbulence should not exist where the Richardson Number is greater than some critical value. Although these arguments are strictly homogeneous and steady states, the size of the gridboxes in HadAM2b allows considerable sub-gridscale inhomogeneity in the stability of the constant flux layer and other surface parameters, particularly over land. This inhomogeneity leads to the presence of turbulence, even for very stable constant flux layers (Mahrt, 1987). Therefore, the transfer coefficients are calculated such that they only tend to zero for an infinite Richardson Number. Thus, the surface never becomes turbulently decoupled from the atmosphere.

On land surfaces with a positive moisture flux, the resistance method of Monteith (1965) is used to calculate evaporation whereby the physiological control of water loss through the vegetation is characterised by the stomatal resistance. Here, the stomatal resistance is a climatologically prescribed, geographically varying quantity dependent on the vegetation type only (Smith, 1996). The vegetation itself has a large affect on surface hydrology over land. Falling water is intercepted by the canopy resulting in drier soils and a reduced soil hydrology cycle. Further, water stored in the canopy only evaporates depending on the aerodynamic resistance, making it larger than for the underlying soil (Gregory et al., 1996).

2.3.4   ARPEGE GCM

The ARPEGE GCM mainly uses the physical parameterisation package of the Météo-France operational model, with some additions including a soil-vegetation scheme with rainfall interception (Déqué and Piedelievre, 1995). The time scheme is a semi-implicit scheme with a time step of 7.5 minutes, and there are 4 levels in the boundary layer (cf. Table 2.5).

As with ECHAM4, the transfer coefficients in ARPEGE are those proposed by Louis (1979) and are functions of the roughness length and Richardson Number. Evaporation is assumed to take place at a potential rate over bare soil when the soil moisture is larger than the field capacity. As with ECHAM4, stomatal resistance is determined from the available water in the root zone, the PAR and the LAI. In addition, the stomatal resistance is dependent on the effects of the vapour pressure deficit of the atmosphere and on the effect of air temperature on the surface resistance (Noilhan and Planton, 1989). Negative humidity values in the bottom layer of the atmosphere are corrected by introducing a fictitious source of water, rather than an additional evaporation from the surface which can lead to spurious desert areas in long-time model integration (Déqué et al., 1994).

2.3.5   ERA15 Reanalysis

The parameterisations in ERA15 are similar to the model used in the ECMWF operations from April 1995 to August 1996 (Betts et al., 1998). It includes the land-surface scheme from Viterbo and Beljaars (1995), the soil moisture initialisation scheme of Viterbo and Courtier (1995), and the subgrid-scale orography scheme of Lott and Miller (1997). This Reanalysis system uses a time step of 30 minutes, and has 6 levels in the boundary layer (cf. Table 2.5).

In ERA15, the surface fluxes of momentum, heat and moisture are not analysed directly, but are determined diagnostically from the model parameterisation, as in the GCMs. To avoid the problem of spin-up, the fluxes were extracted from +24 hour forecasts. The transfer coefficients between the surface (skin) and the lowest model level are not expressed as functions of the Bulk Richardson Number as in Louis (1979), but are expressed as a function of the Obukhov length (Beljaars and Viterbo, 1994). Viterbo and Beljaars (1995) state that one of the advantages of using

this method is that the roughness lengths of momentum, heat and moisture can be chosen independently.

For evaporation, it is assumed that the relative humidity depends on the soil wetness of the top layer. Similarly to ECHAM4, the parameterisation of evaporation is completed in four different surface fractions for each grid box: A snow fraction depending on the depth of the snow layer; a fraction with wet vegetation or bare soil; a fraction with dry bare soil, and; a dry vegetated fraction (Beljaars and Viterbo, 1994). As with ECHAM4, the computation of the stomatal resistance depends on the PAR, LAI and the soil wetness in the root zone. The stomatal resistance is based on an integration across the canopy of the conductances of individual horizontal leaves acting in parallel (Viterbo and Beljaars, 1995). The soil moisture is divided into two components: The skin and soil reservoirs. The skin reservoir (i.e., moisture on the vegetation) evolves due to its own evaporation and its ability to collect dew and intercept precipitation. The soil reservoir takes into account the contributions of precipitation and snow melt, as well as losses due to deep penetration, evaporation over bare soil and root uptake by vegetation (Gibson et al., 1997).

2.3.6   NCEP Reanalysis

The NCEP Reanalysis uses identical parameterisations to the global system that was implemented operationally at the NCEP in January 1995. The only change is that the resolution is T62 in the Reanalysis. Here, a three-dimensional variational analysis scheme (spectral statistical interpolation, SSI) is used as the analysis module (Kalnay et al., 1996). With the use of SSI, it is unnecessary to use an initialisation procedure (see Kalnay et al., 1996 for more details). The time step is 20 minutes for the computation of the dynamics and physics, except radiation which is computed once every 3 hours. The extraction of variables are from +6 hour forecasts. There are 7 levels in the boundary layer (cf. Table 2.5).

The transfer coefficients in NCEP are also based on the formulations of Louis (1979) using Monin-Obukhov similarity theory. The evaporation in NCEP is related to the soil moisture deficit and plant resistance to transpiration as discussed in Monteith (1981). Land surface evaporation is comprised of 3 components: Direct evaporation from the soil; direct evaporation from vegetation, and; transpiration from vegetation. The vegetation cover is set at a constant of 0.7 over the globe. The computation of potential evaporation (which is required to determine the actual evaporation) follows the Penman method (Mahrt and Ek, 1984) with increased numerical efficiency and the addition of upward longwave radiation depending on temperature (Troen and Mahrt, 1986). The soil wetness is updated during the analysis cycle and uses the soil model of Pan and Mahrt (1987). Soil moisture is only slightly nudged towards climatology. As with the other models, the NCEP Reanalysis does not distinguish between the surface air temperature at the level of the roughness elements as used in surface-layer similarity theory and the effective surface radiation temperature.

68

2.3.7   GEOS Reanalysis

GEOS consists of an Optimal Interpolation (OI) analysis scheme and an Incremental Analysis Update (IAU) assimilation technique (Molod et al., 1996). The OI scheme is a statistical interpolation scheme that uses the specified observational and random model errors, and determines an "optimal" analysed atmospheric state. The IAU procedure utilises both intermittent analysis and continuous assimilation. The analysis is performed every 6 hours, but the increments are not added as impulse forcings to the first guess state. Instead, the analysis increments are normalised and included in a constant forcing term during model reintegration over the 6 hour time span centred around the analysis time. The time step is 10 minutes for moist convection, 30 minutes for turbulence and 3 hours for radiation (Bloom et al., 1996). As with NCEP, variables are extracted from +6 hour forecasts. There are 4 levels in the boundary layer (cf. Table 2.5).

The transfer coefficients in GEOS are obtained from Monin-Obukhov similarity theory by selecting similarity functions that approach the convective limit for unstable profiles (Panofsky, 1973) and that agree with observations for very stable profiles (Clarke, 1970). GEOS does not have a coupled land surface model and requires soil moisture to be specified. The determination of the soil moisture climatology is based on Thornthwaite (1948) and Mintz and Serafini (1992), and does not account for frozen ground or ice formation. The potential evapotranspiration (which is required to determine the actual evapotranspiration) is estimated as a function of monthly mean air temperature and the duration of daylight (Schemm et al., 1992).

2.3.8   Summary of Model Description

The ECHAM4, HadAM2b and ARPEGE GCMs, as well as ERA15, NCEP and GEOS Reanalyses have been described. Typically, the surface turbulent fluxes in each model are determined using the bulk transfer relation of Louis (1979) with the transfer coefficients determined from Monin-Obukhov theory. The largest difference between the models is in the land surface hydrology where models can range from having no land surface model (GEOS) to a geographically varying soil moisture depth (ECHAM4) or a multi-level soil moisture model (ERA15 and HadAM2b).

2.4   Summary of Methods Chapter

The validation of the turbulent fluxes in GCMs and Reanalyses is necessary to improve these models for climate studies. This study focuses on the GCMs ECHAM4, HadAM2b and ARPEGE, as well as 3 Reanalysis models: ERA15, NCEP and GEOS. While each of these models has similar characteristics such as integrations periods and the use of the bulk transfer relationship for the determination of the fluxes, there are also signifcant differences such as the determination of the land surface hydrology. The differences in these models is expected to lead to differences in the turbulent fluxes (see the Results Chapter). In order to verify which model represents

the turbulent fluxes most accurately, it is necessary to obtain observed climatologies. This study uses sites from GEBA, with emphasis on sites that have long term measurements (3 years for latent heat flux and 12 months for sensible heat flux). Additionally, the site of Cabauw, The Netherlands is used. Lastly, two new sites are analysed for this study: Swampy Summit, New Zealand and MRI, Tsukuba, Japan. The New Zealand site measured latent heat flux for 6 years, while the site in Japan has sensible and latent heat flux, as well as momentum flux, for 2 years. Emphasis is placed on the MRI, Tsukuba, Japan site since it provides measurements for the boundary layer, as well as surface measurements. Results at MRI show that the profile method produces very different fluxes depending on which method is used. In general, the iterative method using the functions of Beljaars and Holtslag (1991) shows reasonable agreement with observations, but the analytical method using the functions of Högström (1996) tends to overestimate the sensible heat flux due to the inhomogeneity of the site. New equations were determined to better represent the site, although it must be emphasised that these equations are dependent on the roughness of the site.

Chapter 3

Results

3.1 Introduction

This chapter will be broken up into the following parts: An intercomparison between models on a global, zonal and regional basis and a comparison of the models used here to the observations.

3.2 Analysis of Models

3.2.1 Introduction

In the following, the sensible and latent heat flux from the six models used in this study will be compared to each other globally, zonally and regionally over Europe. In each subsection, the merits and/or problems of each model will be discussed to determine which models show promising results for the turbulent fluxes.

3.2.2 Global Annual Means

As a first approach to analysing GCMs and Reanalyses, a comparison of the annual global means of the turbulent heat fluxes over land (Table 3.1), over sea (Table 3.2) and the total global means (Table 3.3) are shown. These tables show that there are large differences between the models. In all tables, fluxes are positive when directed towards the surface. As can be expected, there is a large difference between land fluxes and sea fluxes (Tables 3.1 and 3.2). For example, the latent heat flux over the sea is generally twice as big as that over land. The only exception is for GEOS, which has a very high latent heat flux over land, and a very low latent heat flux over sea. This will be discussed in more detail later in the section. Contrarily, the sensible heat flux is generally substantially higher on land than on sea. Again, GEOS is the sole exception. These values are reflected in the Bowen Ratio, which shows higher values over land than over sea (again, with the exception of GEOS). Finally, the net radiation is somewhat larger over the sea than over land.

71

As seen in Table 3.1, for the latent heat flux over land, ECHAM4 shows the lowest value (-39 W m^{-2}), while GEOS and ARPEGE show the highest values with -60 W m^{-2} and -57 W m^{-2}, respectively. Alternatively, ARPEGE and GEOS show the lowest values of sensible heat flux (-16 W m^{-2} and -10 W m^{-2}, respectively), while HadAM2b shows the highest value with -42 W m^{-2}. These values are further reflected in the Bowen Ratio ($\beta = \frac{H_s}{L_v E}$). GEOS and ARPEGE have low Bowen Ratios (0.17 for GEOS and 0.28 for ARPEGE), while the Bowen Ratio for HadAM2b is very high at 0.98. Lastly, the net radiation ranges from 68 W m^{-2} and 69 W m^{-2} in ECHAM4 and ERA15, respectively, to 97 W m^{-2} in GEOS. The large range in values is indicative of the difficulty in estimating the turbulent fluxes. The large differences between the models occur for a variety of reasons which will be discussed later.

Table 3.1: The global annual turbulent fluxes over land. $L_v E$ is the latent heat flux (W m^{-2}), H_s is the sensible heat flux (W m^{-2}), β is the Bowen Ratio (dimensionless) and R_n is the net radiation (W m^{-2}).

	$L_v E$	H_s	β	R_n
ECHAM4	-39	-23	0.59	68
HadAM2b	-43	-42	0.98	85
ARPEGE	-57	-16	0.28	71
ERA15	-44	-24	0.55	69
NCEP	-52	-26	0.50	80
GEOS	-60	-10	0.17	97

As seen in Table 3.2, for the latent heat flux over the sea, GEOS shows the lowest value (-77 W m^{-2}), while HadAM2b shows the highest value with -114 W m^{-2}. Alternatively, ARPEGE shows the lowest value of sensible heat flux (-1 W m^{-2}), while GEOS shows the highest value with -21 W m^{-2}. For the Bowen Ratio, ARPEGE has a low Bowen Ratio (0.01), while the Bowen Ratio for GEOS is high at 0.27. Lastly, the net radiation ranges from 105 W m^{-2} and 106 W m^{-2} in ARPEGE and ECHAM4, respectively, to 125 W m^{-2} and 130 W m^{-2} in HadAM2b and GEOS, respectively.

As seen in Table 3.3, for the total global latent heat flux, GEOS shows the lowest value (-72 W m^{-2}), while HadAM2b and ARPEGE show the highest values with -94 W m^{-2} and -90 W m^{-2}, respectively. Alternatively, ARPEGE shows the lowest values of sensible heat flux (-5 W m^{-2}), while HadAM2b shows the highest value with -22 W m^{-2}. These values are also reflected in the Bowen Ratio. ARPEGE has a low Bowen Ratio (0.06), while the Bowen Ratio for HadAM2b and GEOS are high at 0.23 and 0.24, respectively. Lastly, the net radiation ranges from 95 W m^{-2} in ECHAM4 and ERA15, to 120 W m^{-2} in GEOS.

The relatively low latent heat flux in ECHAM4, ERA15 and NCEP seen in Tables 3.1 and 3.3 is attributable to low incoming solar radiation when compared to the other models. However, it is important to note that the incoming solar radiation in ECHAM4 and ERA15 is in line with observations (Wild, 2000), thus suggesting

Table 3.2: The global annual turbulent fluxes over sea. L_vE is the latent heat flux (W m^{-2}), H_s is the sensible heat flux (W m^{-2}), β is the Bowen Ratio (dimensionless) and R$_n$ is the net radiation (W m^{-2}).

	L_vE	H$_s$	β	R$_n$
ECHAM4	-96	-9	0.09	106
HadAM2b	-114	-13	0.12	125
ARPEGE	-103	-1	0.01	105
ERA15	-99	-9	0.09	109
NCEP	-92	-11	0.12	109
GEOS	-77	-21	0.27	130

Table 3.3: The total global annual turbulent fluxes. L_vE is the latent heat flux (W m^{-2}), H_s is the sensible heat flux (W m^{-2}), β is the Bowen Ratio (dimensionless) and R$_n$ is the net radiation (W m^{-2}).

	L_vE	H$_s$	β	R$_n$
ECHAM4	-80	-13	0.16	95
HadAM2b	-94	-22	0.23	113
ARPEGE	-90	-5	0.06	95
ERA15	-84	-13	0.16	97
NCEP	-80	-15	0.19	101
GEOS	-72	-17	0.24	120

that the latent heat flux in the other models is too high. These models also appear to realistically partition the net radiation into latent and sensible heat fluxes.

HadAM2b also has a relatively low latent heat flux over land which is comparable to ERA15, although the net and solar radiation is high (Table 3.1). HadAM2b has a large summer drying which decreases the water supply towards the end of summer. Thus, even though the solar radiation is high, the soil moisture quickly reaches wilting point leading to a sudden decrease in evaporation. As a result, the annual mean of the latent heat flux for HadAM2b agrees well with ERA15, even though the monthly values are largely different. This problem in HadAM2b is further reflected in the sensible heat flux, which is very high over land. With the high radiation unable to produce more evaporation, the remaining energy goes directly into sensible heat flux. Over the sea (Table 3.2), the high radiation in HadAM2b produces an overestimation in the latent heat flux. Here, the sensible heat flux is comparable with the other models since evaporation can reach much higher values than over land. Globally (Table 3.3), the net radiation is much larger than ECHAM4 and ERA15 (which are considered to be similar to observations, as mentioned above). As a result, the latent heat flux is larger than other models (due to the high radiation causing a high latent heat flux over the sea), and the sensible heat flux is larger than other models (due to the high radiation causing a summer drying over land).

The high latent heat flux in ARPEGE can be attributed to a too intense zonal flow which produces an excessive moist advection. This increases the precipitation (over land and sea) and soil moisture (over land; Doblas-Reyes et al., 1998). The too intense zonal flow is due to orographic and heating contrast forcings that are not well represented in the model (Deland, 1964), and an incorrect transient forcing of the stationary waves (Stephenson and Held, 1993). The sensible heat flux is low due to a relatively low solar radiation. The energy is first partitioned into latent heat flux, leaving a deficit for sensible heat production since the latent heat flux is too high.

Finally, the high latent heat flux in GEOS over land (Table 3.1) is most likely attributable to 3 reasons: The lack of vegetation control in GEOS (Molod, *pers. comm.*); an overestimation of the solar radiation (Wild, 2000), and; an associated too warm surface in JJA (Molod, *pers. comm.*). The lack of vegetation control and the overly warm surface also produces a soil heat flux that is too high, resulting in a very low sensible heat flux. Over sea (Table 3.2), the exceptionally warm surface in JJA produces a surface heat flux and sensible heat flux that is unrealistically high. Although the net radiation is high, the available energy is mainly partitioned into surface heat flux and sensible heat flux, leaving an underestimation for the latent heat flux. This facet is also seen in Table 3.3.

3.2.3 Zonal Means

Zonal values of latent heat flux, sensible heat flux and incoming solar radiation are shown in Figures 3.1−3.9 to further emphasise differences between models. Again, positive fluxes are directed towards the surface. Whilst the overall pattern between the GCMs and Reanalyses is similar, a number of differences are apparent. The differences between the models will be discussed in more detail below.

The latent heat flux over land (Figures 3.1−3.3) generally varies by approximately 50 W m^{-2} in the summer hemisphere, with ECHAM4, ERA15 and NCEP displaying, in general, the lowest values and GEOS and ARPEGE generally showing the highest. These differences appear to be due to the variation in the incoming solar radiation, although other factors such as soil moisture availability (see Section 3.2.4) are also influential.

Wild et al. (1996) state that ECHAM4 shows a good agreement of latent heat flux to observations. Thus, it is obvious that the other models, particularly GEOS and ARPEGE, are much higher than observed.

For ARPEGE, a high latent heat flux over land is present since the model produces a zonal flow which is too intense. This, in turn, produced an excessive moist advection which increases precipitation and soil moisture (Doblas-Reyes et al., 1998). The zonal solar radiation over land in ARPEGE is quite changeable with bands of low and high radiation which, in turn, also affects the latent heat flux.

On the other hand, GEOS produces a high latent heat flux over land since there is no vegetation control over total evaporation leading to a soil moisture which is too high (see Section 3.2.4).

Figure 3.1: Zonal means over land for the latent heat flux, sensible heat flux and solar radiation for December-January-February. Units are in W m^{-2}.

Figure 3.2: Zonal means over land for the latent heat flux, sensible heat flux and solar radiation for June-July-August. Units are in W m^{-2}.

Figure 3.3: Annual zonal means over land for the latent heat flux, sensible heat flux and solar radiation. Units are in W m^{-2}.

HadAM2b is a special case whereby the latent heat flux over land seems accurate for JJA and annually, but problems exist concerning the reason. The solar radiation in HadAM2b is relatively high when compared to ECHAM4, but the latent heat flux is constrained by the lack of soil moisture in late summer. In early summer, high radiation causes a runaway latent heat flux until the soil moisture reaches wilting point. Following this, the latent heat flux is considerably too low leading to the seasonal mean being comparable to ECHAM4 by cancellation.

The sensible heat flux over land also varies by approximately 50 W m^{-2} in the summer hemisphere. However, for the sensible heat flux, the lowest values are typically in ARPEGE, while the highest values are in HadAM2b. The sensible heat flux over land appears to be affected by both the incoming solar radiation and the surface temperature (not shown). A similar conclusion can be drawn from the winter hemisphere although the magnitude is somewhat smaller.

For ARPEGE, the latent heat flux over land is not water limited (as discussed above), leaving insufficient energy for sensible heat flux production. On the other hand, the sensible heat flux over land in HadAM2b is high for the same reason that the latent heat flux is low in the summer hemisphere. Towards the end of summer, the soil moisture reaches wilting point. Thus, since there is no longer sufficient moisture available for evaporation, the radiation goes directly into the production of sensible heat flux.

Figures 3.4−3.6 show the latent heat flux, sensible heat flux and incoming solar radiation over the sea.

The latent heat flux over the sea generally varies by nearly 100 W m^{-2} in the summer hemisphere. One of the largest differences between Figures 3.4−3.6 and those over land is that GEOS now shows a much smaller latent heat flux than the other models, while HadAM2b shows very large values, regardless of the season. For GEOS, a large overestimation in the net radiation coupled with a surface that is too warm leads to an unrealistically large surface heat flux. While the sensible heat flux appears to be comparable to the other models, the exceptionally large surface heat flux reduces the available energy partitioned into latent heat flux, leading to an underestimation of the latent heat flux. For HadAM2b, in the case over land, the latent heat flux is constrained by the lack of soil moisture in late summer. In early summer, high radiation causes a runaway latent heat flux until the soil moisture reaches wilting point. Over the sea, there is no constraint of moisture which leads to an even larger runaway affect of latent heat flux than over land.

As mentioned for the land surface, Wild et al. (1996) mention that ECHAM4 shows a good agreement of latent heat flux to observations. Thus, over the sea, it is obvious that GEOS is much too low, and HadAM2b is higher than observed.
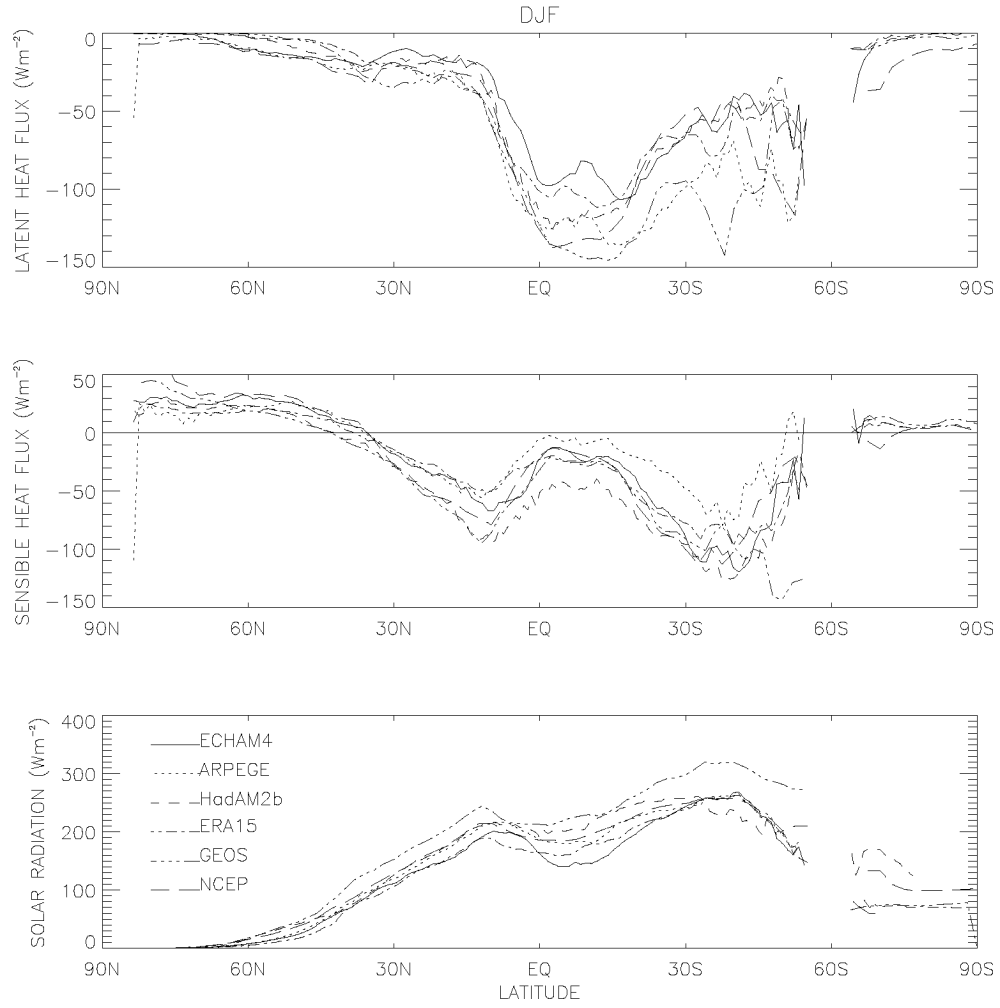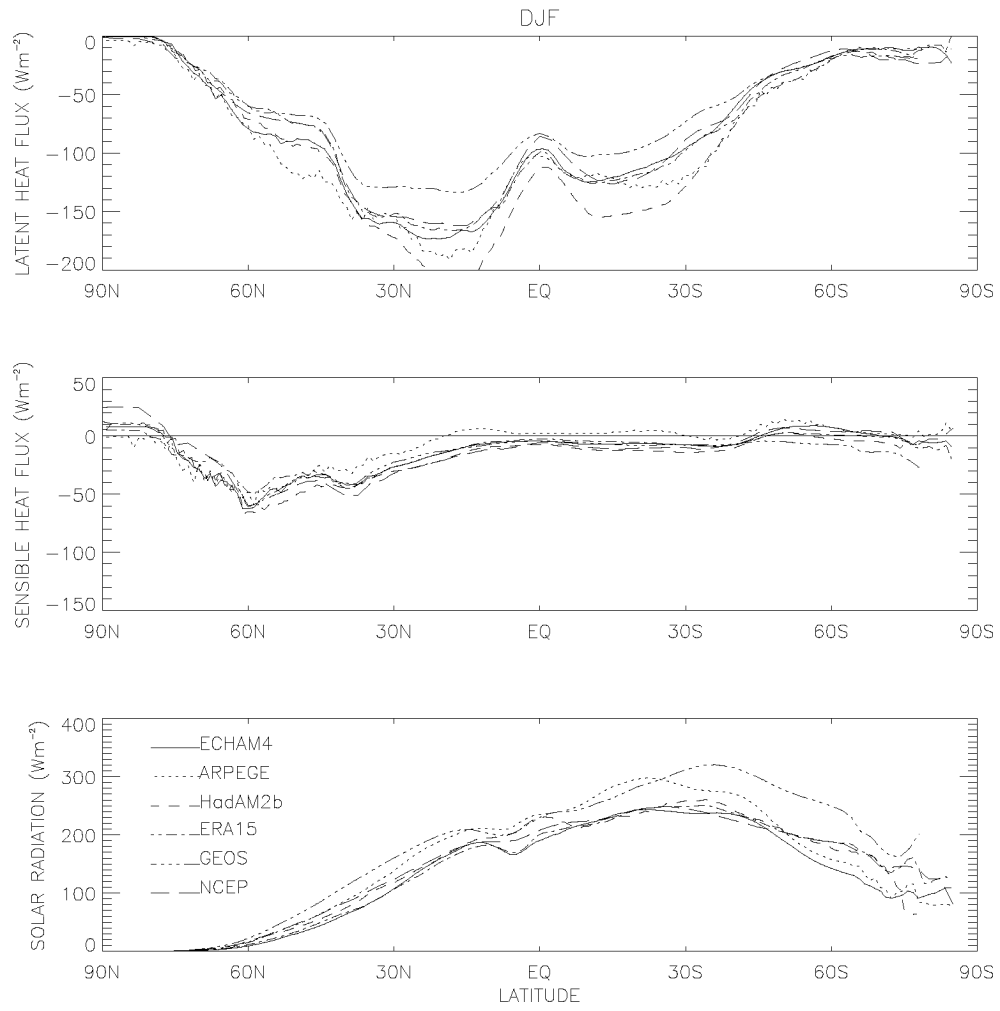
Figure 3.4: Zonal means over the sea for the latent heat flux, sensible heat flux and solar radiation for December-January-February. Units are in W m^{-2}.
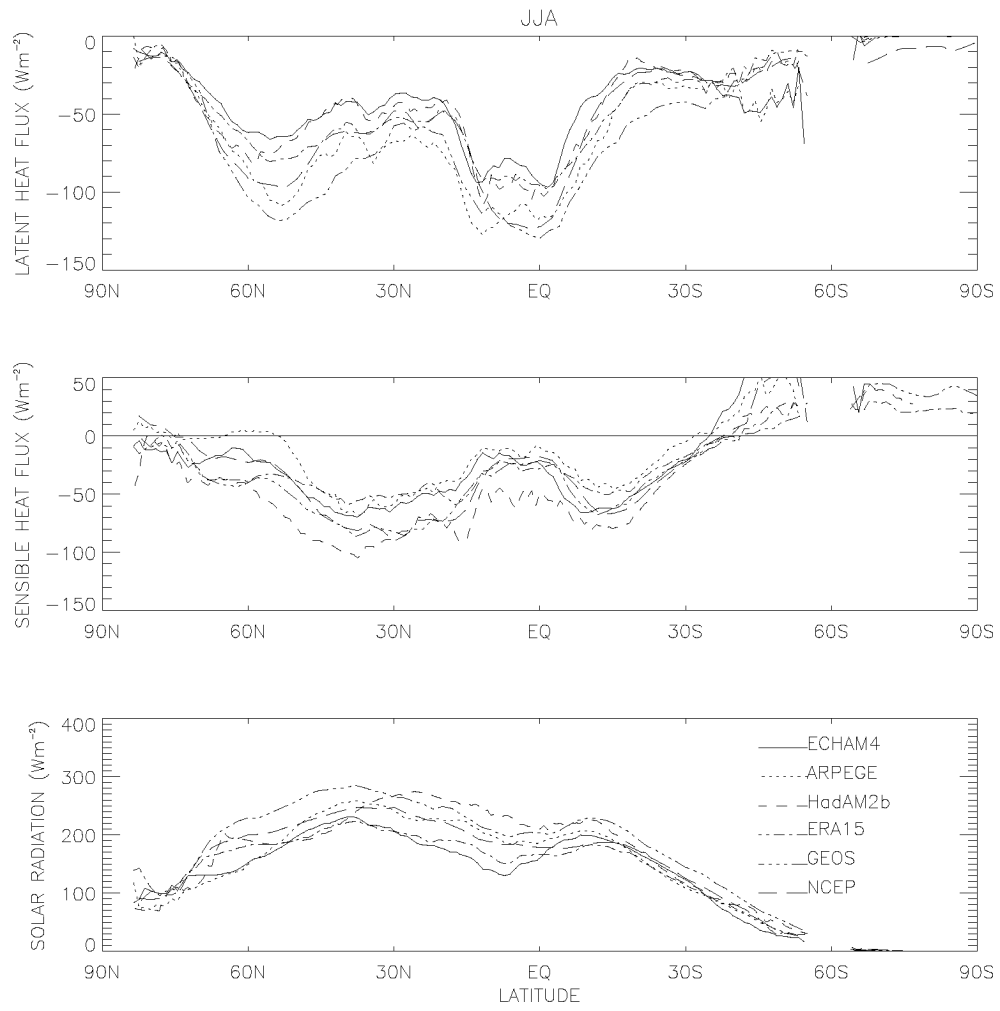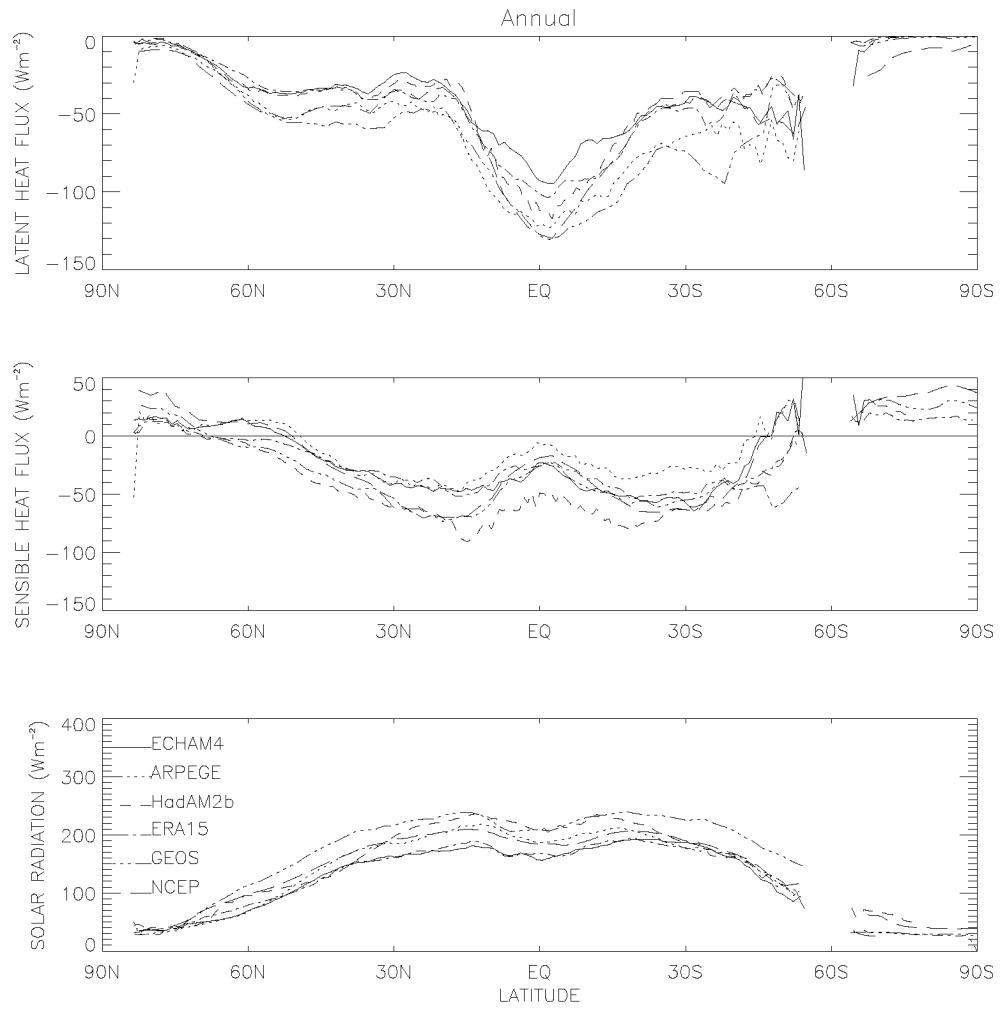
Figure 3.5: Zonal means over the sea for the latent heat flux, sensible heat flux and solar radiation for June-July-August. Units are in W m^{-2}.

Figure 3.6: Annual zonal means over the sea for the latent heat flux, sensible heat flux and solar radiation. Units are in W m^{-2}.

Finally, Figures 3.7−3.9 show the latent heat flux, sensible heat flux and incoming solar radiation for the entire globe.

Figure 3.7: Global zonal means for the latent heat flux, sensible heat flux and solar radiation for December-January-February. Units are in W m^{-2}.

Figures 3.7−3.9 shows all facets of the previous 6 figures. GEOS shows a latent heat flux that is too high during summer in the Northern Hemisphere, but too low in the winter of either hemisphere (DJF for the Northern Hemisphere or JJA for the Southern). However, it is comparable to the other models for the Southern Hemisphere during summer. The high incoming solar radiation, together with the lack of vegetation control, leads to a very high latent heat flux for JJA in the Northern Hemisphere. Otherwise, the overestimation in the solar radiation leads to an unrealistic soil heat flux that reduces the available energy to the point that latent heat flux must be underestimated.

HadAM2b also shows noticeable problems on a global basis. The latent heat flux is constantly too high due to a high incoming solar radiation. Further, the latent heat flux is not water limited over the sea, giving the global averages a much larger value.

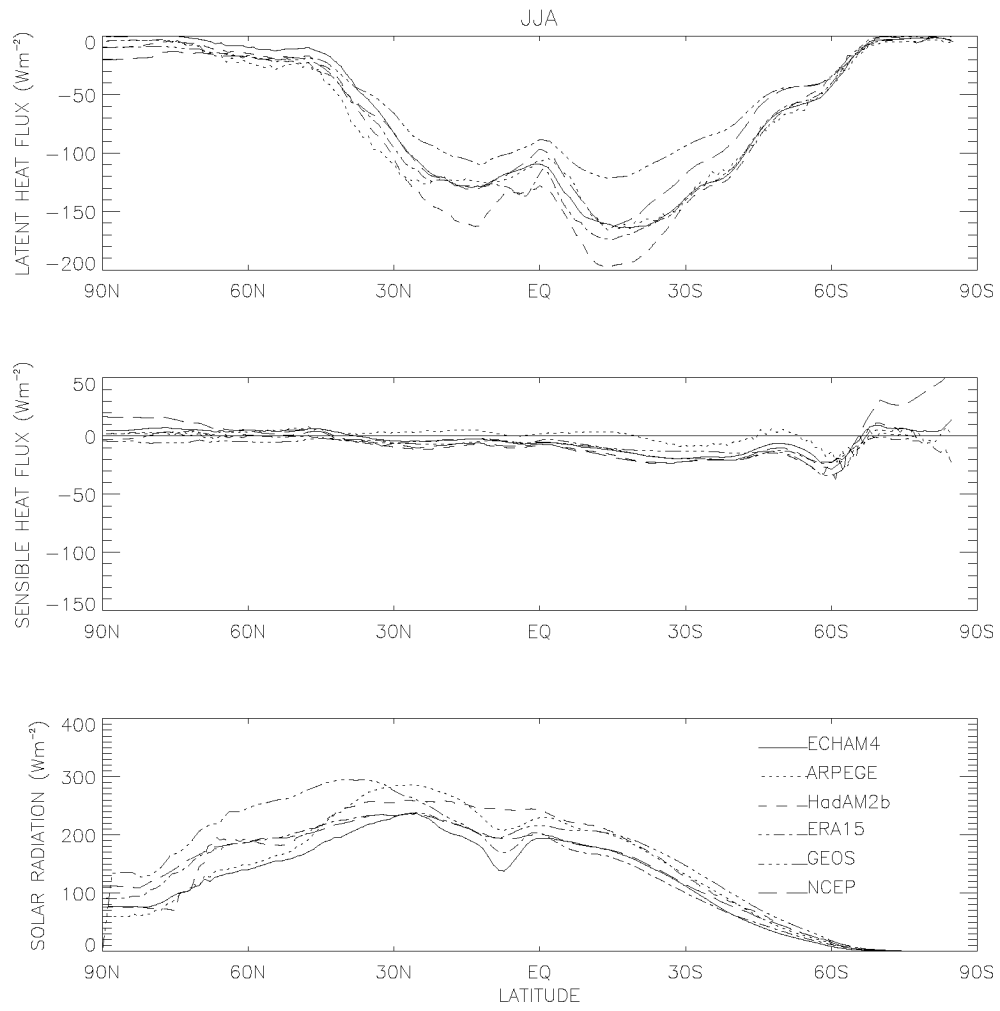**Figure 3.8:** Global zonal means for the latent heat flux, sensible heat flux and solar radiation for June-July-August. Units are in W m^{-2}.

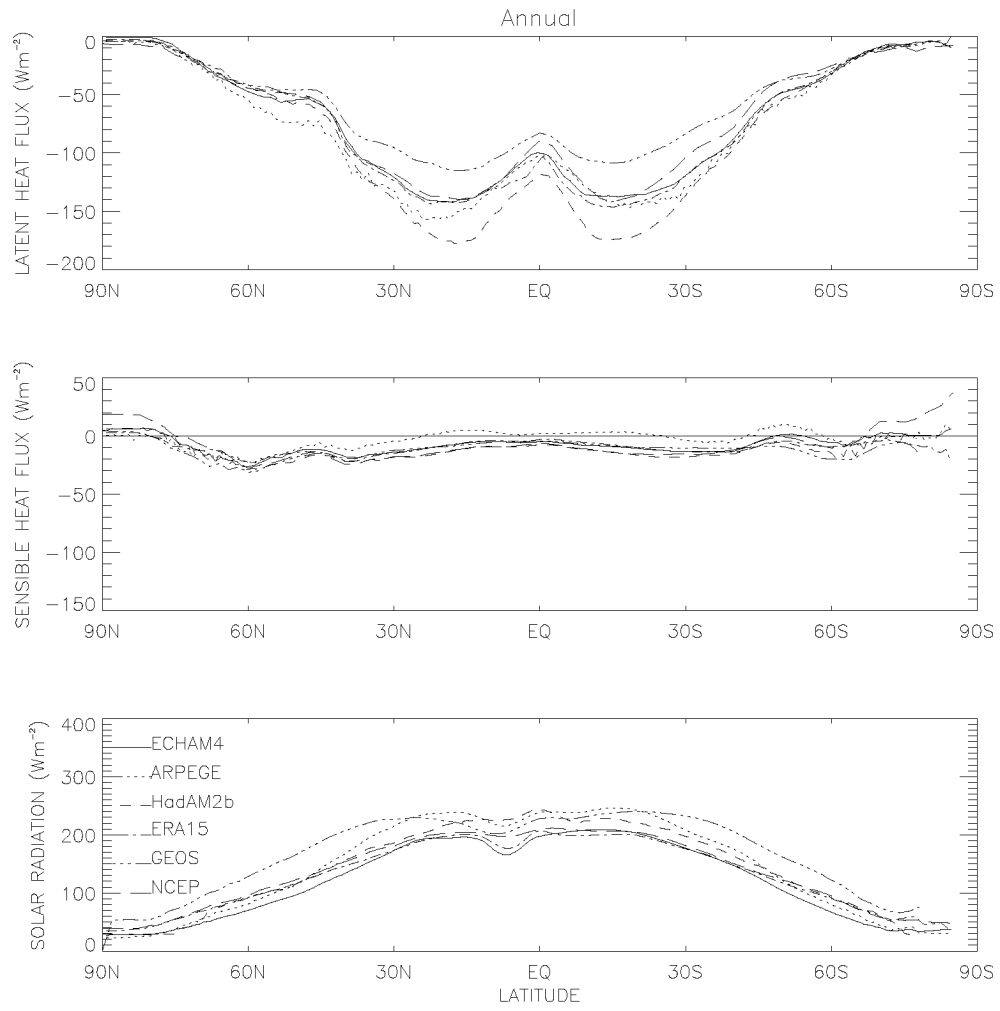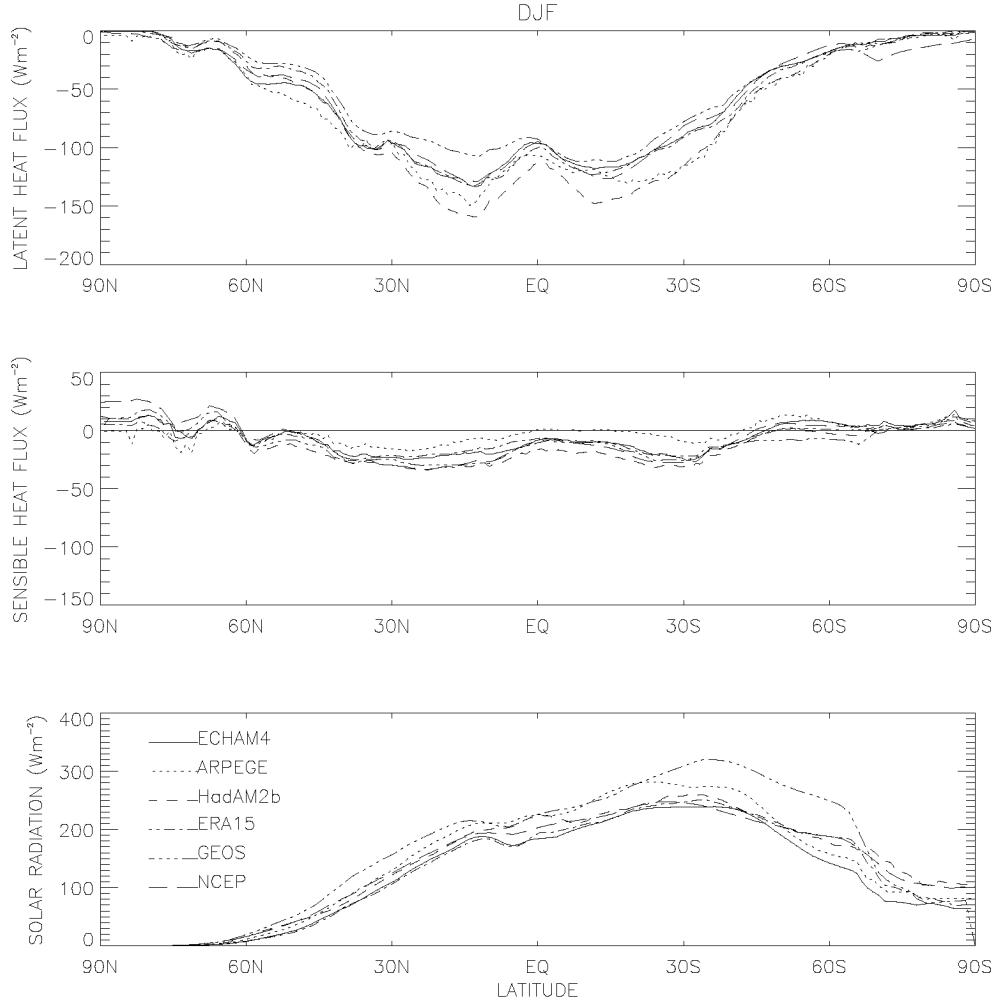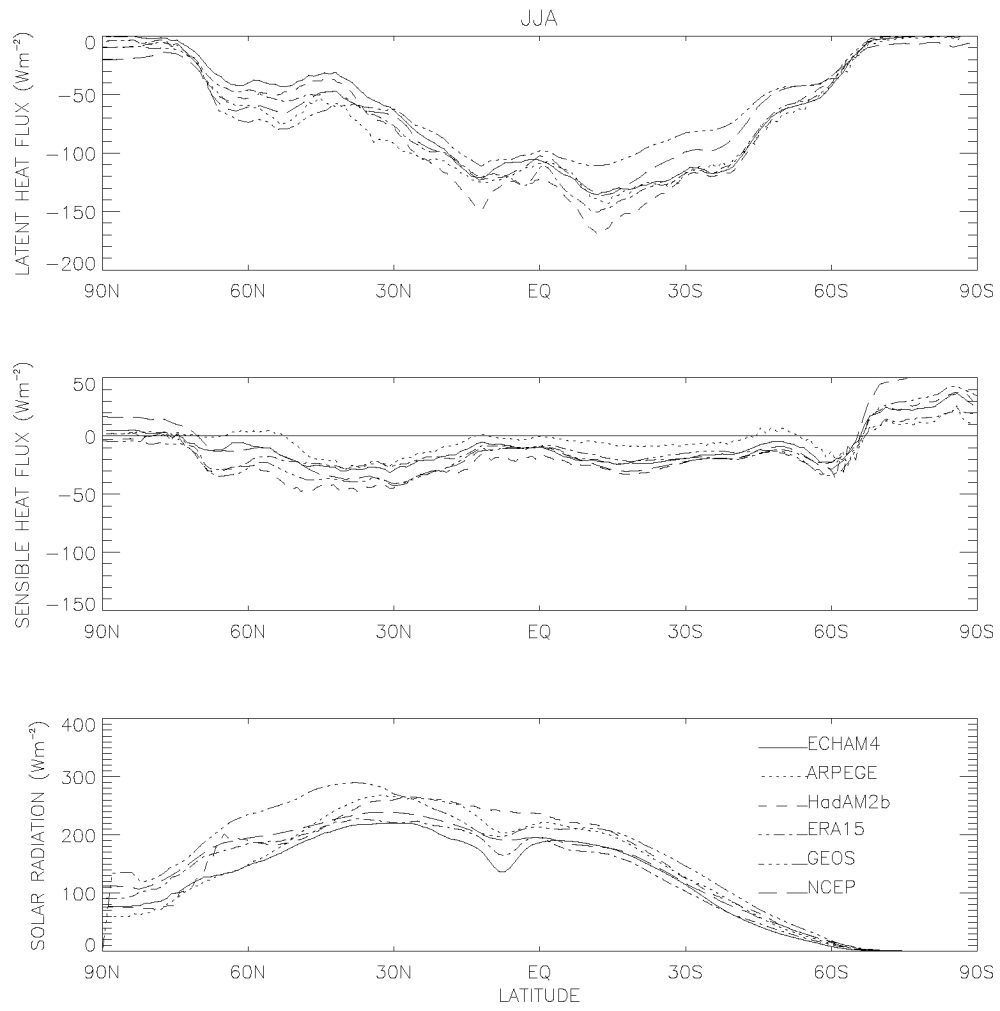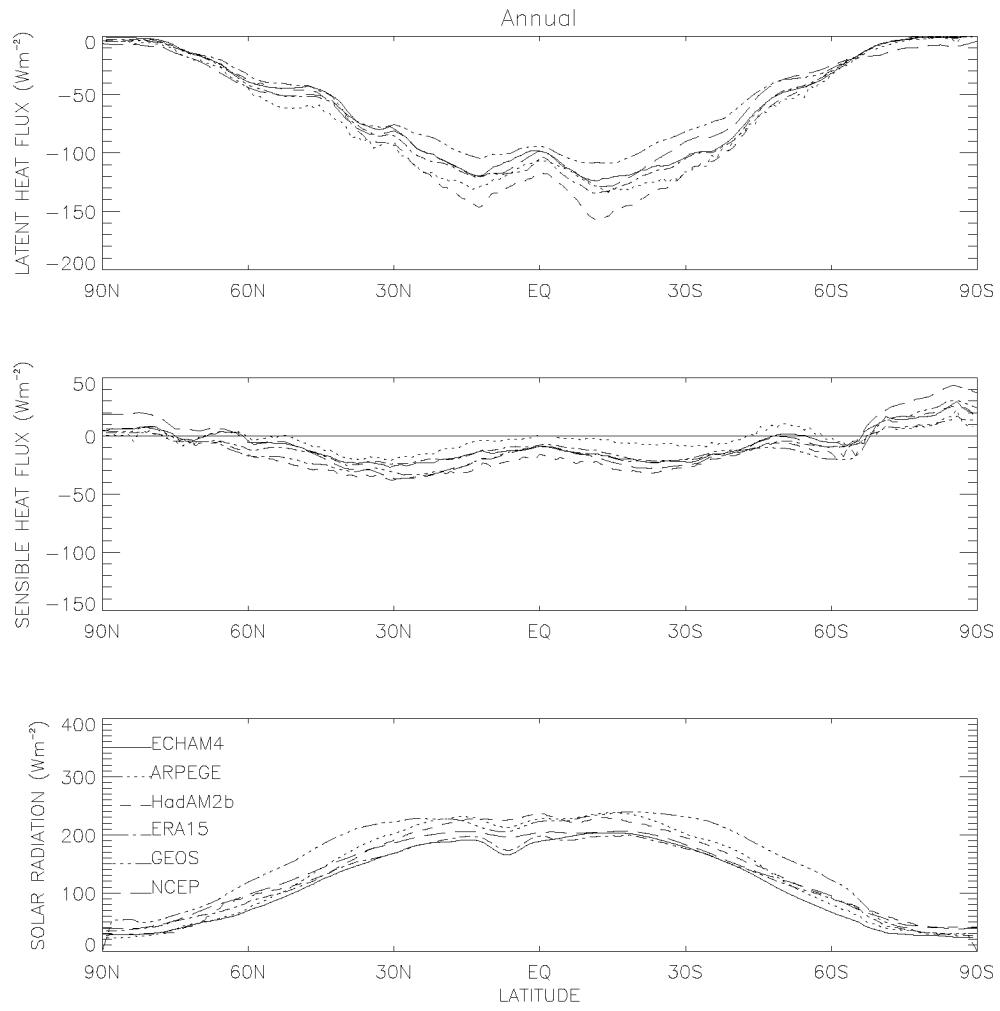**Figure 3.9:** Annual global zonal means for the latent heat flux, sensible heat flux and solar radiation. Units are in W m^{-2}.

For ARPEGE, the high latent heat flux over the globe is present since the model produces a zonal flow which is too intense. This, in turn, produced an excessive moist advection which increases precipitation and soil moisture. It is also interesting to note that the sensible heat flux is somewhat smaller than the other models, suggesting that the available energy is being used predominantly by the latent heat flux.

3.2.4 Regional Means

On a regional basis, variations between models are even more pronounced (Figures 3.10−3.21). The remainder of this discussion will focus over Europe for DJF, JJA and annually.

ECHAM4 shows the lowest latent heat flux both in JJA and annually (Figures 3.11 and 3.12). In DJF (Figure 3.10), all models produce a similar latent heat flux. According to Wild et al. (1996), the latent heat flux for ECHAM4 is in good agreement with observations. Unlike many of the other models studied here, ECHAM4 does not overestimate solar radiation when compared to observations (Wild et al., 1996, Wild and Ohmura, 1999). Thus, the latent heat flux is well represented in this model. Further, Figures 3.13−3.15 show the sensible heat flux which is comparable to the other models. However, it is important to note that ECHAM4 has a high artificially generated soil heat flux in the Northern Hemisphere in JJA (14 W m^{-2}), which decreases the amount of available energy for the sensible heat flux (Schulz et al., 1999). Thus, a correction of this would lead to values of the sensible heat flux slightly above what is currently shown in Figure 3.14. Lastly, Figures 3.16−3.18 show the Bowen Ratio. Typically, the Bowen Ratio in ECHAM4 is comparable to the other models in DJF, but is slightly higher in JJA and annually. This is mainly due to the slightly low latent heat flux as discussed above.

HadAM2b, similarly to ECHAM4, shows a relatively low latent heat flux throughout the year over Europe (Figures 3.10−3.12). In JJA (Figure 3.11), this is predominantly due to a large summer drying which decreases the water supply towards the end of summer (Figure 3.22). Although the radiation in HadAM2b is slightly high compared to ECHAM4 (Figure 3.20), evaporation can only continue until the soil moisture reaches wilting point. Thus, the overall summer mean for evaporation is only slightly higher than ECHAM4. This is also seen in the Bowen Ratio which shows very high values over Europe in JJA (Figure 3.17), but slightly low values in DJF (Figure 3.16). This is emphasised by a very high sensible heat flux in JJA (Figure 3.14), which is also a characteristic of the drying in summer. Since the energy can no longer be used for latent heat flux towards the end of summer, it goes directly into the sensible heat flux.

ARPEGE, unlike HadAM2b, has a very high latent heat flux in JJA and annually (Figures 3.11−3.12). This model exhibits a too intense zonal flow, mainly in winter, which produces an excessive moist advection thus increasing precipitation and soil moisture (Doblas-Reyes et al., 1998). This, in combination with a high radiation locally over Europe and mainly in summer (Figure 3.20−3.21), produces a very high latent heat flux. However, the sensible heat flux (Figure 3.14−3.15), and
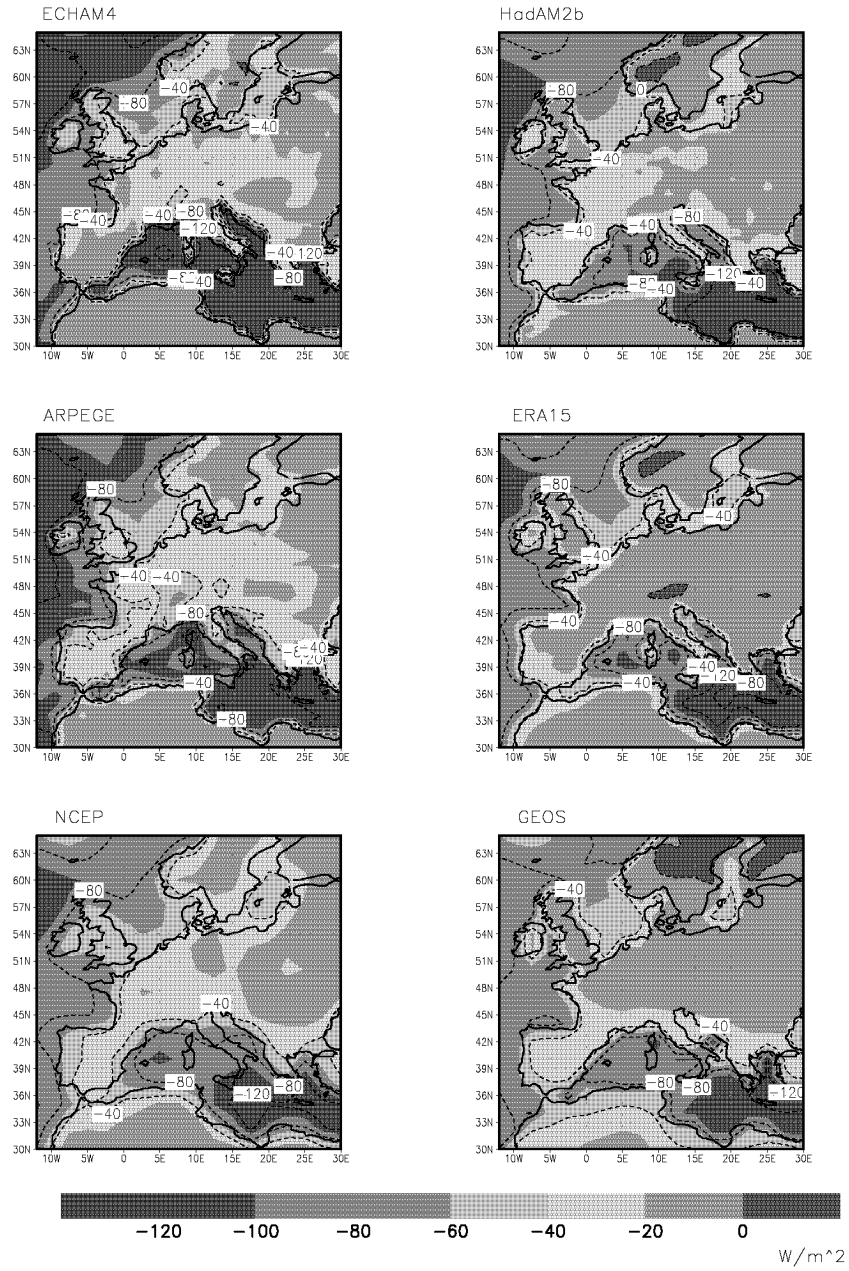
Figure 3.10: The latent heat flux over Europe for December-January-February. Units are in W m^{-2}.

consequently the Bowen Ratio (Figure 3.17−3.18), are very low in JJA and annually since the majority of the available energy is being used for the latent heat flux.

Of the 6 models studied here, ERA15 shows the best agreement with observations for the latent heat flux (Sheppard et al., 2000 and Section 3.3). The latent heat flux (Figures 3.10−3.12) is slightly higher than that in ECHAM4 and HadAM2b
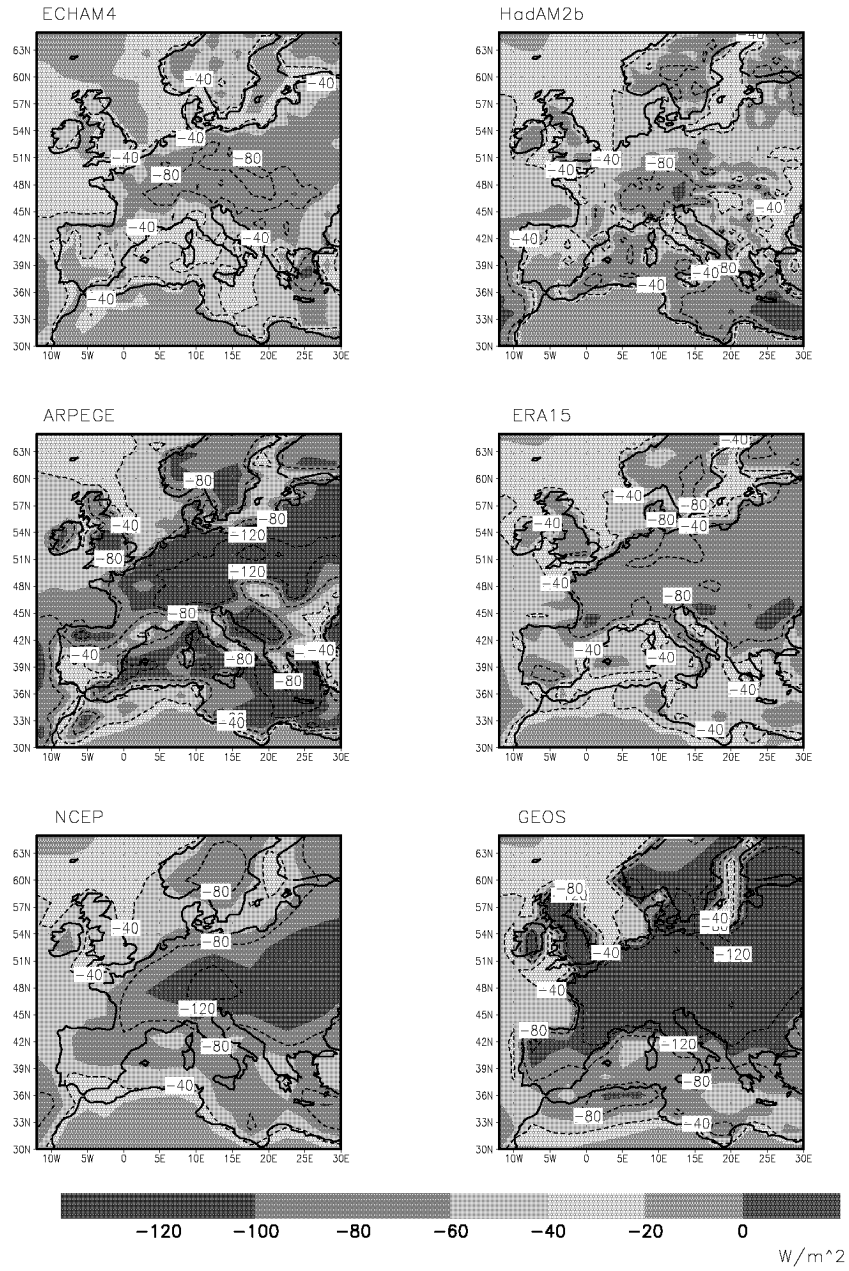
Figure 3.11: The latent heat flux over Europe for June-July-August. Units are in W m^{-2}.

in JJA and slightly lower than these models in DJF. This is largely due to the reasonable solar radiation (Figure 3.19−3.21), which is similar to that in ECHAM4 and is in good agreement with observations (Wild, 2000). Further, soil moisture (not shown) is sufficiently available since it is climatologically prescribed at the lowermost soil level (Gibson et al., 1997). Consequently, ERA15 has sufficient moisture to

Figure 3.12: The annual latent heat flux over Europe. Units are in W m^{-2}.

maintain a high evaporation throughout summer. Further, the sensible heat flux (Figure 3.13−3.15) is slightly higher than ECHAM4 since ERA15 has slightly more available energy.

The radiation in NCEP (Figure 3.19−3.21), as with the majority of the models studied here, is too high (cf. Wild, 2000). However, unlike ECHAM4 and HadAM2b,
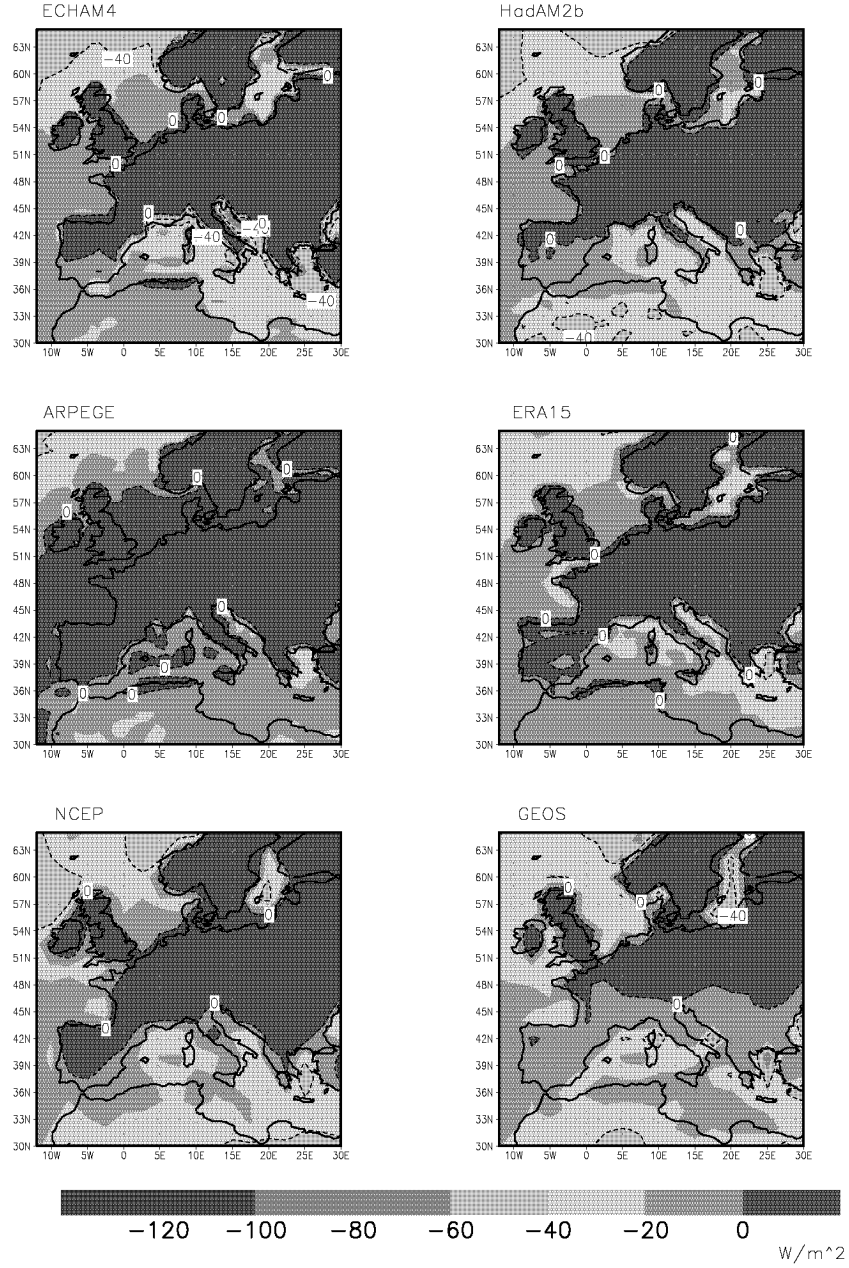
Figure 3.13: The sensible heat flux over Europe for December-January-February. Units are in W m^{-2}.

the soil moisture (Figure 3.22) is quite high since it is relaxed to a climatology with a 60-day timescale. Therefore, in JJA, the latent heat flux (Figure 3.11) is also high since there is no summer limiting of soil moisture. The sensible heat flux (Figure 3.13–3.15) is high, especially in JJA, when compared to other models due to a high net radiation (not shown), thus this leads to an intermediate value for the

89
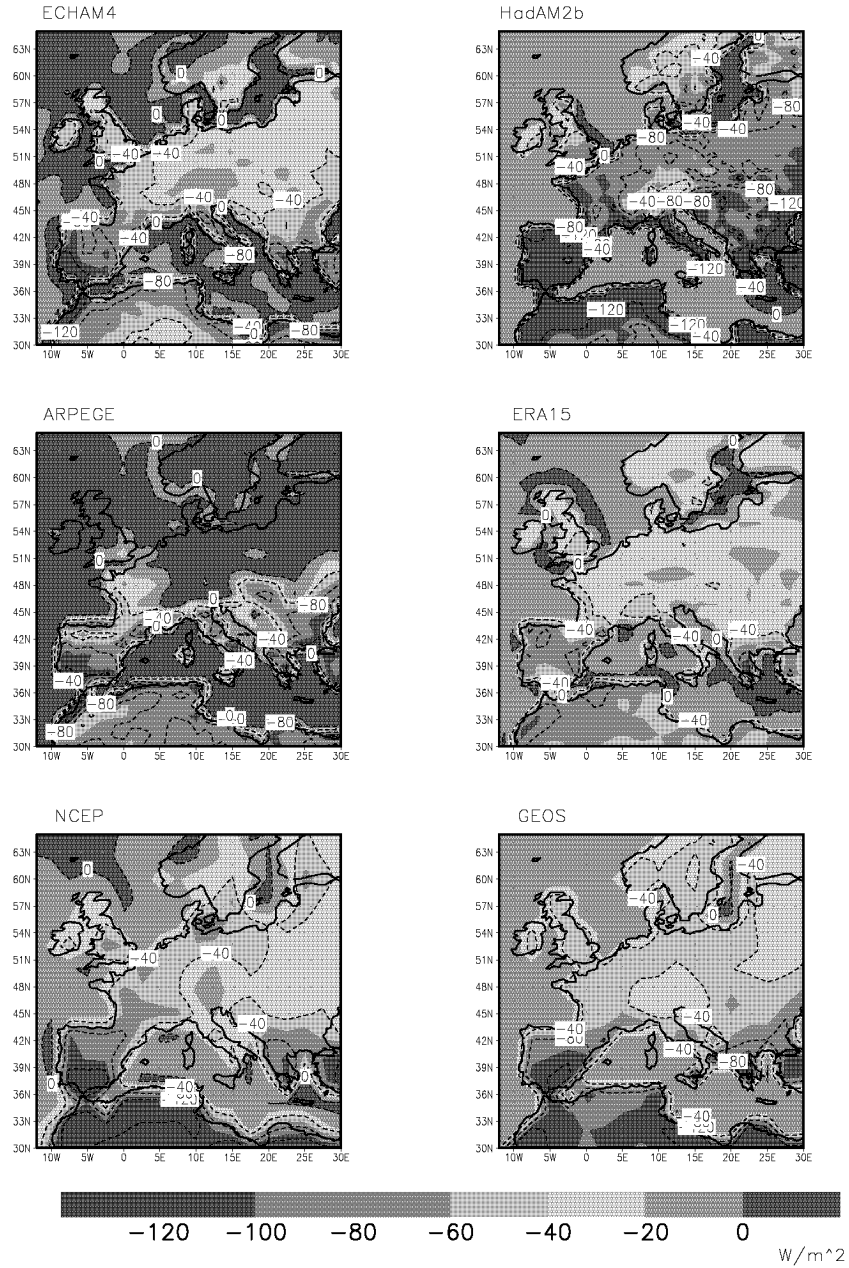
Figure 3.14: The sensible heat flux over Europe for June-July-August. Units are in W m^{-2}.

Bowen Ratio (Figure 3.16−3.18).

GEOS displays an exceptionally high latent heat flux in JJA, while it is comparable to the other models in DJF (Figure 3.10−3.12). This can be attributed to a comparatively high soil moisture (Figure 3.22), no vegetation control over total evaporation (cf. Section 2.3), and an exceptionally high solar radiation (Fig-

Figure 3.15: The annual sensible heat flux over Europe. Units are in W m^{-2}.

ure 3.19–3.21). On the contrary, the sensible heat flux (Figure 3.13–3.15) is quite high since the ground is too warm in GEOS (Molod, *pers. comm.*).
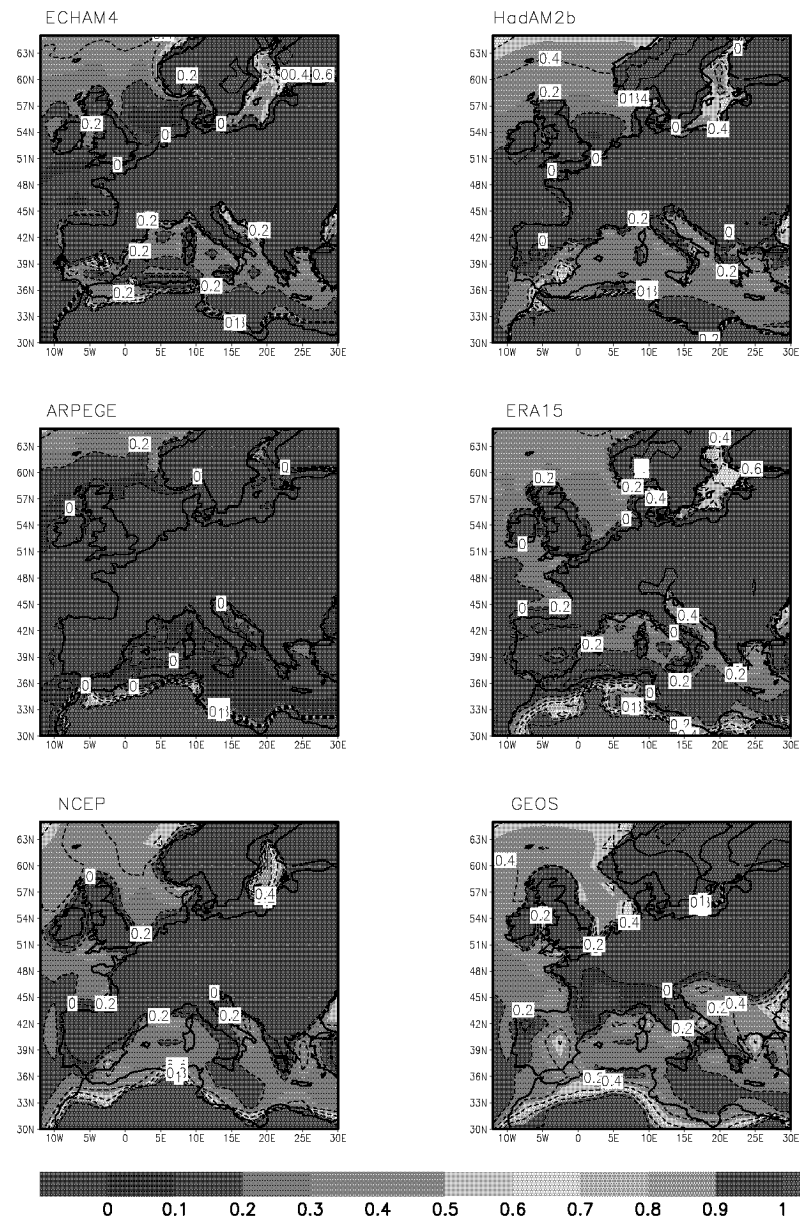
Figure 3.16: The Bowen Ratio over Europe for December-January-February.
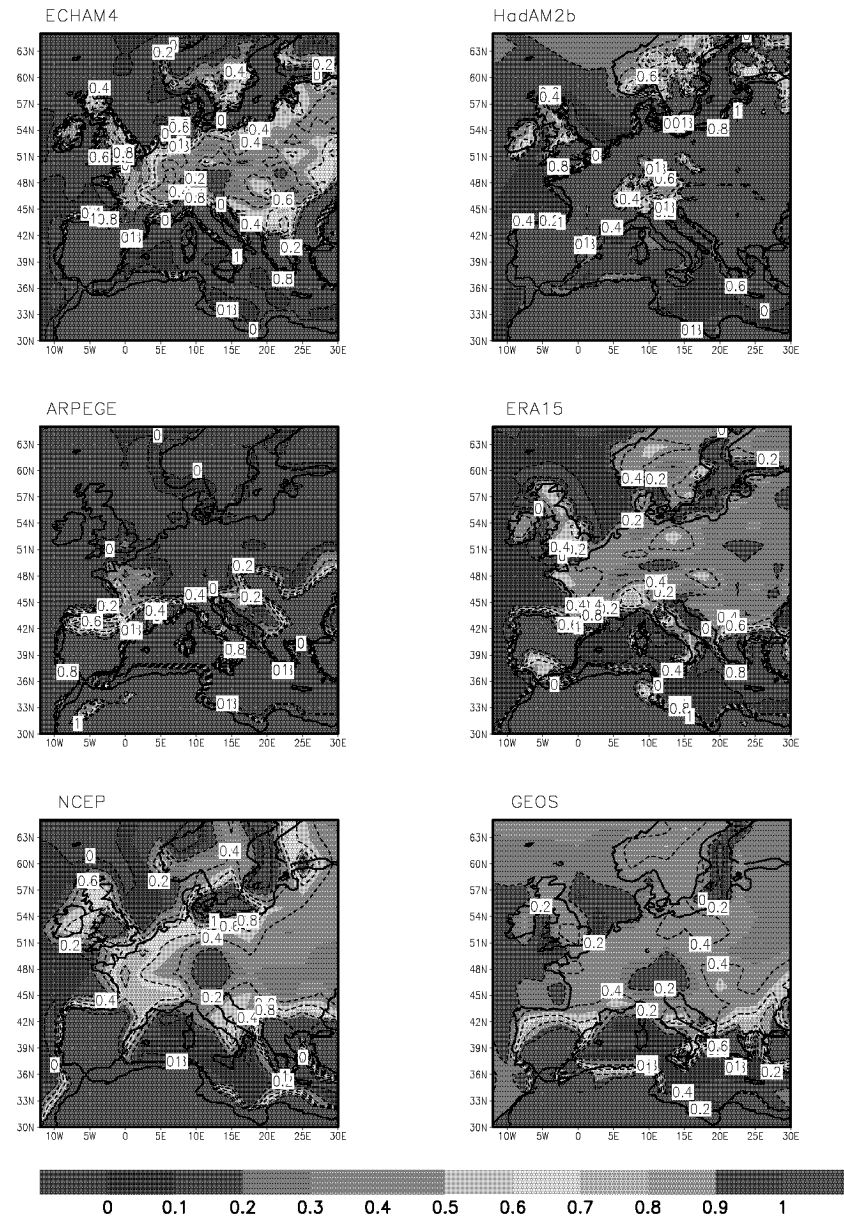
Figure 3.17: The Bowen Ratio over Europe for June-July-August.

93

Figure 3.18: The annual Bowen Ratio over Europe.
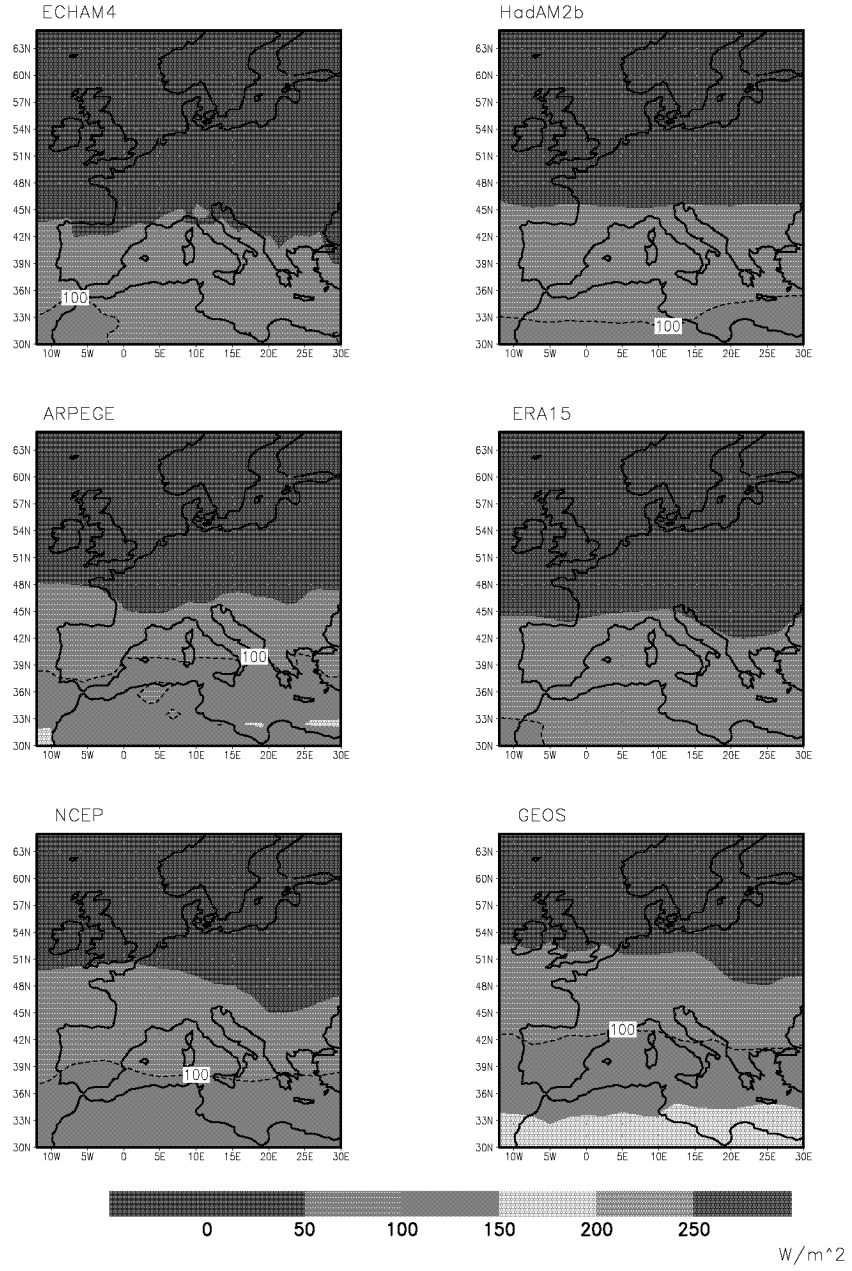
Figure 3.19: The solar radiation over Europe for December-January-February. Units are in W m^{-2}.
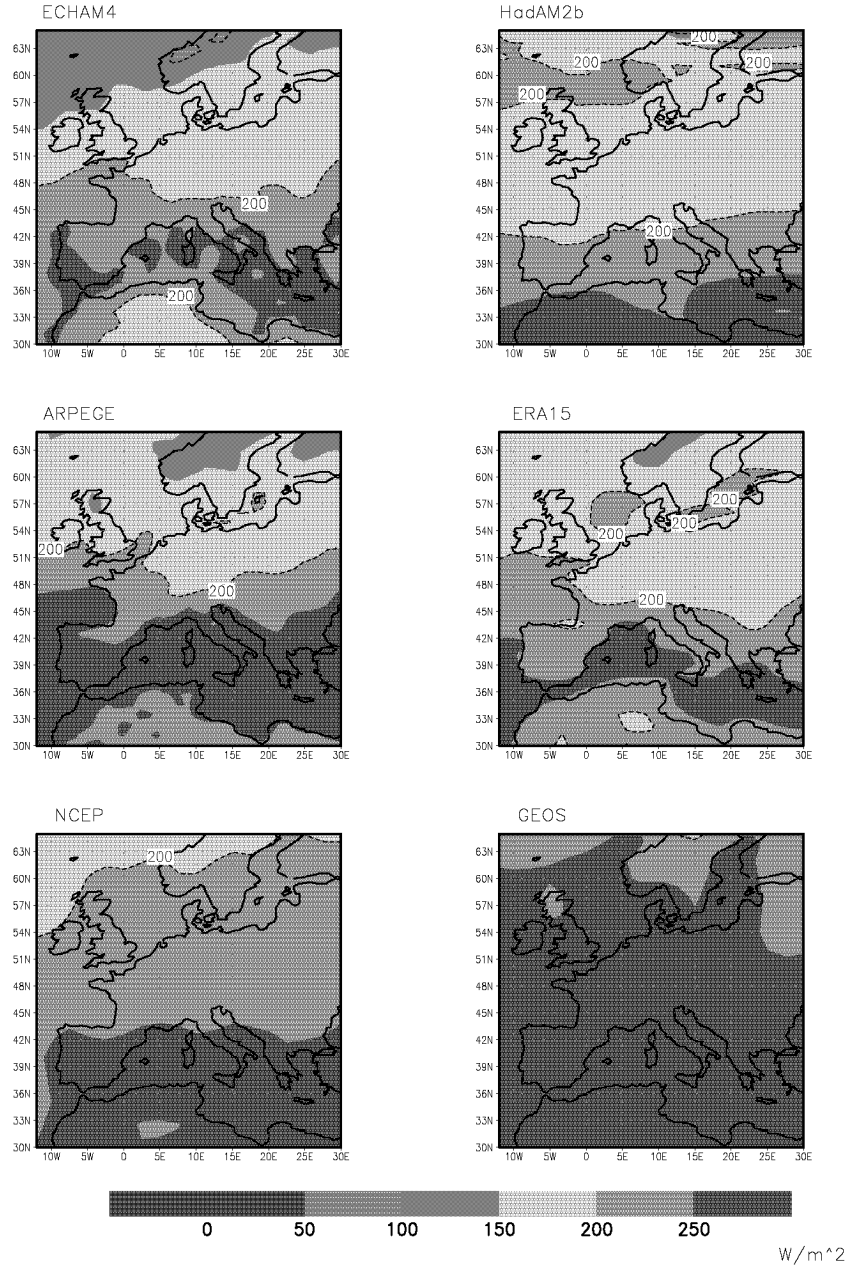
Figure 3.20: The solar radiation over Europe for June-July-August. Units are in W m^{-2}.

Figure 3.21: The annual solar radiation over Europe. Units are in W m^{-2}.
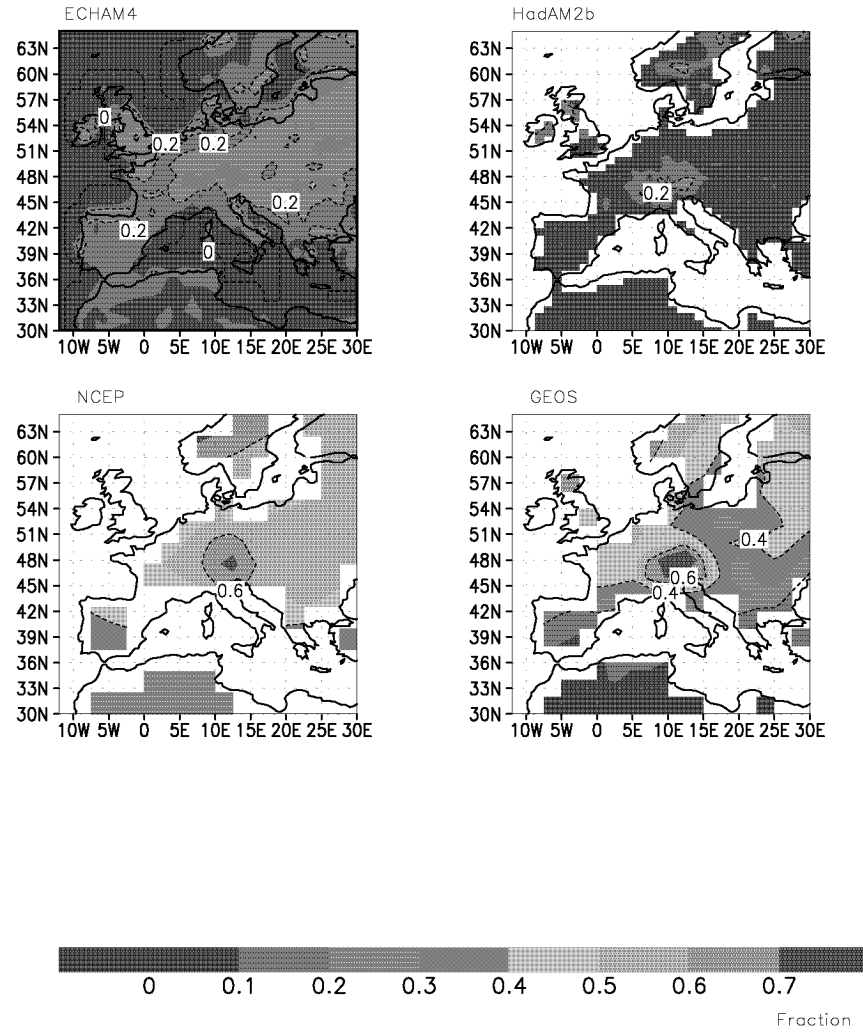
Figure 3.22: The soil moisture fraction over Europe for June-July-August. The ARPEGE and ERA15 soil moistures were not available for this study. Units are in fractions of field capacity.

3.2.5 Summary of Analysis of Models

The six models used in this study show large differences in the sensible and latent heat fluxes on a global, zonal, as well as regional, basis. In particular, ECHAM4 shows relatively low values of latent heat flux over land, which is attributable to the low net radiation. As mentioned, the net radiation in ECHAM4 compares well with observations (this will also be discussed in Section 3.3), giving confidence in this model. Similarly, ERA15 has relatively low net radiation and is considered one of the more accurate models analysed in this study. The largest problems appear to be due to a too intense zonal flow (ARPEGE), excessive summer drying (HadAM2b), high net radiation (GEOS, NCEP and ARPEGE) and the lack of vegetation control (GEOS).

3.3 Analysis of Models Versus Observations

3.3.1 Introduction

This section will compare the models used in this study to observations. Firstly, all six models will be compared to the measurements of sensible and latent heat flux obtained from the GEBA database, Swampy Summit, New Zealand and Cabauw, The Netherlands. Following this, an analysis of the parameterisations in the ECHAM4 GCM will be compared to measurements of sensible heat flux and momentum flux determined from MRI. While ECHAM4 does compare well to observations, the latter section shows some significant differences.

3.3.2 Monthly Means of Models Compared to Point Observations

To compare the models to point observations, up to 4 surrounding land points were weighted with the reciprocal of the distance between model points and observation points to provide the simulated turbulent flux for the exact location. Ocean grid points were excluded for this study. The representativity of weighted grid points has been successfully researched at both Cabauw, The Netherlands and Rietholzbach, Switzerland (Cabauw: Beljaars et al., 1983; Beljaars and Bosveld, 1997; Beljaars and Holtslag, 1991; Rietholzbach: Fürholz, 1994; Wild et al., 1996). While no such studies have been completed for the remaining sites, the orography and albedo present at each measurement site is comparable to that found in the weighted grid point used in this study (except at Hartheim, which will be discussed later), thus increasing the representativity of each site.

Figure 3.23 shows the latent heat flux for the 6 observational sites compared to the 3 GCMs. Positive fluxes are directed down. For the GCMs, the latent heat flux shows a characteristic maximum in the summer months, similarly to observed. However, it is obvious that the magnitude is quite different between models.
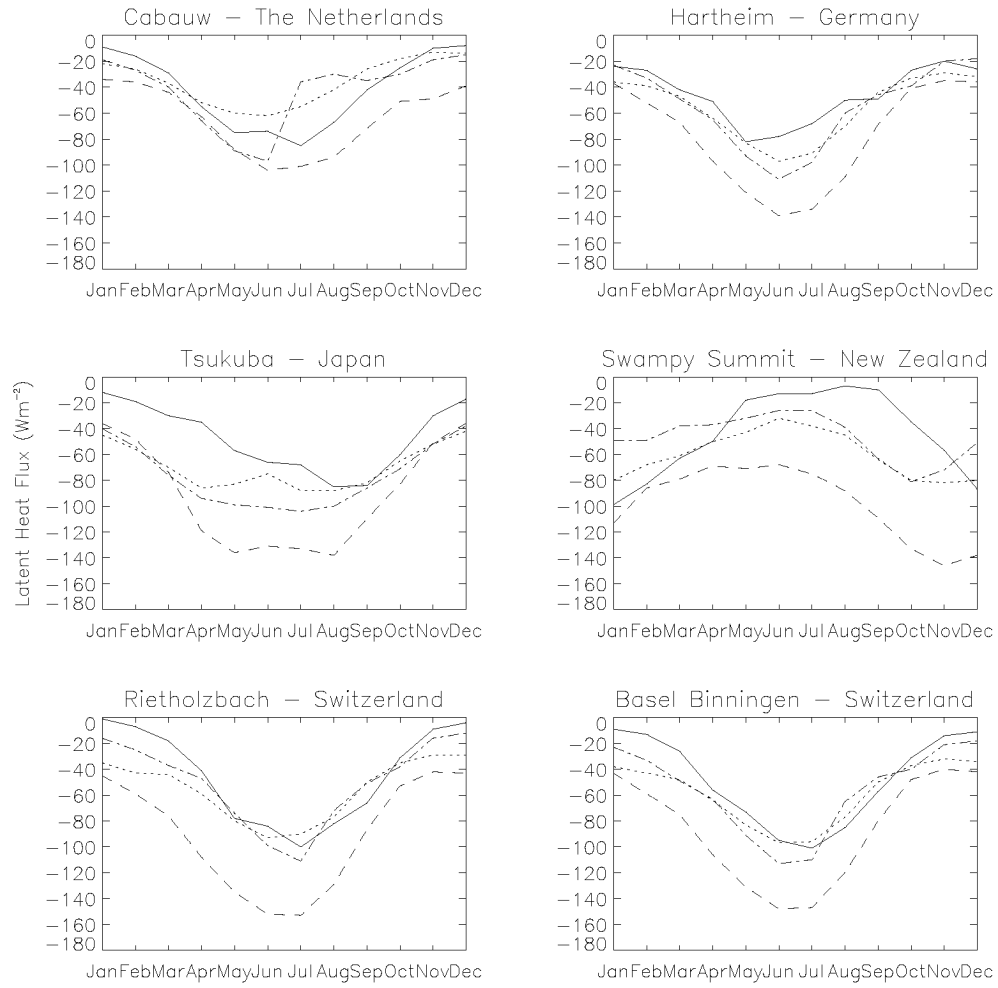
Figure 3.23: The latent heat flux from the GCMs compared to surface observations for 6 land points. The solid black line is the observations; the dotted line is ECHAM4; the dash-dot line is HadAM2b; and the dashed line is ARPEGE. Units in W m^{-2}.

Typically, ECHAM4 shows the lowest latent heat flux, although they are in line with observations in summer (Figure 3.23). ECHAM4 profits from an accurate calculation of insolation in the summer months (Wild et al., 1996). In winter, the latent heat flux is typically too high. This is due to several factors. Namely: The winter advection (which comes from the ocean) in ECHAM4 is too high which increases both windspeed and the warm air advection and, therefore, evaporation (Wild et al., 1996); the assumption that the roughness lengths of heat and momentum are equal, which tends to overestimate the roughness length for heat (Beljaars and Viterbo, 1994), and; the lack of soil freezing in winter, which enables evaporation to continue even though the ground is frozen in obervations (Betts et al., 2001). The sensible heat flux in ECHAM4 typically shows good agreement with observations, except at Hartheim, Germany where it is much lower (Figure 3.24). At the sites of Cabauw, The Netherlands and ERC, Tsukuba, Japan, the ECHAM4 net radiation (Figure 3.25) is in good agreement with observations, leading to a good agreement of sensible heat flux. However, at Hartheim, the modelled net radiation is lower than observations due to a higher modelled albedo since the pine forest at this site is not represented in the models. This leads to a lower sensible heat flux. This can also be seen in the Bowen Ratio in Figure 3.26. Of the sites used in this study, only the sites at Cabauw, Hartheim and ERC, Tsukuba had long-term measurements of both sensible and latent heat flux, allowing for the computation of the Bowen Ratio. For ECHAM4, the Bowen Ratio is close to observed at Cabauw and ERC, Tsukuba, although the low simulated sensible heat at Hartheim produces a low Bowen Ratio.

HadAM2b has very distinct characteristics in the summer months with a sharp drop in the latent heat flux in June-July for the Northern Hemisphere and October for the New Zealand site (Figure 3.23). This is due to an excessive insolation and a limitation in the soil moisture. In early summer, the excessive net radiation (Figure 3.25) causes excessive evaporation. However, HadAM2b rapidly becomes water limited, restricting the evaporation for the remainder of the season. This dramatic change is also seen in the sensible heat flux (Figure 3.24) and the Bowen Ratio (Figure 3.26). As the latent heat flux in late summer becomes restricted by limited soil moisture availability, the sensible heat flux correspondingly increases to maintain the energy balance. Consequently, the Bowen Ratio peaks towards the end of summer.

The latent heat flux in ARPEGE is exceptionally high compared to observations (Figure 3.23). This is primarily due to the model exhibiting a too intense zonal flow throughout the year, which produces an excessive moist advection, thereby increasing precipitation and evaporation (Doblas-Reyes et al., 1998). Additionally, while the incoming shortwave radiation in ARPEGE is high when compared to observations (cf. Wild and Ohmura, 1999) which further increases the evaporation, the net radiation is only slightly higher than observed (Figure 3.25). Thus, the sensible heat flux (Figure 3.24) is low when compared to observations in order to maintain the energy balance, leading to a low Bowen Ratio (Figure 3.26).

Figure 3.27 shows the latent heat flux for the 3 Reanalysis models. As with the GCMs, there is considerable spread throughout the year, although the general trend follows observations.

Of the 6 models discussed here, ERA15 shows the closest latent heat flux when

Figure 3.24: The sensible heat flux from the GCMs compared to surface observations for 6 land points. The solid black line is the observations; the dotted line is ECHAM4; the dash-dot line is HadAM2b; and the dashed line is ARPEGE. Units in W m^{-2}.

Figure 3.25: The net radiation from the GCMs compared to surface observations for 3 land points. The solid black line is the observations; the dotted line is ECHAM4; the dash-dot line is HadAM2b; and the dashed line is ARPEGE. Units in W m^{-2}.

Figure 3.26: The Bowen Ratio from the GCMs compared to surface observations for 3 land points. The solid black line is the observations; the dotted line is ECHAM4; the dash-dot line is HadAM2b; and the dashed line is ARPEGE.

Figure 3.27: The latent heat flux from the Reanalyses compared to surface observations for 6 land points. The solid black line is the observations; the dotted line is ERA15; the dashed line is NCEP; and the dash-dot line is GEOS. Units in W m^{-2}.

compared to observations (Figure 3.27). In particular, the latent heat flux in the two Swiss sites and Cabauw are very well represented. The sensible heat flux for ERA15 is also comparable to observations, except at Hartheim (Figure 3.28). Figure 3.29 shows the net radiation in ERA15 compared to observations. As can be seen, the net radiation determined by ERA15 at Cabauw and ERC, Tsukuba is the closest of all models to observations. This can also be seen in the Bowen Ratio (Figure 3.30). At Cabauw and ERC, Tsukuba, the Bowen Ratio is similar to observed, while the low sensible heat flux calculated at Hartheim leads to a low Bowen Ratio. As mentioned for ECHAM4, the low values of modelled sensible heat flux at Hartheim are due to the pine forest being unrepresented in the models. For the other sites, considering that both ECHAM4 and ERA15 are based on a similar model, the greater accuracy of ERA15 compared to ECHAM4 shows that the turbulent fluxes in the Reanalyses are improved when compared to the GCMs.

Figure 3.28: The sensible heat flux from the Reanalyses compared to surface observations for 6 land points. The solid black line is the observations; the dotted line is ERA15; the dashed line is NCEP; and the dash-dot line is GEOS. Units in W m^{-2}.

The latent heat flux in NCEP is typically higher than observations (Figure 3.27). A major factor contributing to this is an excessive incoming solar radiation, which

106

Figure 3.29: The net radiation from the Reanalyses compared to surface observations for 3 land points. The solid black line is the observations; the dotted line is ERA15; the dashed line is NCEP; and the dash-dot line is GEOS. Units in W m^{-2}.
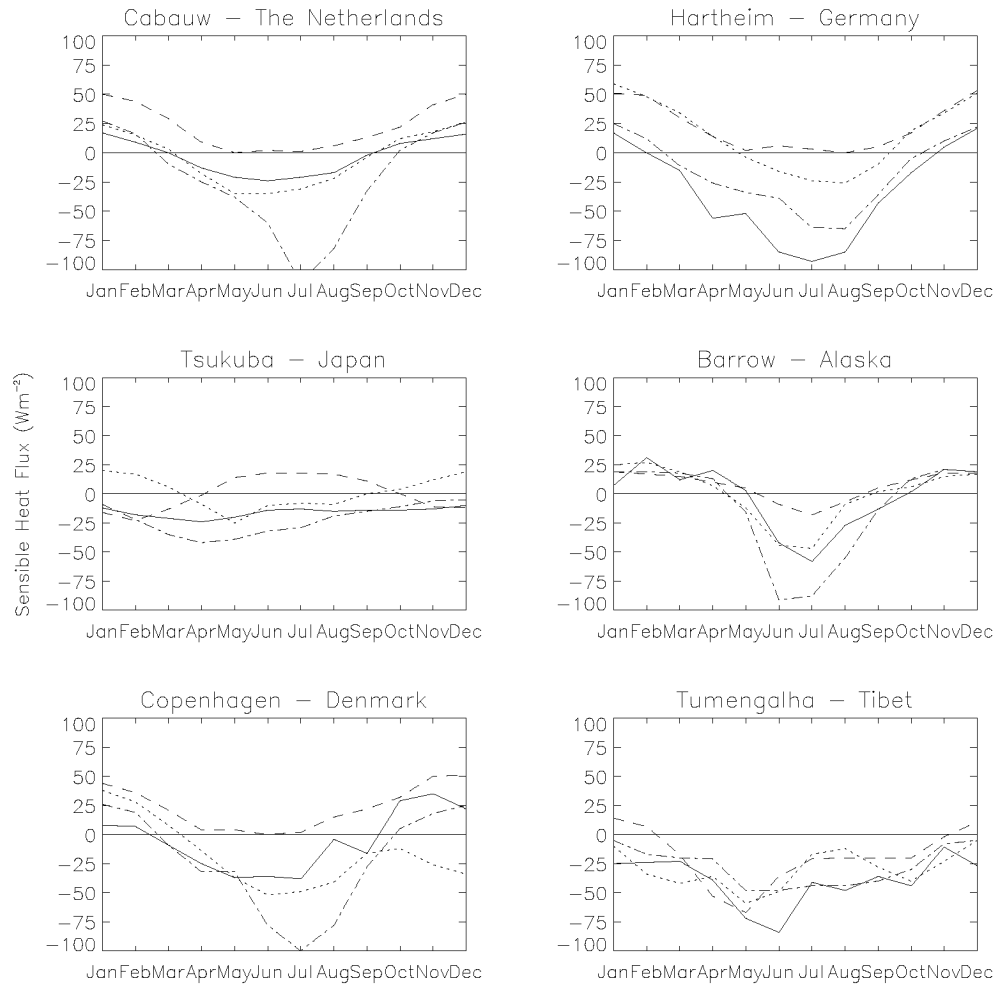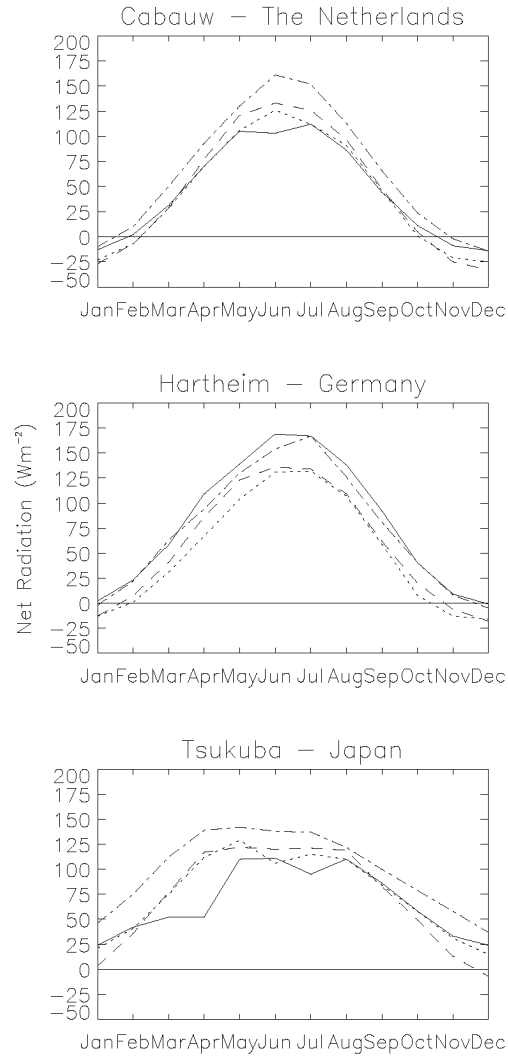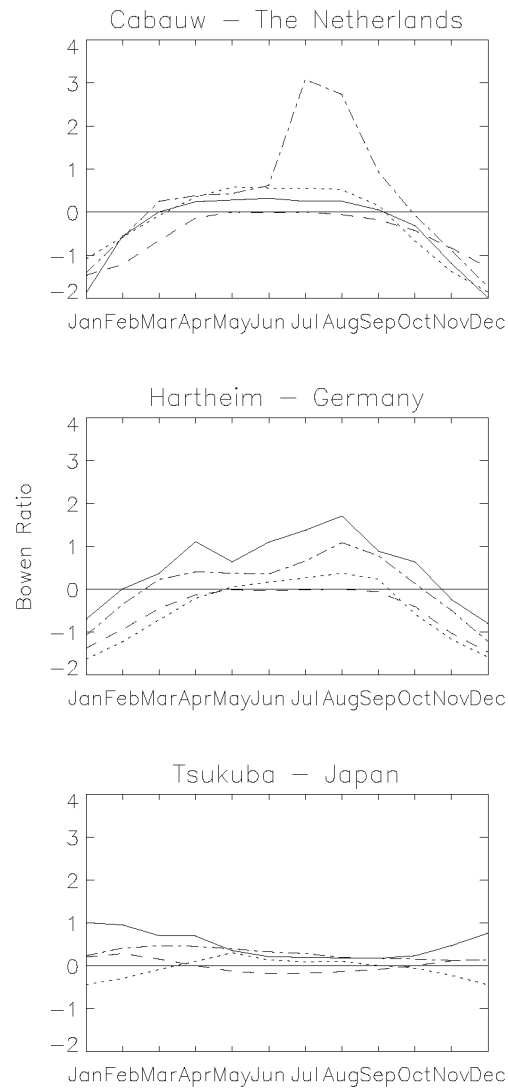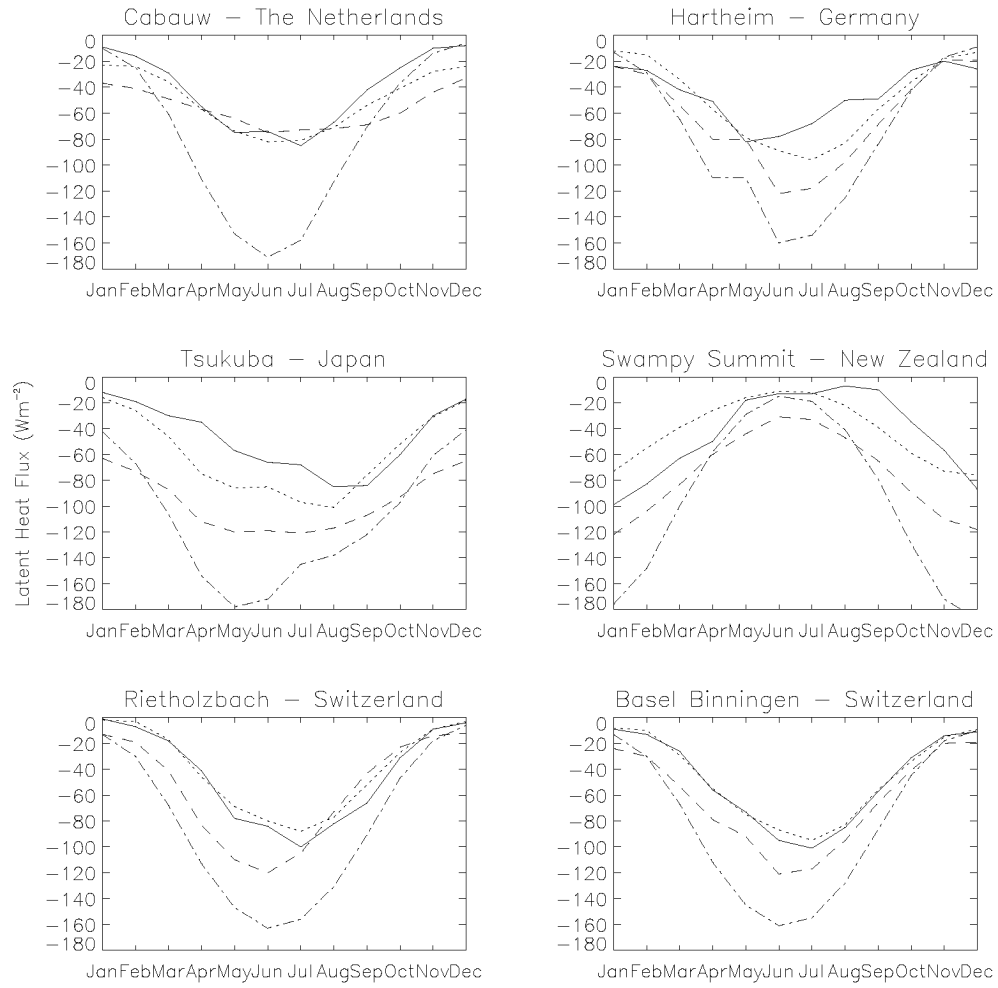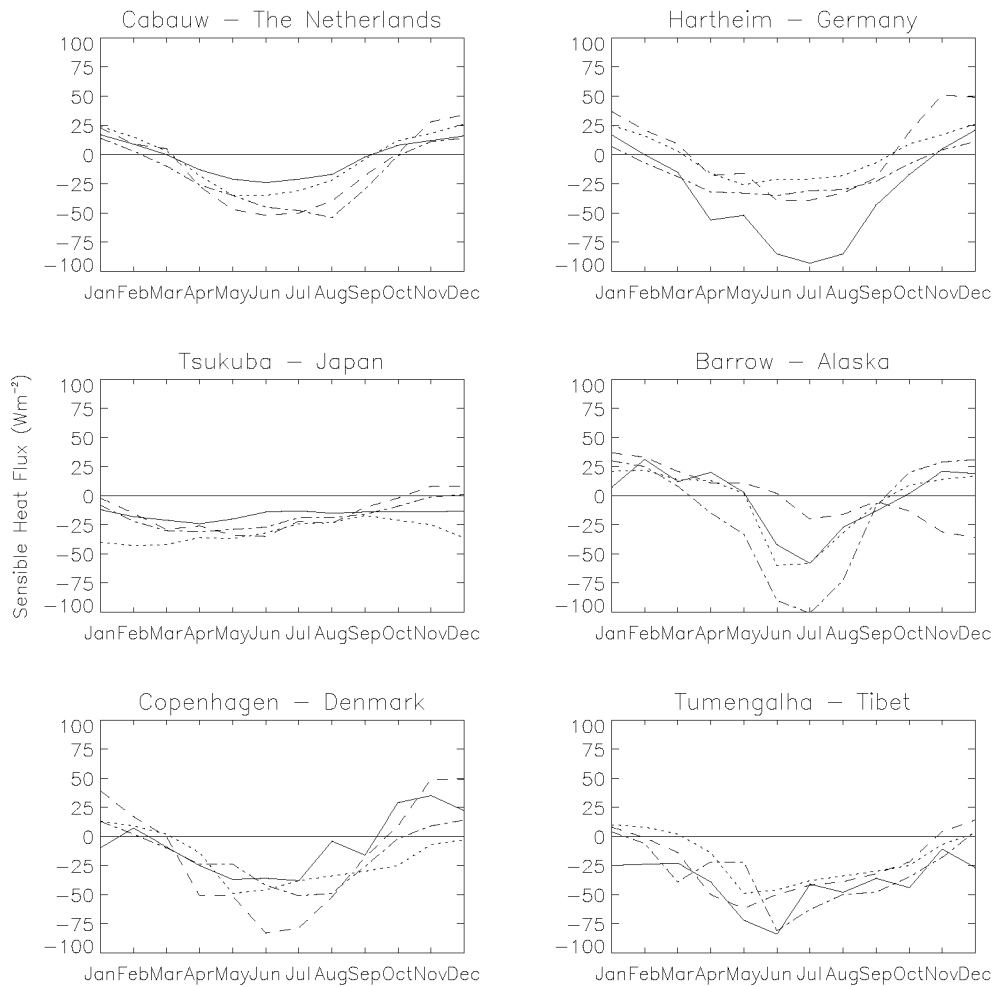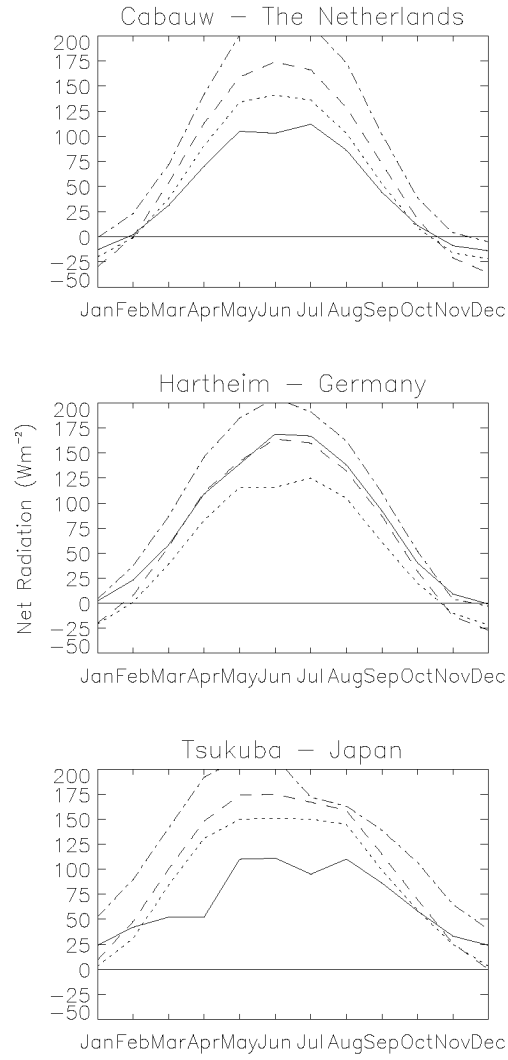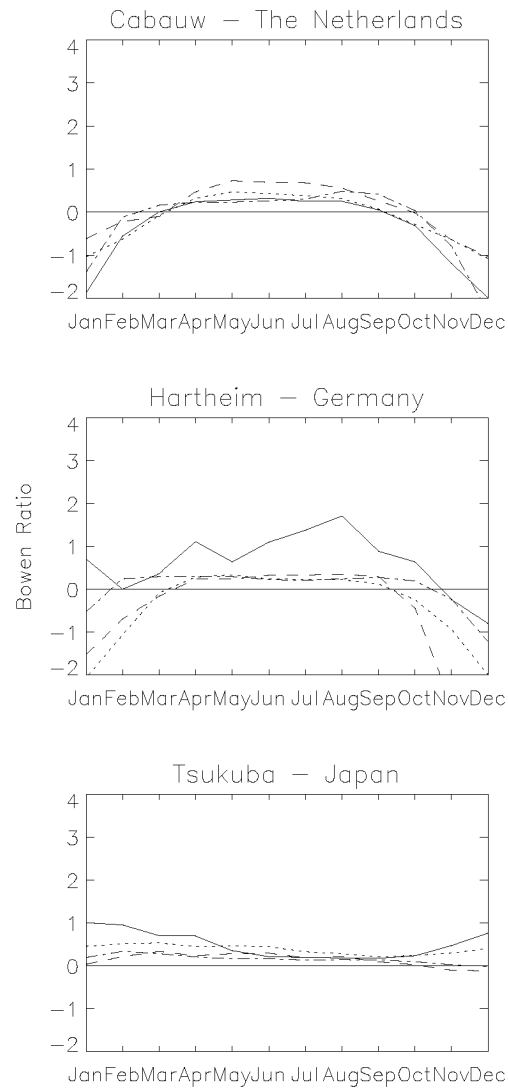
107

Figure 3.30: The Bowen Ratio from the Reanalyses compared to surface observations for 3 land points. The solid black line is the observations; the dotted line is ERA15; the dashed line is NCEP; and the dash-dot line is GEOS.

increases the evaporation. This can also be seen in the excessive net radiation in NCEP (Figure 3.29). Contrarily to HadAM2b, NCEP has sufficient soil moisture throught the year (not shown). Thus, the high radiation leads to high evaporation. The sensible heat flux in NCEP differs from observations with values slightly lower than observed at some sites (Barrow and Hartheim) and slightly higher than observed at others (Cabauw and Copenhagen; Figure 3.28). Therefore, the Bowen Ratio is quite similar to observations (Figure 3.30). However, since the sensible heat flux at Hartheim is low, the Bowen Ratio is also lower than observed.

Lastly, the latent heat flux in GEOS is exceptionally high when compared to observations (Figure 3.27). This is largely due to exceptionally high incoming solar radiation and a large soil moisture availability. Thus, GEOS is never water limited. The sensible heat flux is also quite high (Figure 3.28). Since the net radiation is exceptionally high (Figure 3.29) in GEOS, there is ample energy available to partition into both latent and sensible heat fluxes, leading to high values in both the turbulent fluxes. As both sensible and latent heat fluxes are too high, the Bowen Ratio appears comparable to observations, except at Hartheim, as discussed above (Figure 3.30).

3.3.3   Comparison of Tower Data to ECHAM4

Figure 3.31 shows the momentum flux as determined from the sonic (M_{sonic}) compared to the ECHAM4 parameterisations (M_{ECHAM}) for the 25 m level at the MRI site for May 1997. Figure 3.31a shows the momentum flux as directly determined from the ECHAM4 GCM parameterisation using the 25 m level and the surface. In this plot, it is obvious that, while there is a small agreement with the sonic momentum flux, ECHAM4 typically underestimates the momentum flux for small values, and overestimates the flux for large values. This may be due to a variety of reasons. For example, the equations to determine the fluxes in ECHAM4 (Equations 2.53 and 2.54) add the value "1" to the ratio z_l/z_0 for the sole purpose of guaranteeing against a zero denominator. Thus, this addition of "1" is purely a numerical convenience with no physical substance. However, it is obvious from Figure 3.31b that removing this "+1" has little affect on the momentum flux. Another possibility is that, for all models studied here, $z_{0h} = z_0$. As mentioned in Section 2.2.5, it is difficult to define z_{0h} due to the inability to define the surface temperature. As an estimate, the value of z_{0h} (5×10^{-4} m) from Section 2.2.5 has been added to the parameterisations used in ECHAM4, with all other equations remaining the same (Figure 3.31c). It is evident that the momentum flux from the model does change from the original parameterisations (Figure 3.31a), although the results are still significantly different from the sonic momentum flux. One improvement to the adoption of z_{0h} is that the trend of momentum flux now follows the trend from the sonic, even though the magnitudes are different. It is possible that the use of a different value of z_{0h} would rectify this disagreement, but it remains difficult to determine an exact value for z_{0h}. The third alternative (Figure 3.31d) eliminates this problem. Instead of using the roughness length, the momentum flux is determined using two atmospheric levels. For the previous three plots, the 25 m level and surface values were used. The fourth plot uses the 10 m and 25 m levels, with the sonic data interpolated to a correspond-

ing level. As can be seen from this plot, there is a much better agreement between the sonic momentum flux and ECHAM4. This method prevents the calculation of large wind gradients (since u at z_0 is 0), and means that the surface temperature need not be defined for either the determination of Ri or z_{0h}. The values in each "bin" may be different in the four plots due to two reasons: Plots a, b and c use surface data whereas plot d uses the 10 m level data, and; the different formulations suggested here regroup the values into different "bins".
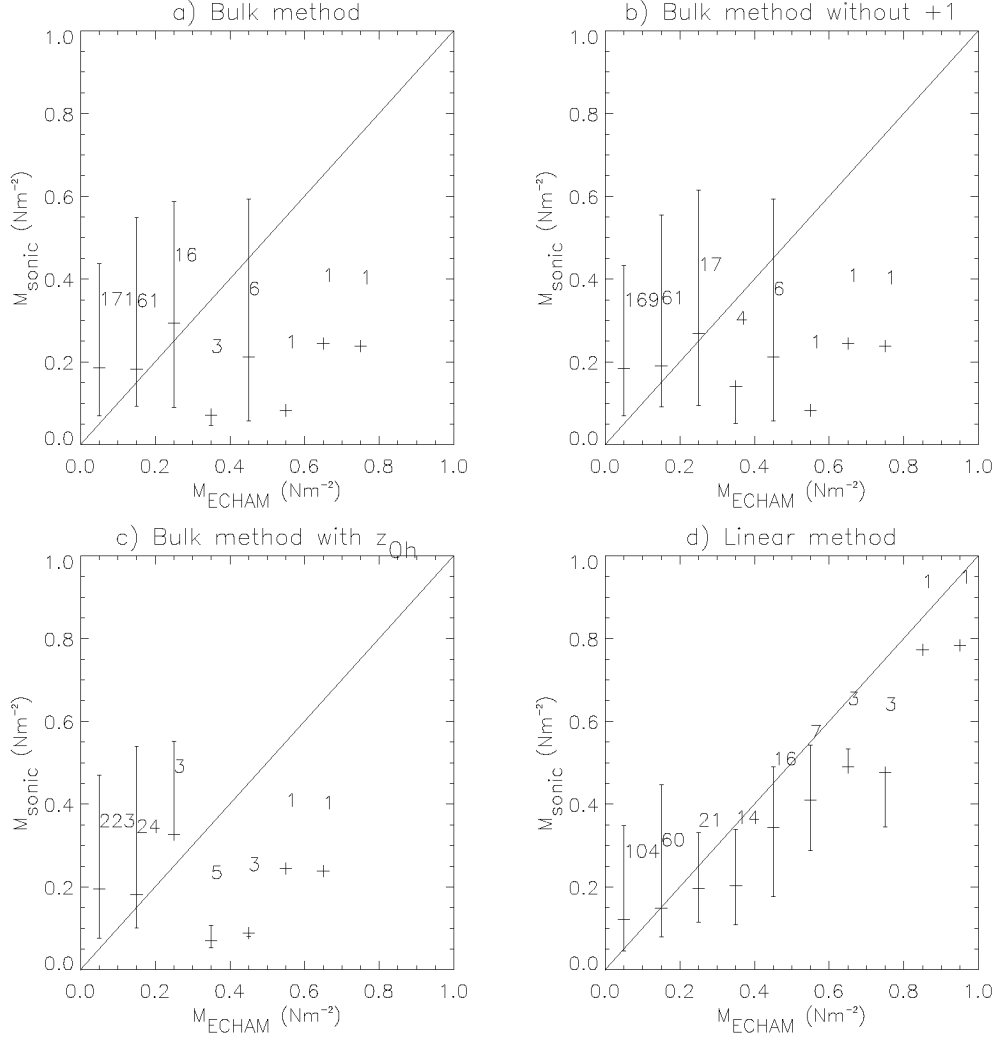
Figure 3.31: Half hourly mean sonic momemtum flux (M_{sonic}) compared to the momentum flux from ECHAM4 (M_{ECHAM}) for the 25 m level at MRI for May 1997. (a) Uses the parameterisations directly from ECHAM4, (b) uses the parameterisation from ECHAM4 but removes the value "+1" from Equations 2.53 and 2.54, (c) uses the ECHAM4 parameterisation but incorporates the value of z_{0h} obtained from Section 2.2.5, and (d) incorporates the previous two changes and uses two levels rather than 1 level and the surface. The bars show the standard deviation. The numbers above the bars show the number of occurrences in each "bin". Units in N m^{-2}.

A similar result can be seen in Figure 3.32. This figure is equivalent to that above, but for the sensible heat flux. As with the figure for momentum flux, the sensible

heat flux determined with ECHAM4 show large differences when compared to sonic measurements, particularly for large values of sensible heat flux (Figure 3.32a). Removing the case of "+1" (Figure 3.32b) does little to correct the values, although this is a more theoretically correct determination of the fluxes. Figure 3.32c shows the ECHAM4 parameterisations with the addition of z_{0h}. As with the momentum flux, a slight improvement is seen, although it remains difficult to quantify the exact value of the roughness length for heat. Figure 3.32d shows by far the best agreement when compared to the sonic. This plot uses two atmospheric levels rather than one level and the surface. The ability to compute the fluxes without the use of the roughness lengths is a clear advantage over the current parameterisations since there is no need to define the surface temperature. As for the previous figure, values in each "bin" may change.

Figure 3.33 shows the Ri determined from R_f (Equation 2.29) using the sonics (Ri_{sonic}) compared to the Bulk Richardson Number determined from ECHAM4 (Ri_{ECHAM}) for the 25 m level at MRI for May 1997. In this figure, it is apparent that using two levels (Figure 3.33b) is superior over using one level and the surface (Figure 3.33a) when compared to the sonic measurements. The bulk formulation in ECHAM4 shows little or no agreement to the sonic. This is mainly because the use of one level and the surface produces large temperature gradients which lead to large values of Ri when using bulk parameterisations. As mentioned previously, Beljaars and Holtslag (1991) found that the difference in temperature at z_0 and the surface may be as large as 6 K, implying that the temperature gradients determined using surface values may be significantly different than that obtained through using two atmospheric levels. At MRI, the temperature gradient between the 25 m level and the surface may reach up to 15 K. This requires further discussion.

If it is assumed that the lapse rate is approximately $10^o C/$ km, the temperature gradient between the atmosphere just above the surface and the 25 m level would be approximately $0.25^o C/$ 25 m. However, as mentioned, the true gradient can reach up to 15 K over the same height difference, a value 60 times larger than the lapse rate. For windspeed, the difference is not as significant. The calculation of Ri uses the square of the wind shear. When using the 25 m level and the surface, this squared value averages 7 for May 1997, when using two atmospheric levels (10 m and 25 m), it averages 0.7, a value 10 times smaller. Thus, in cases where the temperature gradient is large, this dominates the calculation of Ri. This leads to exceptional large values of Ri_{ECHAM} when compared to Ri_{sonic}. The obvious solution would be to include another atmospheric level for the computation of the surface fluxes to reduce problems of using surface characteristics. The idea would be to introduce a new level which is only used for the determination of the fluxes. This new level (at, say 2 m or 10 m where temperature and windspeed, respectively are currently available) would require surface information, but would then be used as the atmospheric surface level to determine the fluxes at 33 m (for ECHAM4). Indirectly, the 33 m level would still be affected by the surface (through this lower level), but to a much lesser degree than using surface information directly. One immediate problem associated with this solution is the introduction of more levels, which would require a smaller timestep and a smaller horizontal resolution leading to the need of more computational time. Secondly, the use of more levels in the lower boundary layer could lead to very small
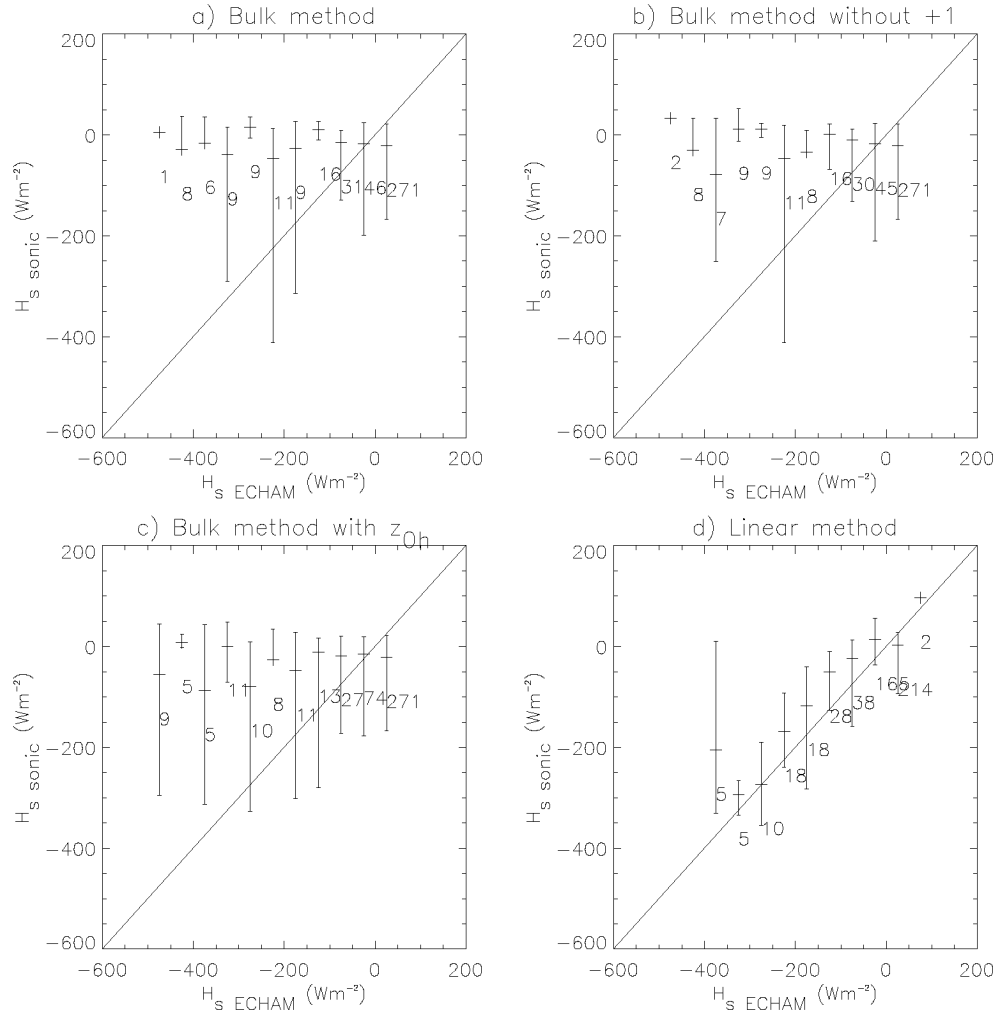
Figure 3.32: Half hourly mean sonic sensible heat flux ($H_{s\,sonic}$) compared to the sensible heat flux from ECHAM4 ($H_{s\,ECHAM}$). (a) Uses the parameterisations directly from ECHAM4, (b) uses the parameterisation from ECHAM4 but removes the value "+1" from Equations 2.53 and 2.54, (c) uses the ECHAM4 parameterisation but incorporates the value of z_{0h} obtained from Section 2.2.5, and (d) incorporates the previous two changes and uses two levels rather than 1 level and the surface. The bars show the standard deviation. The numbers above the bars show the number of occurrences in each "bin". Units in W m^{-2}.

gradients of windspeed or temperature, making it impossible to determine Ri.

Another solution would be to adopt another method rather than relying on Monin-Obukhov theory. Zilitinkevich and Calanca (2000) state that Monin-Obukhov theory has the disadvantage that it does not include possible effects from the plantery boundary layer's large features on the constant flux layer. Further, Monin-Obukhov theory was determined for close to neutral conditions, while it may not neccesarily describe the constant flux layer in strong convection or strong static stability (Zilitinkevich and Calanca, 2000). Instead, Zilitinkevich and Calanca (2000) suggest the use of the Brunt-Väisälä frequency. While this method has been proven not to work in ECHAM4 (Larsen et al., 2001), it does suggest that other methods may be used to replace Monin-Obukhov theory in the models.

A final possible solution would be to incorporate the atmospheric physics into a layer that is close to the surface to calculate the atmospheric surface fluxes. This has similar benefits to adding levels at 2 m or 10 m, but reduces the possibility of small gradients of windspeed or temperature, as well as better representing the surface. Further, it would not require a smaller timestep to compensate for the addition of atmospheric levels. However, the addition of this new layer would also increase the computational requirements since the physics between this level and the surface would need to be incorporated.
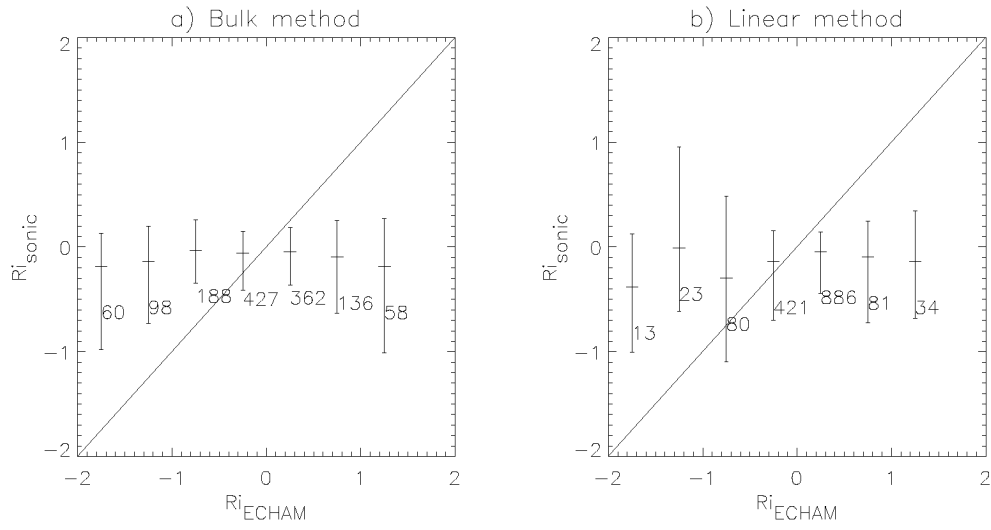
Figure 3.33: Half hour mean Gradient Richardson Number from the sonic (Ri_{sonic}) compared to the Richardson Number from ECHAM4 (Ri_{ECHAM}). (a) Uses the parameterisations directly from ECHAM4, and (b) uses two levels rather than 1 level and the surface. The bars represent the standard deviation. The numbers above the bars show the number of occurrences in each "bin".

3.3.4   Summary of Analysis of Models Versus Observations

This study, as with previous studies (see, e.g., Wild, 2000 and Sheppard et al., 2000), has shown that the ECHAM4 GCM and ERA15 Reanalysis show good agreement with observations of sensible and latent heat flux, largely due to an accurate parameterisation of solar radiation. The results from ERA15 appear to be slightly better than ECHAM4 implying that the Reanalyses offer a more accurate means to determine the turbulent fluxes (since both ECHAM4 and ERA15 are based on a similar model). The other models studied here have various limitations: HadAM2b suffers from excessive summer drying; ARPEGE from excessive solar radiation and a too intense zonal flow, and; GEOS from the lack of vegetation control and a too warm surface. All these models, including ECHAM4 and ERA15, also use bulk formulations for the determination of the fluxes. A comparison of the ECHAM4 parameterisations to sonic measurements from MRI shows that there is still room for improvement in the determination of the fluxes. The addition of another atmospheric level (at, say, 2 m or 10 m), or the introduction of a close to surface layer, would remove the need for using surface data which is difficult to define.

3.4   Summary of Results

Global comparisons of the six models used in this study show that the latent heat flux over land in ECHAM4, ERA15 and NCEP is low compared to the other models, although it is inline with observations (see, e.g., Sheppard et al., 2000). This is because, for ECHAM4 and ERA15, the radiation is in good agreement with observations (Wild, 2000). The results on a local scale show that the turbulent fluxes for ERA15 are slightly closer to observations than ECHAM4 indicating that the Reanalyses are superior for the determination of the turbulent fluxes since both ECHAM4 and ERA15 are based on a similar model. For NCEP, the solar radiation is too large, leading to an overestimation of the sensible heat flux. Problems also arise in HadAM2b which exhibits an excessive solar radiation. Over land, this results in a large drying effect at the end of summer since the wilting point is reached. Over sea, a runaway evaporation leads to a very high latent heat flux. ARPEGE has an excessive solar radiation and a latent heat flux that is not water limited leaving an underestimation in the sensible heat flux. Finally, GEOS suffers from the lack of vegetation control and high radiation. These facets are also seen on a zonal and regional basis.

Finally, the six models were compared to the observations. Results show that the ECHAM4 GCM and ERA15 Reanalysis agree well with observations. However, the use of bulk formulations in the determination of the fluxes is a distinct disadvantage. ECHAM4, as with other models, would significantly benefit from an additional atmospheric layer, or the introduction of a layer close to the surface, to omit the need for using surface information.

115

Chapter 4

Conclusions

The accurate parameterisation of the turbulent fluxes in climate models is necessary to determine the hydrological cycle and energy balance, as well as to describe the state of the turbulence in the atmosphere. However, to date, relatively few studies have been completed to determine the problems and/or strengths of these parameterisations.

In order to analyse the turbulent fluxes in GCMs and Reanalyses, long term measurement data was obtained from various sources including two newly analysed sites in New Zealand and Japan. Emphasis was placed on the MRI, Tsukuba, Japan measurements since they provide a wealth of data that has not previously been analysed. Measurements from MRI were obtained for 1.5 years using sonic anemo-thermometers, propeller anemometers, Pt-100s and capacitance hygrometers. A comparison of the different measurements shows good agreement between the windspeeds and temperatures. However, for the determination of the fluxes, a number of methods were applied using the profile instruments. These show quite varying results, and often disagree with the sonic fluxes. New universal functions were developed to better reflect the inhomogeneity of the site at MRI. These equations appear to agree well with the sonic fluxes, although it is important to note that the new equations are site specific depending on the roughness elements in the area. Even at MRI, the new equations appear to describe the 25 m level well, but the 10 m level appears to be better represented by the universal functions of Högström (1996).

The six models used here include the ECHAM4 GCM, HadAM2b GCM, ARPEGE GCM, ERA15 Reanalysis, NCEP Reanalysis and GEOS Reanalysis. Each of these models determines the turbulent fluxes using the bulk transfer relation, although there are some minor differences for the determination of the drag coefficients and description of evaporation. Most notable is in GEOS which contains no vegetation control leading all evaporation to the potential rate. Of the models tested here, ECHAM4 and ERA15 show the turbulent fluxes most inline with observations, with ERA15 slightly better than ECHAM4. This indicates that the Reanalyses are a more accurate means to determine the turbulent fluxes than GCMs, since both ECHAM4 and ERA15 are based on a similar model. The ability of ECHAM4 and ERA15 to accurately determine the turbulent fluxes is due to an accurate parameterisation of the solar radiation. The excessive radiation in the other models has different effects

depending on the soil moisture availability and the partitioning into sensible heat flux. Hence, it is obvious that radiation plays a key role in determining accurate fluxes.

Although ECHAM4 shows quite good agreement when compared to observations, the use of the MRI data in this model shows a number of limitations. The use of the bulk formulations requires surface data which is difficult to define and results in overly large gradients of windspeed and, in particular, temperature. The addition of a new level at, say, 2 m or 10 m would prevent the need for surface data and has been shown to give excellent agreement to observations. Another solution would be to introduce a new layer very close to the surface, which would also omit the need for surface data.

Possible future work would be to attempt to standardise the new equations developed here for the determination of the fluxes using the profile method. At present, the new equations are dependent of the roughness of the elements influencing the 25 m level at MRI. However, it would be an obvious benefit to adapt these equations so that they are site independent for input into models. This would be a difficult undertaking, since the roughness of each site is often unique.

Bibliography

Aslyng, H. C., 1961: Evaporation and radiation heat balance at the soil surface. *Arch. Met. Geoph. Biokl.* **B10**, 359–375.

Beljaars, A. C. M. and F. C. Bosveld, 1997: Cabauw data for the validation of land surface parameterization schemes. *J. Climate* **10**, 1172–1193.

Beljaars, A. C. M. and A. A. M. Holtslag, 1991: Flux parameterization over land surfaces for atmospheric models. *J. Appl. Meteorol.* **30**, 327–341.

Beljaars, A. C. M., P. Schotanus, and T. M. Nieuwstadt, 1983: Surface layer similarity under uniform fetch conditions. *J. Clim. and Appl. Meteorol.* **22**, 1800–1810.

Beljaars, A. C. M. and P. Viterbo, 1994: The sensitivity of winter evaporation to the formulation of aerodynamic resistance in the ECMWF model. *Bound. Layer Meteorol.* **71**, 135–149.

Bendat, J. and A. Piersol, 1986: *Random data: Analysis and measurement procedures*, Chapter 4.7 Statistical independence and trend tests, pp. 407. John Wiley, Interscience.

Betts, A. K., P. Viterbo, and A. C. M. Beljaars, 1998: Comparison of the land-surface interaction in the ECMWF Reanalysis Model with the 1987 FIFE data. *Mon. Wea. Review* **126**, 186–198.

Betts, A. K., P. Viterbo, A. C. M. Beljaars, and B. van den Hurk, 2001: Impact of BOREAS on the ECMWF model. *J. G. R.* **106 (D24)**, 33593–33604.

Bloom, S. C., L. L. Takacs, A. M. da Silva, and D. Ledvina, 1996: Data assimilation using incremental analysis updates. *Mon. Wea. Review* **124**, 1256–1271.

Brinkop, S., 1992: *Parameterisierung von Grenzschichtwolken für Zirkulationsmodelle* Berichte aus dem Zentrum für Meeres- und Klimaforschung, Meteorologie Nr 2. Meteorologisches Institut der Universität Hamburg.

Brutsaert, W., 1982: *Evaporation into the atmosphere: Theory, history, and applications.* D. Reidel Publishing Company, Dordrecht, Holland.

Businger, J. A., J. C. Wyngaard, Y. Izumi, and E. F. Bradley, 1971: Flux-profile relationships in the atmospheric surface layer. *J. Atmos. Sciences* **28**, 181–189.

Cassardo, C., D. Sacchetti, M. G. Morselli, D. Anfossi, G. Brusasca, and A. Longhetto, 1995: A study if the assessment of air temperature, and sensible- and latent-heat fluxes from sonic-anemometer observations. *Il Nuovo Cimento* **18**, 419–440.

Chen, T. H., A. Henderson-Sellers, P. C. D. Milly, A. J. Pitman, A. C. M. Beljaars, J. Polcher, F. Abramopoulos, A. Boone, S. Chang, F. Chen, Y. Dai, C. E. Desborough, R. E. Dickinson, L. Dümenil, M. Ek, J. R. Garratt, N. Gedney, Y. M. Gusev, J. Kim, R. Koster, E. A. Kowalczyk, K. Laval, J. Lean, D. Lettenmaier, X. Liang, J. F. Mahfouf, H. T. Mengelkamp, K. Mitchell, O. N. Nasonova, J. Noilhan, A. Robock, C. Rosenzweig, J. Schaake, C. A. Schlosser, J. P. Schulz, Y. Shao, A. B. Shmakin, D. L. Verseghy, P. Wetzel, E. F. Wood, Y. Xue, Z. L. Yang, and Q. Zeng, 1997: Cabauw experimental results from the project for intercomparison of land-surface parameterization schemes. *J. Climate* **10**, 1194–1215.

Clarke, R. H., 1970: Observational studies in the atmospheric boundary layer. *Q. J. Royal Meteorol. Soc.* **96**, 91–114.

Cullen, M. J. P., 1993: The unified forecast/climate model. *Meteorol. Magazine* **122**, 81–94.

Deland, R. J., 1964: Travelling planetary waves. *Tellus* **16**, 271–273.

Déqué, M., C. Dreveton, A. Braun, and D. Cariolle, 1994: The ARPEGE/IFS Atmospheric Model: A Contribution to the French Community Climate Modelling. *Clim. Dynamics* **10**, 249–266.

Déqué, M. and J. P. Piedelievre, 1995: High resolution climate simulation over Europe. *Clim. Dynamics* **11**, 321–329.

Doblas-Reyes, F. J., M. Déqué, A. Braun, and J. P. Piedelievre, 1998: Impact of resolution on variability in the CNRM runs: Task C1 In *Proceedings of the 3rd HIRETYCS meeting*, Bologna, Italy, pp. 17–19.

Dolman, A. J. and D. Gregory, 1992: The parameterization of rainfall interception in GCMs. *Quart. J. Royal Meteorol. Soc.* **118**, 455–467.

Dümenil, L. and E. Todini, 1992: *A rainfall-runoff scheme for use in the Hamburg climate model* Advances in Theoretical Hydrology, A Tribute to James Dooge, European Geophysical Society Series on Hydrological Sciences, 1. Elservier.

Dyer, A. J., 1974: A review of flux-profile relationships. *Bound. Layer Meteorol.* **7**, 363–372.

Dyer, A. J. and E. F. Bradley, 1982: An alternative analysis of flux-gradient relationships at the 1976 ITCE. *Bound. Layer Meteorol.* **22**, 3–19.

Fahey, B. D., D. L. Murray, and R. M. Jackson, 1996: Detecting fog deposition to tussock by lysimetry at Swampy Summit near Dunedin, New Zealand. *J. Hydrol. (NZ)* **35**, 87–104.

Foken, T. and G. Skeib, 1983: Profile measurements in the atmospheric near-surface layer and the use of suitable universal functions for the determination of the turbulent energy exchange. *Bound. Layer Meteorol.* **25**, 55–62.

Forrer, J., 1999: *The structure and turbulence characteristics of the stable boundary layer over the Greenland Ice Sheet* Geographisches Institut ETH Zürich: Zürcher Klima-Schriften 75.Verlag.

Fürholz, B., 1994: *Die Berechnung der Wasserhaushaltsbilanz an einem voralpinen Einzugsgebiet mit einem Wasserhaushaltsmodell* Diploma Thesis. Institute for Geography ETH Zurich.

Gates, W. L., 1992: AMIP: The Atmospheric Model Intercomparison Project. *Bull. Am. Meteorol. Soc.* **73**, 1962–1970.

Germann, P., H. Lang, and B. Schaedler, 1978: Flaechenmaessige interpretation von Lysimeterdaten mit hilfe von Bodenfeuchtemessungen. *Mitteilgn. Dtsch. Bodenkundl. Gesellsch.* **26**, 61–66.

Gibson, J. K., P. Kållberg, S. Uppala, A. Hernandez, A. Nomura, and E. Serrano, 1997: *ERA description*. ECMWF Reanalysis Project Report Series, 1, Reading.

Gregory, D., R. N. B. Smith, and P. M. Cox, 1996: *Canopy, surface and soil hydrology* Unified Model Documentation Paper 25. Climate Research, Meteorological Office, Bracknell.

Hanafusa, T., T. Fujitani, N. Banno, and H. Uozu, 1979: *On the meteorological tower and its observational system at Tsukuba Science City* Technical Reports of the Meteorological Research Institute No. 3: Meteorological Research Institute, Japan.

Högström, U., 1996: Review of some basic characteristics of the atmospheric surface layer. *Bound. Layer Meteorol.* **78**, 215–246.

Jaeger, L., 1978: Die klimatologische Messstation Hartheim des Meteorologischen Institutes der Universitaet Freiburg. *Br. Ber. Naturf. Ges. Freiburg* **68**, 47–73.

Kaimal, J. C. and J. J. Finnigan, 1994: *Atmospheric boundary layer flows: Their structure and measurement*. Oxford University Press, New York.

Kalnay, E., M. Kanamitsu, R. Kistler, W. Collins, D. Deaven, L. Gandin, M. Iredell, S. Saha, G. White, J. Woollen, Y. Zhu, M. Chelliah, W. Ebisuzaki, W. Higgins, J. Janowiak, K. Mo, C. Ropelewski, J. Wang, A. Leetmaa, R. Reynolds, R. Jenne, and D. Joseph, 1996: The NCEP/NCAR 40-Year Reanalysis Project. *Bull. Am. Meteorol. Soc.* **77**, 437–471.

Larsen, S. E., E. Roeckner, A. Roesch, and S. Zilitinkevich, 2001: *Surface fluxes in climate system*. SFINCS, Final report, EC Contract ENV4-CT97-0573.

Lott, F. and M. J. Miller, 1997: A new sub-grid scale orographic drag parameterization: Its formulation and testing. *Q. J. Royal Meteorol. Soc.* **123**, 101–127.

Louis, J. F., 1979: A parametric model of vertical eddy fluxes in the atmosphere. *Bound. Layer Meteorol.* **17**, 187–202.

Mahrt, L., 1987: Grid-averaged surface fluxes. *Mon. Wea. Review* **115**, 1550–1560.

Mahrt, L. and M. Ek, 1984: The influence of atmospheric stability on potential evaporation. *J. Appl. Climatol. and Appl. Meteorol.* **23**, 222–234.

Martano, P., 2000: Estimation of surface roughness length and displacement height from single-level sonic anemometer data. *J. Appl. Meteorol.* **39**, 708–715.

McMillen, R. T., 1988: An eddy correlation technique with extended applicability to non-simple terrain. *Bound. Layer Meteorol.* **43**, 231–245.

Mintz, Y. and Y. Serafini, 1992: A global monthly climatology of soil moisture and water balance. *Clim. Dynamics* **8**, 13–27.

Molod, A., H. M. Helfand, and L. L. Takacs, 1996: The climatology of parameterized physical processes in the GEOS-1 GCM and their impact on the GEOS-1 Data Assimilation System. *J. Climate* **9**, 764–785.

Monteith, J. L., 1965: Evaporation and environment. *Symp. Soc. Exptl. Biol.* **19**, 205–234.

Monteith, J. L., 1981: Presidential address: Evaporation and surface temperature. *Q. J. Royal Meteorol. Soc.* **107**, 1–24.

Noilhan, J. and S. Planton, 1989: A simple parameterization of land surface processes for meteorological models. *Mon. Wea. Review* **117**, 536–549.

Ohmura, A., H. Gilgen, and M. Wild, 1989: *Global Energy Balance Archive (GEBA), Report 1: Introduction* Geographisches Institut ETH Zürich: Zürcher Geographische Schriften 34.

Ohmura, A., M. Wild, and L. Bengtsson, 1996: A possible change in mass balance of Greenland and Antarctic Ice Sheets in the coming century. *J. Climate* **9**, 2124–2135.

Pan, H. L. and L. Mahrt, 1987: Interaction between soil hydrology and boundary-layer development. *Bound. Layer Meteorol.* **38**, 185–220.

Panofsky, H. A., 1973: Tower micrometeorology In D. A. Hangen (Ed.), *Workshop on Micrometeorology.* American Meteorological Society.

Panofsky, H. A. and J. A. Dutton, 1984: *Atmospheric turbulence.* John Wiley and Sons, New York.

Roeckner, E., K. Arpe, L. Bengtsson, M. Chrisoph, M. Claussen, L. Dümenil, M. Esch, M. Giorgetta, U. Sclese, and U. Schulzweida, 1996: *The atmospheric general circulation model ECHAM-4: Model description and simulation of present-day climate.* Max-Planck-Institut für Meteorologie Report No. 218: Hamburg.

Roesch, A., J. P. Schulz, and M. Wild, 1997: *Comparison and sensitivity studies of the land-surface schemes in the ECHAM general circulation model and the Europa-Modell.* Max-Planck-Institut für Meteorologie Report No. 244, Hamburg.

Schemm, J., S. Schubert, J. Terry, and S. Bloom, 1992: *Estimates of monthly mean soil moisture for 1979-1989* NASA Technical Memorandum 104571. Goddard Space Flight Center, Greenbelt, Maryland.

Schubert, S. D., R. B. Rood, and J. Pfaendtner, 1993: An assimilated dataset for earth science application. *Bull. Am. Meteorol. Soc.* **74**, 2331–2342.

Schulz, J. P., L. Dümenil, and J. Polcher, 1999: *The impact of two different land-surface coupling techniques in a single column version of the ECHAM4 atmospheric model* Max-Planck-Institut für Meteorologie Report No. 297. Hamburg.

Sheppard, R., M. Wild, and A. Ohmura, 2000: The estimation of the latent heat flux over land surfaces in the reanalysis models In *Proceedings of the Second WCRP International Conference on Reanalyses*, WMO/TD-No. 985. Wokefield Park, Reading, UK, 23-27 August 2000, pp. 177–180.

Simmons, A. J., D. M. Burridge, M. Jarraud, C. Girard, and W. Wergen, 1989: The ECMWF medium-range prediction models: Development of the numerical formulations and the impact of increased resolution. *Meteorol. and Atmos. Physics* **40**, 28–60.

Smith, R. N. B., 1996: *Subsurface, surface and boundary layer processes*. Climate Research Group, Meteorological Office, Bracknell.

Stephenson, D. B. and I. M. Held, 1993: GCM response of northern winter stationary waves and storm-tracks to increasing amounts of carbon dioxide. *J. Climate* **6**, 1859–1870.

Stratton, R., 1999: A high resolution AMIP run using the Hadley Centre model HadAM2b. *Clim. Dynamics* **15**, 9–28.

Stull, R. B., 1988: *An introduction to boundary layer meteorology* Kluwer Academic Publishers: Dordrecht The Netherlands.

Thornthwaite, C. W., 1948: An approach toward a rational classification of climate. *Geograph. Review* **38**, 55–94.

Troen, I. B. and L. Mahrt, 1986: A simple model of the atmospheric boundary layer: Sensitivity to surface evaporation. *Bound. Layer Meteorol.* **37**, 129–148.

van Ulden, A. P. and J. Wieringa, 1996: Atmospheric boundary layer research at Cabauw. *Bound. Layer Meteorol.* **78**, 39–69.

Viterbo, P. and A. C. M. Beljaars, 1995: An improved land surface parameterization scheme in the ECMWF model and its validation. *J. Climate* **8**, 2716–2748.

Viterbo, P. and P. Courtier, 1995: The importance of soil water for medium-range weather forecasting. Implications for data assimilation In *Workshop on Imbalance of Slowly Varying Components of Predictable Atmospheric Motions*, Beijing, China, pp. 121–130.

Weller, G. and B. Holmgren, 1974: The microclimates of the Arctic tundra. *J. Appl. Meteorol.* **13**, 854–862.

Wild, M., 2000: Assessment of surface and atmospheric radiation budgets in the ECMWF/NCEP/NASA Reanalyses using collocated surface and satellite data In *Proceeding of the Second WCRP International Conference on Reanalyses*, WMO/TD-No. 985. Wokefield Park, Reading, UK, pp. 23–27.

Wild, M., L. Dümenil, and J. P. Schulz, 1996: Regional climate simulation with a high resolution GCM: Surface hydrology. *Clim. Dynamics* **12**, 755–774.

Wild, M. and A. Ohmura, 1999: The role of clouds and the cloud-free atmosphere in the problem of underestimated absorption of solar radiation in GCM atmospheres. *Phys. Chem. Earth (B)* **24**, 261–268.

Williamson, D. L. and P. J. Rasch, 1994: Water vapour transport in the NCAR CCM2. *Tellus* **46A**, 34–51.

Zeng, Q. and Y. Xie, 1980: Thermodynamical effects on the Qinghai-Xizang Plateau from the radiation balance and heat balance of the earth's surface. *Kexue Tongbao* **25**, 683–688.

Zilitinkevich, S. and P. Calanca, 2000: And extended similarity theory for the stably stratified atmospheric surface layer. *Q. J. Royal Meteorol. Soc.* **126** **(566A)**, 1913–1923.